

UCSF

UC San Francisco Electronic Theses and Dissertations

Title

Associative Learning in Dorsal and Ventral Hippocampus

Permalink

<https://escholarship.org/uc/item/9m0215rq>

Author

Ladow, Max

Publication Date

2022

Peer reviewed|Thesis/dissertation

Associative Learning in Dorsal and Ventral Hippocampus

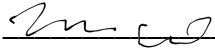
by
Max Ladow

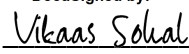
DISSERTATION
Submitted in partial satisfaction of the requirements for degree of
DOCTOR OF PHILOSOPHY

in
Neuroscience

in the
GRADUATE DIVISION
of the
UNIVERSITY OF CALIFORNIA, SAN FRANCISCO

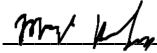
Approved:

DocuSigned by:

3A5C1850C2F1412... Michael Brainard
Chair

DocuSigned by:

DocuSigned by: 4E6... Vikaas Sohal

DocuSigned by:

DocuSigned by: 74C3... Loren Frank

DocuSigned by:

D52190F39543433... Mazen Kheirbek

Committee Members

Copyright 2022

by

Max Ladow

Acknowledgements

I started my neuroscience journey in high school, working with Nilay Yapici in Leslie Vosshall's lab at Rockefeller University. It has been quite a journey since then, through 13.5 years, 7 labs, flies, monkeys, humans, mice, rats, and more mice. Through this long escapade I've been lucky to have many bright and passionate mentors, not only many of the lab heads I've gotten to work with but also my fellow high school, undergrad, technician, graduate students, and postdocs. I'm writing this now because of those many debating lunches, all-night analysis binges, fly-sorting gossip sessions, historical journal clubs, mycologically-focused hikes, really a whole culture of supportive and curious people encouraging me.

Through these experiences, I came to UCSF knowing exactly what I wanted to work on and who I wanted to work with. Through my rotations and the co-mentorship I've received from Mazen Kheirbek and Vikaas Sohal, I've done generally precisely what I had hoped I could do. It has been a pleasure and privilege to receive mentorship from Mazen and Vikaas throughout my PhD. They are expert optimists, yet know how to convince me out of my overly ambitious schemes. Perhaps most importantly, they craft lab communities full of many of my favorite scientists, fostering supportive and collaborative environments.

I am also deeply indebted to Jeremy Biane. Both a collaborator and friend, Jeremy taught me from my rotation how to do surgeries, experiments, analysis, presenting, and how to be a mentor. I am generally in awe of your commitment to not only our research but the achievement of all those who have worked with us, as well as your consistent encouraging approach with me and others through this many year

project. I similarly need to thank Fabio Stefanini, Rachel O'Sullivan, Nick Woods, Victoria Turner, Mark Gergues, and Eszter Kish, as well as the rest of the kheirbek and sohal labs for their continuous support, feedback, casual smatterings of genius, freely given friendship, and deep love for what we do. Also, many thanks to Sunny Choi, Aaditya Garg, Jake Bornstein, Rithvik Ramesh, and my other mentees for sharing your enthusiasm for our work and teaching me how to be a better scientist.

I am thankful to my friends and family--my mom, dad, brother, and grandmother--who have bolstered my efforts at every turn, refining my ideas, celebrating my successes and guiding me through all the tribulations. Phew, we did it.

I am very appreciative of the feedback and support members of my thesis committee—Michael Brainard and Loren Frank--have provided in my training, aiding me to think critically about my research and probe it in new ways. Lastly, thank you to the neuroscience program at UCSF for believing in my potential and allowing me to share this epic experience with y'all, and to Pat and Lucita for making sure the program keeps running.

I feel I have finally achieved the dream explained to me by Michael Crickmoore when I was working with Nilay Yapici and Leslie Vosshall, to help advance just a bit further our understanding the human condition.

Contributions

Chapter 2 of this thesis is reproduced in an adapted form from the following publication:

Jeremy S. Biane, Max A. Ladow, Fabio Stefanini, Sayi P. Boddu, Austin Fan, Shazreh Hassan, Naz Dundar, Daniel L. Apodaca-Montano, Lexi Zichen Zhou, Varya Fayner, Nicholas I. Woods, Mazen A. Kheirbek (2023). Neural dynamics underlying associative learning in the dorsal and ventral hippocampus. In Review.

Conceptualization, J.S.B., M.A.K., M.A.L.; Methodology, J.S.B., M.A.K., M.A.L., N.I.W.; Writing – Original Draft, J.S.B.; Writing – Reviewing & Editing, J.S.B., M.A.K., M.A.L.; Investigation, J.S.B., M.A.L., S.P.B., A.F., S.H., N.D., D.L.A., L.Z.Z., V.F.; Visualization, J.S.B., F.S., M.A.K., M.A.L.; Formal Analysis, J.S.B., F.S., M.A.L., M.A.K.; Supervision, M.A.K., J.S.B.; Funding Acquisition, M.A.K., J.S.B.

Somos nuestra memoria,
somos ese quimérico museo de formas inconstantes,
ese montón de espejos rotos.

We are our memory,
we are that chimerical museum of shifting shapes,
that pile of broken mirrors.

–Jorge Borges, “Cambridge” *Elogio de la sombra*, translated in *In Praise of Darkness*

Associative Learning in Dorsal and Ventral Hippocampus

By Max Ladow

Abstract

Animals associate cues with outcomes and continually update these associations as new information is presented. How might the brain allow for the learning of these associations, particularly the identity and incurred value of the cues? What might the link be between behavioral learning and neural representation? Such a complicated set of questions cannot be addressed by a single set of experiments, but the intent of this thesis is to contribute to the understanding of these foundational questions.

The hippocampus is crucial for associative learning, yet how neurons track changes in cue-outcome associations remains unclear. In the experiments described in this thesis, recordings from dorsal and ventral hippocampus (vCA1 and dCA1) across days of learning in odor and tone associative learning tasks were analyzed to understand how cue and outcome representations might be differently encoded across these areas. Both areas encoded cues and outcomes, but vCA1 representations were dependent on learning and behavioral salience, while dCA1 cue representations exhibited outcome invariant stable representation. Additionally, vCA1 neurons, but not dCA1 neurons, demonstrated encoding of outcome during the odor period as well as temporally broadened encoding of outcome throughout trials. Thus, vCA1 and dCA1 appear to have diverging roles in associative learning encoding.

In Chapter 1 (Introduction), I provide an introduction to the hippocampus, with special emphasis on its dorsal-ventral axis and potential differences in functionality. Over the last few decades, it has been increasingly hinted at that these separate areas or gradient in the hippocampus might serve overlapping but also distinct roles in various memory and learning behaviors. I will illustrate how past approaches, which have tended to focus on the spatial domain and to a lesser extent on emotion, leave many basic questions unanswered.

In Chapter 2 (Neural dynamics underlying associative learning in the dorsal and ventral hippocampus), I present evidence of differences in dorsal and ventral hippocampal representations of associative learning. Using 2-photon calcium imaging, I tracked the same dCA1 and vCA1 neurons across days to determine how responses evolve across phases of odor-outcome learning. I found that, initially, odors elicited robust responses in dCA1, whereas in vCA1 odor responses primarily emerged after learning and embedded information about the paired outcome. Population dynamics in both regions rapidly reorganized with learning, then stabilized into ensembles that stored task representations for days, even after extinction or pairing with a different outcome. Finally, I found stable, robust signals across CA1 when anticipating behaviorally controlled outcomes, but not when anticipating inescapable shock. These results identify how the hippocampus encodes, stores, and updates learned associations, and illuminates the unique contributions of dorsal and ventral hippocampus.

In Chapter 3 (Conclusions), I place these experimental findings within the larger context of our knowledge of the hippocampus to date. I propose that the dorsal ventral axis of the hippocampus has different roles in not only spatial learning or emotion-related behavior but also associative learning and suggest further experimental studies for understanding the mechanisms underlying their differing population dynamics which could be to expand our knowledge of hippocampal function in health and disease states.

Table of Contents

Chapter 1: Introduction.....	1
References for Chapter 1.....	25
Chapter 2: Population dynamics underlying associative learning in the dorsal and ventral hippocampus.....	57
Introduction.....	57
Results.....	59
Discussion.....	71
Methods.....	78
References for Chapter 2.....	112
Chapter 3: Conclusions.....	160
References for Chapter 3.....	167

List of Figures

Chapter 1

Figure 1.1: Schematic of the orientation of the hippocampal long axis in rats, macaque monkeys and humans.....	22
Figure 1.2: The canonical trisynaptic loop.....	23
Figure 1.3: Idealized neuronal firing patterns of hippocampal neurons.....	24

Chapter 2

Figure 2.1: Prior to conditioning, odor stimuli are more strongly represented in dCA1 versus vCA1.....	97
Figure 2.2: Discrimination training enhances task representations.....	99
Figure 2.3: Learned odor representations are sensitive to extinction but can be rapidly reinstated.....	101
Figure 2.4: Learned odor representations are sensitive to extinction but can be rapidly reinstated.....	102
Figure 2.5: Task representations stabilize with learning.....	103
Figure 2.6: Long timescale representations in vCA1.....	105
Figure 2.7: Individual odor representations dominate dCA1, while vCA1 incorporates information about future outcome. Both regions represent anticipated outcome during the trace period.....	106
Figure 2.8: Aversive conditioning and reversal learning.....	108

Figure 2.9: Instrumental control of outcomes increases task-related representations in associative learning.....	110
Supplementary Figure 1.....	127
Supplementary Figure 2.....	129
Supplementary Figure 3.....	131
Supplementary Figure 4.....	133
Supplementary Figure 5.....	135
Supplementary Figure 6.....	137
Supplementary Figure 7.....	138
Supplementary Figure 8.....	140
Supplementary Figure 9.....	141
Supplementary Figure 10.....	142
Supplementary Figure 11.....	144

Chapter 3

Figure 3.1: Summary Schematic.....	166
------------------------------------	-----

List of Tables

Chapter 2

Table 1: Summary of statistics in all figure panels in manuscript.....	146
-------------------------------------------------------------------------------	-----

Chapter 1: Introduction

The seat of memory in the brain

Central to our experience as humans is our ability to remember: to learn, to reflect, to bridge new forms of understanding. Memory functions as a foundation of how we orient our lives and our trajectories through them (Zeidman & Maguire, 2016). When our memory becomes impaired our lives can be altered in myriad ways, not only limiting out future abilities, but also changing ingrained aspects of our identity. For example, in Alzheimer's Disease patients many studies have shown shifts in personality correlated with disease progression, which in sum can lead to a transformation in the sense of self (Addis & Tippett, 2004; Bishop et al., 2010; Chatterjee et al., 1992; Talassi et al., 2007). Thus, to identify the neurobiological mechanisms of and foundations for memory, neuroscience in the past half century has developed basic and clinical insights towards these memory processes and pathologies (Milner et al., 1998).

How should we define memory? A suitable simple and broad definition might be that memory is any process that receives information and crucially maintains or stores it for some eventual use; more specifically, in neuroscience memory is further subclassified into several categories (Eichenbaum, 2017; Eichenbaum et al., 2007). First, the timing of memory storage and retrieval can be used to differentiate memory into short- and long-term, meaning for up to 10-12 seconds or as long as a whole lifetime (Dharani, 2015). Long-term memory can be further classified into declarative and nondeclarative memory, which is to say memory that can be consciously or unconsciously recalled (Camina & Güell, 2017; Cohen & Squire, 1980). And within declarative memory, we can further categorize into semantic and episodic memory,

respectively the memory of factual and first-hand experiential information (Tulving et al., 1972). The episodic memory consists of a combination of context (“where,” place and time) and content (“what,” objects and events) (Dickerson & Eichenbaum, 2010). Returning to short-term memory, that grouping can also be divided into procedural, associative, non-associative, and priming memory (Camina & Güell, 2017). Procedural memory refers to learning actions to complete a task, like riding a bike, while non-associative and priming memory refer to behavior arising to repeated exposure to a stimulus that affects respectively response to that stimulus or other stimuli (Camina & Güell, 2017). Finally, associative memory refers to the creation of an association between sections of information through classical and operant conditioning, which is to say association between a new stimuli and behavior or behavior and consequences of said behavior (Camina & Güell, 2017). While hearing a jingle from an ice cream truck leading you to buy ice cream is an example of classical conditioning, an example of operant conditioning could be learning to eat ice cream slowly after getting brain freeze from consuming more rapidly. This full breakdown of memory subtypes will prove useful in our scientific exploration of memory in specific brain systems that participate in the representation, storage, and recall of conscious and unconscious information.

The undertaking to identify the substrate of memory in the brain has a long historical narrative, but contemporarily began with the study of patients with lesions who exhibited various forms of memory loss. Penfield and Milner in the 1950s examined the memory and other behavior and cognitive abilities of patients, including famously H.M, who had received unilateral or bilateral removal of parts of the frontal or temporal lobe to treat their epilepsy (Milner et al., 1998). Through years of work evaluating the specific

areas disabled or at least modified through surgery and the exact subtypes of memory impacted by the operations, these studies implicated the hippocampus as potentially the fundamental hub in the formation of declarative memory, and then specifically episodic memory rather than semantic memory (Rosenbaum et al., 2000; Squire, 1992).

Early characterizations of hippocampal function: spatial memory

Following these lesion studies, in the following decades researchers directly recording from neurons in the hippocampus of animal models made landmark studies suggesting that the hippocampus might be an essential locus for spatial memory, which could be considered a specific kind of spatial memory (O'Keefe & Nadel, 1978). In 1971, John O'Keefe and John Dostrovsky found that when a rat explored an open platform they observed using extracellular electrophysiological recordings from pyramidal cells in the hippocampus that a subset of these neurons fired especially when a rat was in a particular location of its environment (O'Keefe & Dostrovsky, 1971). These cells became famously referred to as "place cells" because of their consistent activity when an animal (or later a similar property was found in humans) traversed through a specific area (Niediek & Bain, 2014). Later research has shown these cells exist throughout the subregions of the hippocampus, though many differences in the ways these cells represent space have been found across these subregions (Almeida et al., 2012; K. B. Kjelstrup et al., 2008; Leutgeb et al., 2004; Stefanini et al., 2020; Strange et al., 2014). O'Keefe hypothesized that animals create a neural representation of their external world, termed a "cognitive map" (O'Keefe & Nadel, 1978). This theory was earlier developed by Edward Tolman, who observed that animals learned the optimal path through a maze using cues in their environment without exploring every

possible route through the maze (McNaughton et al., 2006; Tolman, 1948). He suggested this ability could only exist if the cues in the environment were somehow represented in the brain into an internally-oriented map. O'Keefe and Dostrovsky's discovery of place cells provided the first neural evidence for this cognitive map theory and specifically implicated the hippocampus as the locus for where such an internal representation might be formed. Importantly, because place cells precisely map the environment externally without respect to only the mouse's location but rather with respect to objective spatial relationships in the environment that suggests that this cognitive map operates through allocentric, or an external, relationship to the environment. This is in contrast to an egocentric, or self-oriented, map to the environment which has been found for other types of mapping, including touch but also there is evidence of egocentric spatially tuned cells in parahippocampal areas (Kunz et al., 2021; Stein, 1989).

This discovery of place cells has ushered in an era of spatial memory exploration in the brain and in the hippocampus in particular; how might this spatial signal in these pyramidal neurons arise? Entorhinal cortex, an adjacent subregion of the allocortex to the hippocampus, provides the main excitatory input to these spatially tuned cells, and May-Britt Moser, Edvard Moser, and colleagues found that a subset of cells in the medial entorhinal cortex (MEC) specifically send the spatial signals necessary for place cell spatial mapping (Hafting et al., 2005). The Mosers labeled this subset of cells in the MEC as "grid cells" due to their firing with "any vertex of a regular grid of equilateral triangles spanning the surface of the environment" and that the clustering of these cells into groups that shared common orientations but with different positions (Hafting et al.,

2005). Additionally, the grid cell spatial map was also found to be allocentric, much like the place cell mapping (Hafting et al., 2005). Further studies demonstrated changes in the grid cell activity directly correlated with changes in the formation and stability of place cells in the hippocampus (Fyhn et al., 2007)

These exciting findings provided further momentum for the study of the hippocampus as a hub of spatial memory. Importantly, other significant discoveries revealed potential mechanisms for how place cells might have stable, long-term representations of spatial maps. Before the examination of place cells, Bliss and Lomo in 1973 found when recording from neurons in a subregion of the rabbit hippocampus that stimulating a subset of these cells led to a long-term, 30 minutes to 10 hours, of potentiated (LTP) response (Bliss & Lomo, 1973). Kandel and colleagues later found that the absence of this LTP mechanism inhibited the formation of stable place cells, suggesting that LTP might allow for long-term spatial memory in the hippocampus (Rotenberg et al., 1996). Additionally, the long-term stability of place cells has been repeatedly demonstrated, with spatial tuning remaining consistent across weeks of time (Wirtshafter & Disterhoft, 2022; Ziv et al., 2013).

Oscillatory organization of spatial information

Another key feature of spatial processing of increasing interest in recent work is the organization of spatial representation through neural oscillations. In 1938, Richard Jung and Alois Kornmüller observed using electroencephalogram (EEG) a large-amplitude, sinusoidal wave pattern in the rabbit hippocampus between 4 and 7 Hz (though contemporary definitions for theta would broaden this range to 4-12 Hz), which they named “theta” activity (Andersen et al., 2007). Initially, theta activity was thought to

be related to attention and movement behaviors, could be related to different learning states, and was regulated through neuromodulatory signals (Grastyan et al., 1959; Green & Arduini, 1954; Holmes & Adey, 1960; Vanderwolf, 1969). Later work has shown theta synchronizes across the hippocampus and place cells fire at shifting phases of the theta cycle throughout the hippocampal population; thus theta processing synchronizes hippocampal spatial coding and primes LTP for sequential structure (Jensen & Lisman, 2000; Lisman, 2005; Mitchell & Ranck, 1980; O'Keefe & Recce, 1993; Skaggs et al., 1996). Furthermore, there is some evidence that hippocampal activity occurring at the positive phase of theta is potentiating while activity during the negative phase is de-potentiating, including an elegant study by Siegle and Wilson (Hölscher et al., 1997; Huerta & Lisman, 1995; Hyman et al., 2003; Pavlides et al., 1988; Siegle & Wilson, 2014). Finally, it has been suggested that place cell activity during theta phase precession predicts future behavior by rapidly sweeping through potential paths before an animal moves through them (Johnson & Redish, 2007; Pfeiffer & Foster, 2013).

In addition to theta rhythms, other activity states including 100 ms duration “sharp wave” activity and associated higher frequency ~100 ms “ripple” oscillations (SWR) in the high gamma 100 to 200 Hz range have been identified in the hippocampus during both awake and sleep states (Karlsson & Frank, 2009; O'Keefe & Nadel, 1978; Vanderwolf, 1969; Wilson & McNaughton, 1994). Recordings at different points along the hippocampus have shown that sharp waves are in phase over the entire extent and might originate in the CA3 subregion of the hippocampus (Chrobak & Buzsáki, 1996; Csicsvari et al., 2000). During SWR there are synchronous bursts in most hippocampal

interneurons and subsets of place cells, specifically cells that contain previous or potential future spatial trajectories, including both reactivation of remote experiences and immediate future navigational behavior that may not be tied to experience from the current environment (Buzsáki et al., 1992; Diba & Buzsáki, 2007; Foster & Wilson, 2006; Gupta et al., 2010; Karlsson & Frank, 2009; Pfeiffer & Foster, 2013). This suggests SWRs and “replay” may play a role in memory consolidation (Jadhav & Frank, 2009). Elimination or interruption of SWRs can impair behavior in memory tasks (Girardeau et al., 2009; Jadhav et al., 2012). SWRs appear to engage cortical and subcortical areas through hippocampal outputs, thus providing a mechanism for memory retrieval across the brain (Girardeau et al., 2017; Gomperts et al., 2015; Jadhav et al., 2016; Ji & Wilson, 2007; Pennartz et al., 2004; Rothschild et al., 2017; Sosa et al., 2020). A holistic hypothesis posits SWRs and replay might engage in both consolidation and retrieval through local hippocampal and target cortical activation (Carr et al., 2011; Joo & Frank, 2018). While SWR and replay offer a compelling organizational mechanism for hippocampal memory processes, other gamma-theta oscillations extraneous to SWRs also appear to temporally organize spatial information between different hippocampal inputs (Colgin et al., 2009; Johnson & Redish, 2007).

While the enthusiasm for exploring the role of the hippocampus as specifically a spatial map has led to transformative advances in molecular, cellular, systems, and computational neuroscience, it has also led to a relative lack of experiments examining how the area might support non-spatial memory (Aronov et al., 2017). This summary of research focused on spatial mapping in the hippocampus provides context for the perhaps constrained understanding that developed of all hippocampal functioning

(Wood et al., 1999). There are many benefits of studying the hippocampal coding for non-spatial memory (the research for which is discussed below) including that looking at such coding might reveal other roles for individual or populations of neurons in non-spatial memory processes. The dominance of spatial research in experiments across these subregions indicates this is particularly likely considering that each subregion of the hippocampus is thought to have its own defined role (Knierim & Neunuebel, 2016). Interestingly, recent studies suggest that specifically the non-spatial hippocampal and associated circuits might change in the earlier stages of neurodegenerative disease, including Alzheimer's disease, and that their differences compared to spatial circuits might provide insight into vulnerability under these disease states (Khan et al., 2014; Knierim & Neunuebel, 2016).

Hippocampal anatomy and signaling through subregions

The hippocampus is a bilateral structure in the mammalian forebrain (O'Keefe & Nadel, 1978). In the rat, it's a curved sausage-like formation, lying behind the septum and is further categorized into subregions through its various axes. Its name however, comes from the typical shape seen through cross section in humans that has the appearance of a "seahorse" which is the latin meaning of hippocampus (Figure 1.1). In the rat and mouse, where most hippocampal studies have been conducted, the top portion is referred to as the dorsal region, while the bottom portion is referred to as the ventral region and lies in the temporal part of the brain. Throughout the dorsal-ventral axis the hippocampus consists of a three-layered structure made up of plexiform, principal cell, and diffuse fiber layers (Figure 1.1). This is in contrast to the typical six-layered structure in the neocortex (Chauhan et al., 2021). The hippocampus follows this

layering through the dentate gyrus, the hippocampus proper (also known as the cornu ammonia, abbreviated CA), and the subiculum. In 1934, Lorente de No further subdivided the CA into CA1, CA2, CA3, and CA4, which is still used today to categorize the subareas containing principal glutamatergic cells (Andersen et al., 2007).

While the hippocampus has a variety of circuits fundamental to its operation, the primary classical circuit is known as the trisynaptic loop and goes through the dentate gyrus, CA3, and CA1 (Figure 1.2). This circuit begins with the sensory information from the entorhinal cortex being sent to the hippocampus via the perforant path, which has direct and indirect subcomponents (Hjorth-Simonsen & Jeune, 1972; Witter et al., 2017). In the direct pathway, layer III cells of the entorhinal cortex project onto the apical dendrites of CA1 pyramidal cells, which are the main output neurons of the hippocampus and project back to deeper layers of entorhinal cortex (Figure 1.2)(van Groen, 2001). CA1 cells project to many other areas beyond the entorhinal cortex, including importantly the previously mentioned subiculum which also projects to the entorhinal cortex and many other regions (Naber et al., 2001). The direct pathway in particular has received a lot of attention due the ease of accessing it near CA1; this research has helped explain how spatial memory in the subset of cells in CA1 that form place cells might be differentiated based on divergent projections (Brun et al., 2008; Igarashi et al., 2014; Masurkar et al., 2017).

The indirect pathway is made up of projections from layer II of the entorhinal cortex, and these axons synapse onto granule cells and interneurons in the dentate gyrus (Figure 1.2)(Andersen et al., 1966; Lomo, 1971). This synapse is the first stage of the trisynaptic loop. Granule cells exhibit sparse activity patterns, with high levels of

network inhibition such that granule cell activity is thought to result in the inhibition of nearby granule cells (Hashimoto et al., 2017; Luna et al., 2019). This feature of granule cells in the dentate gyrus allows for the separation of similar inputs into non-overlapping population activity (Aimone et al., 2011). A crucial feature of memory encoding is the ability to distinguish between similar stimuli, contexts, and complete episodic memories. The dentate gyrus through this sparse encoding ability has been hypothesized to pattern separate by which salient and non-salient information can be effectively distinguished (Kesner, 2013; Rolls, 2013b). Medial and lateral entorhinal cortex (LEC) project to exclusive and respectively to the middle and outer molecular layers of granule cell dendrites, thus sending spatial and contextual information through distinct pathways (Treves & Rolls, 1992; Witter, 2007; Woods et al., 2018; Yasuda & Mayford, 2006). Granule cells dramatically outnumber the entorhinal cells they receive projections from, allowing for an ease of non-overlapping representation of entorhinal input (Amaral & Witter, 1989; McNaughton & Morris, 1987; Scharfman & Myers, 2012; Treves & Rolls, 1994). Also these cells fascinatingly have the unusual feature of continuing to develop through adulthood, a process known as neurogenesis, leading to classification of granule cells into mature and immature categories depending on their age (Gage et al., 1995; Ming & Song, 2011; Overstreet-Wadiche & Westbrook, 2006). These immature or adult-born granule cells have been shown to possess an outsized role relative to their population size specifically in pattern separation—disrupting neurogenesis affects discrimination between highly similar but not very different contexts—and are also thought to inhibit mature granule cell activity (Danielson et al., 2016; Drew et al., 2016; Kheirbek, Tannenholz, et al., 2012; Sahay et al., 2011).

Granule cells also receive excitation and inhibition from both ipsi- and contralateral glutamatergic mossy cells and gabaergic inhibitory cells in the hilus (Figure 1.2)(Freund & Buzsáki, 1996; Scharfman, 2016). Recent work has demonstrated mossy cells also have spatial tuning properties, though they are less specifically tuned compared to the surrounding granule cells and interestingly show broader firing across contexts (Danielson et al., 2017; GoodSmith et al., 2017; Senzai & Buzsáki, 2017). Additionally, in circuit with the interneurons in the dentate that mossy cells also synapse onto, it has been found that the mossy cells primary effect on granule cells is to provide feedforward inhibition, likely through HIPP cells, a group of interneurons that express somatostatin and neuropeptide Y (Galloni et al., 2022; Jinde et al., 2013; Scharfman & Myers, 2012). This feedforward inhibition appears to enhance granule cell sparse encoding; removal of mossy cell activity impairs pattern separation ability (Jinde et al., 2013). Organization of this inhibition might be achieved through mossy cell activity during theta oscillations, leading to the phase-locking synchronization of target granule cells and interneurons (Soltesz et al., 1993) Mossy cells also appear to influence neurogenesis in the dentate gyrus through a complicated mix of excitation and inhibition as well as the excretion of sonic hedgehog, a multifunctional signaling protein governing pattern formation, proliferation and cell survival during embryogenesis (Antonelli et al., 2019; Yeh et al., 2018). Additionally they may have a unique role in priming adult born granule cell activity and connectivity (Chancey et al., 2014).

Returning to the trisynaptic loop, granule cells send axons through the hilus which form the mossy fiber pathway (Figure 1.2). These axons terminate onto CA3 pyramidal cells via large mossy terminals, often contacting 11-15 CA3 cells and 7-12

mossy cells with a single granule cell, leading to the reliable activation of CA3 and mossy cells (Acsády et al., 1998; Henze et al., 2002). CA3 pyramidal cells also are the most highly recurrent excitatory connections among principal cells in the hippocampus, which has been suggested to allow for an “auto-associative” network in which a few cells can readily excite the populations of cells that might encode for different features of the environment, including space, time, context, and others (Le Duigou et al., 2014; Rolls, 2013a; van Strien et al., 2009). Through this recurrent excitation it is hypothesized that CA3 pattern completes, meaning the representation of individual and separate pieces of information can lead to the rapid reactivation or initial association of ensembles coding for the previously described features (Kondo et al., 2009; Leutgeb & Leutgeb, 2007; McHugh et al., 2007).

CA3 axons, in a formation known as the Schaffer collaterals, synapse onto proximal dendrites of CA1 pyramidal cells in the third and final synapse in the trisynaptic circuit (Figure 1.2) (van Strien et al., 2009). While the dentate gyrus and CA3 have been both theorized and results suggest they pattern separate and pattern complete the precise role for CA1 aside from being the output node for the hippocampus has been less certain. Some proposed functions include novelty detection, enrichment of CA3 encodings, or redistributing information during recall (Hasselmo et al., 2000; Kaifosh & Losonczy, 2016; McClelland & Goddard, 1996; Treves & Rolls, 1994). Further recent work shows CA1 representations have a higher correlation with behavioral discrimination compared to granule cell representations, suggesting that CA1 weighs decorrelated information from the dentate gyrus, through CA3, and produces a map of memory representations that can be used to guide behavior (Allegra et al., 2020)

As previously mentioned, the trisynaptic circuit spans along the dorsal-ventral axis of the hippocampus, however almost all of the previously described functionality of this circuit has been determined through experiments focused on the dorsal portion of the hippocampus. In rodents, the dorsal hippocampus lies directly under the cortex and the principal neurons are aligned with the skull which provides an ease of surgical and recording access. In contrast, experiments targeting the ventral hippocampus, particularly in vivo experiments, are far more difficult to acquire (Jung et al., 1994). Nonetheless, a variety of experiments have attempted to dissect potential differences across this axis to ascertain if the areas have a functional subdivision which has been an open question in the field since Ramón Y Cajal (1901) and Lorente de Nó (1934) both observed differences in dorsal-ventral anatomy as they established the trisynaptic circuit and other basic features of hippocampal anatomy (Fanselow & Dong, 2010).

Further experimental anatomy work has established that different transverse levels along the dorsoventral axis establish axonal connections in a highly differentiated manner (Cenquizca & Swanson, 2007). Separate projections from entorhinal cortex have been shown to specifically synapse onto separate dorsal and ventral areas within the dentate gyrus, resulting in information from infralimbic and prelimbic cortices routing to ventral hippocampus, and cingulate cortex and other areas being routed to dorsal hippocampus. Not only does this show that the dorsal and ventral hippocampus receive separate inputs, but also because these projecting areas have differing functions, namely that spatial and contextual versus emotional functionality, this suggests dorsal and ventral hippocampus may also preferentially process different types of information (Komorowski et al., 2013; Strange et al., 2014). Interestingly the map of these

projections is continuous rather than discretized, suggesting a potential gradient of dorsal-ventral function rather than discrete subareas (Amaral & Witter, 1989). Projections from other areas and cell types have also been shown to predominantly target only dorsal or ventral hippocampus, including a long-range inhibitory projection from medial prefrontal cortex (Malik et al., 2022; Rajasethupathy et al., 2015). There also are differences in neuromodulatory input: cholinergic afferents from the fornix more strongly innervate dorsal hippocampus, whereas serotonergic and dopaminergic afferents provide their strongest innervation to ventral hippocampus (Gage et al., 1983; Pitkänen et al., 2000; Verney et al., 1985; Witter et al., 1989). Similarly, the projections from the dorsal and ventral hippocampus differ, including their projections to the lateral septum (Risold & Swanson, 1996). Also, ventral hippocampus but not dorsal hippocampus projects directly to medial prefrontal cortex (mPFC) (Burwell & Witter, 2002; Hoover & Vertes, 2007; Verwer et al., 1997). Recently, cutting-edge techniques have been applied to mapping hippocampal inputs and outputs, the results of which have show that there are separate populations of neurons in ventral hippocampus that project to both multiple and individual targets in a non-random fashion (Arszovszki et al., 2014; Gergues et al., 2020). In contrast to these anatomical studies, genomic experiments have found sharp divides between potential dorsal and ventral subregions (Fanselow & Dong, 2010; Thompson et al., 2008). Thus, while it remains unclear exactly how the border between these subareas might be delineated, perhaps there are both gradual and sharp divisions in differing functionalities along the dorsal-ventral axis, understanding the functional differences of these two poles of the hippocampus may

provide a useful perspective for better understanding how different types of memory processing are enabled via anatomical segregation (Komorski et al., 2020).

Differential coding along the hippocampal dorsal-ventral axis

If spatial coding exists throughout the dorsal hippocampus, does ventral hippocampus also code for spatial location and do these subareas diverge in their spatial coding qualities? Early lesion studies suggest that lesions of the dorsal hippocampus had greater effects on spatial memory, while lesions of the ventral hippocampus had greater effects on emotional memory, particularly shown in fear conditioning experiments (K. G. Kjelstrup et al., 2002; Komorowski et al., 2013; Moser et al., 1993; Pothuizen et al., 2004; Rogers et al., 2006; Rogers & Kesner, 2006). However, there could be variability in these studies to the extent of how much of the dorsal or ventral hippocampus might be affected, so their overall effectiveness is difficult to determine.

Initial electrophysiological recording experiments in ventral hippocampus suggest that place cells also exist but contain less finely tuned spatial information and have lower stability compared to dorsal hippocampus (Jung et al., 1994; Poucet et al., 1994). A study by Royer and colleagues suggests not only a progressive diminishment of spatial encoding, but also found the ventral CA3 differentially encoded positively and negatively valenced spatial locations or contexts, specifically rewarded or avoided areas, in a biased manner compared to dorsal CA3. In addition to less spatial tuning in ventral CA3, they found less theta power and fewer theta-locked spatially tuned pyramidal cells and interneurons, similar to the change in spatial tuning and theta through the corresponding projections in the dorsal-ventral gradient in entorhinal cortex

(Hafting et al., 2005; Royer et al., 2010). SWRs from dorsal or ventral hippocampus are asynchronously activated and activate distinct and opposing patterns of nucleus accumbens activity (Sosa et al., 2020). Other experiments recording from dorsal and intermediate CA1 have also shown enhanced and rapid remapping of place cells in intermediate CA1 to reward locations by specific reward location cells rather than increased place cell density (Jarzebowski et al., 2022; Jin & Lee, 2021). Finally, dorsal and ventral CA1 (dCA1 and vCA1) and dentate gyrus neurons appear to have a variety of differences in synaptic transmission and plasticity, including differences in LTP induction, leading to divergent input-output functionality (Koutsoumpa & Papatheodoropoulos, 2019; Malik & Johnston, 2017; Trompoukis & Papatheodoropoulos, 2020). Cumulatively, this demonstrates a substantial set of differences in spatial encoding and other basic properties between dCA1 and vCA1.

If vCA1 spatial coding is less richly tuned than dCA1, might it have some other specialized functionality? Lesion and pharmacological studies first suggested ventral hippocampus but not dorsal hippocampus might be involved in anxiety, trace fear, and unconditioned fear behavior, including avoidance behavior in the elevated plus maze and similar innate anxiety tasks (Bannerman et al., 2004; Deacon et al., 2002; File et al., 1996; Gray & McNaughton, 2003; Maren & Holt, 2004; Trent & Menard, 2010; Trivedi, 2004). Studies manipulating and recording from ventral hippocampus neurons in vCA1 and the dentate gyrus and inputs have confirmed this, demonstrating that exciting/inhibiting these cells drives/suppresses innate anxiety behavior, preferentially represent anxiogenic features, and selectively route anxiety-related information to specific downstream targets (Ciocchi et al., 2015; Jimenez et al., 2018, 2020; Kheirbek

et al., 2013; Parfitt et al., 2017; Yeates et al., 2020). Similarly, many experiments have shown manipulating ventral neurogenesis affects emotional behaviors and contextual memory: manipulating neurogenesis through behavior, x-irradiation, genetically and through modifying cellular plasticity can lead to neurogenesis suppression which increases anxiety behavior, and/or stimulating neurogenesis which dampens anxiety behavior (Hill et al., 2015; Kheirbek, Klemenhagen, et al., 2012; Kheirbek, Tannenholz, et al., 2012; Kheirbek & Hen, 2011; Oliveira et al., 2020; Sahay et al., 2011; Santarelli et al., 2003; Schloesser et al., 2009; Surget et al., 2011; Tannenholz et al., 2014; Tronel et al., 2012). Additionally, neurogenesis is necessary for the anxiolytic effects of certain antidepressants, and antidepressant treatment reverses behaviorally depleted stressed mouse neurogenesis (Tanti et al., 2012). Collectively, these studies demonstrate the differential role of ventral and not dorsal hippocampus in anxiety-related and other behaviors.

Beyond internal hippocampal signaling, the circuitry between the ventral hippocampus and other areas have also been found to be crucial for anxiety and other emotion-related behaviors. Again, ventral hippocampus has many outputs and a large body of literature has established that many of these connections control various anxiety, fear, and other memory processes and behaviors, but of particular interest are the vCA1-NAc, vCA1-mPFC, vCA1-amygdala pathways (Gergues et al., 2020; Jacinto et al., 2016). In studies recording from both ventral hippocampus and mPFC, mPFC neuron and local field potential anxiety-related activity was influenced by phase-locking to ventral hippocampal theta (Adhikari et al., 2010, 2011). Activation and inhibition of this vCA1-mPFC pathway can bidirectionally modulate anxiety behavior and vasoactive

intestinal polypeptide (VIP) interneurons and serotonin 1B receptors appear to control this information flow during avoidance behavior (Kjaerby et al., 2016; Lee et al., 2019; Padilla-Coreano et al., 2016, 2019). Similarly, optogenetic inhibition of the basal lateral amygdala (BLA)-vCA1 projection is anxiolytic, and BLA and vCA1 and BLA-mPFC theta synchrony are increased during innate forms of anxiety (Felix-Ortiz et al., 2013, 2016; Lesting et al., 2011; Likhtik et al., 2014; Stujenske et al., 2014). Broader circuits tying all of these areas together have been identified as related to fear and reward learning, and, in one case, predictive of the emergence of major depressive disorder-related behavior in mice subject to chronic social defeat (Beyeler et al., 2018; Burgos-Robles et al., 2017; Hultman et al., 2018).

While vCA1-NAc projections also appear to carry a certain form of anxiety-related information, for example, vCA1-NAc activity regulates susceptibility to chronic social defeat stress in mice, vCA1-NAc circuitry also has been heavily implicated in reward-seeking and social behavior (Bagot et al., 2015; Bryant & Barker, 2020; Okuyama et al., 2016; Sosa et al., 2020). Specifically ventral hippocampus but not dorsal hippocampus inactivation impairs reward-seeking behavior and memory retrieval (Riaz et al., 2017). Ventral hippocampus projections to NAc are crucial for driving NAc activity which is gated by prefrontal input, are more likely to be active near rewards, are necessary for acquisition of contextual reward conditioning, and inactivation of this projection restores reward-seeking habitual behavior (Barker et al., 2019; Britt et al., 2012; Charara & Grace, 2003; Ciochi et al., 2015; Ito et al., 2008; LeGates et al., 2018). Interestingly, NAc neurons activated during hippocampal SWRs were only tuned to task- and reward-related information during dorsal but not ventral SWRs, and ventral

SWRs were insensitive to reward learning in an appetitive spatial task (Sosa et al., 2020). The studies on vCA1-NAc/mPFC/BLA circuits suggest the ventral hippocampus plays a variety of important roles in approach- and avoidance-based behaviors in a variety of multi-area networks.

Associative learning in the hippocampus

How might we further differentiate dorsal and ventral hippocampus not only through information type (spatial vs. emotion-related information), but also through processing through memory and learning? From Marr's early modeling of the hippocampal autoassociation to initial studies of conditioned and unconditioned learning in rabbits and other animals, it has long been theorized that the hippocampus is involved in memory and learning tasks that have an inherent temporal discontinuity that needs to be bridged so that associations between disparate pieces of information can be formed (Eichenbaum et al., 1987; McEchron & Disterhoft, 1997; Segal et al., 1972; Wallenstein et al., 1998; Willshaw et al., 2015). Studies lesioning the hippocampus or fornix, even specifically ventral hippocampus, found impaired associative memory, thus further supporting this hypothesis, and also suggesting that hippocampal encoding of associative memory need not be reliant on a spatial feature in the associated information (Brasted et al., 2003; Macedo et al., 2012). Eichenbaum and colleagues recording in dCA1 during a odor-reward associative learning task in rats found individual neuron responses were at least as correlated with odor cue sensing and reward approach as they were to other spatial information (Eichenbaum et al., 1987, 1999). These results indicate specific cell types in the hippocampus might play complementary roles: cue-encoding cells might compare relative cue valence, reward-encoding cells

might enable goal-seeking behavior across successive trials, and theta-locked interneurons might synchronize these representations. Other groups have elaborated upon hippocampal involvement in odor processing--especially in the context of odor-object associations and sequence learning (Ahmed et al., 2020; Igarashi et al., 2014; Li et al., 2017; MacDonald et al., 2013; Taxidis et al., 2020). Interestingly, Taxidis and colleagues found not only high stable odor responsive cells, but also time-cells that exhibited sparse and dynamic fields that remapped in both cases, including into new population sequences. However, this body of work has exclusively examined associative learning in dorsal CA1 pyramidal cells.

Taken together, the existence of a dorsal-ventral functional axis in the hippocampus and its potential role in non-spatial associative learning is well-evidenced, and it could be studied with a similar type of scrutiny as the spatial cognitive map in dorsal hippocampal networks. Thus, the purpose of this thesis is to further contribute to the understanding of how dCA1 and vCA1 represent non-spatial associative learning, in our case primarily in response to odors.

Relevance to human hippocampal functioning

This introduction has focused on hippocampal function primarily in animal models, particularly rodents, but many of the findings have been replicated in humans and the animal model literature has often extended observations and hypotheses originally derived from human experiments. While there are a variety of basic differences in human and rodent hippocampal anatomy, the basic structure of the hippocampus, its dorsal-ventral axis (posterior-anterior in humans), and these regions

various general functions appear to be preserved (Figure 1.1)(Castelhana et al., 2022; Poppenk et al., 2013; Strange et al., 2014). Additionally, many studies have found with regard to the dorsal-ventral split of spatial and emotion information processing, place cells and place-related theta activity, episodic and associative memory functioning, general similarities to the rodent literature (Bach et al., 2019; Castelhana et al., 2022; Ekstrom et al., 2003; Goyal et al., 2020; Ito & Lee, 2016; Khemka et al., 2017; Kirkby et al., 2018; Miller et al., 2013; Wixted et al., 2018). Better understanding of associative learning in the hippocampus will hopefully enable improved treatment for a range of conditions. For example, it has been suggested that post-traumatic stress disorder (PTSD) impairs and may also be exacerbated by hippocampal-related associative learning for multiple types of information. Further understanding mechanisms in different PTSD subtypes will enable tailored interventions, particularly for treatment-resistant PTSD (Lambert & McLaughlin, 2019).

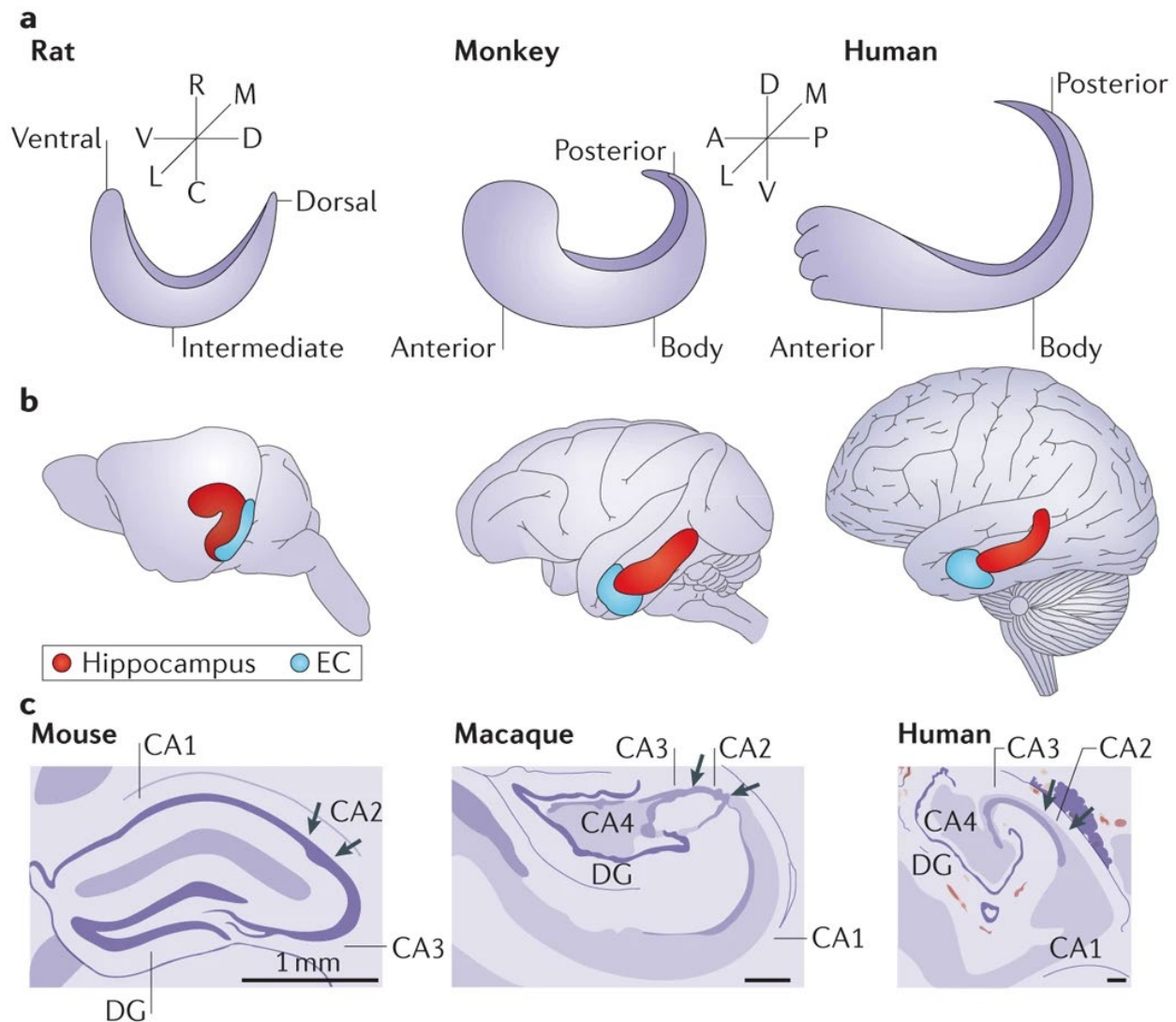


Figure 1.1: (a) Schematic of the orientation of the hippocampal long axis in rats, macaque monkeys and humans. The longitudinal axis is described as ventrodorsal in rodents and as anteroposterior in primates. The precise anatomical definition for a dorsal versus ventral portions of the hippocampus are undetermined, although in general, topologically, the former is positioned close to the retrosplenial cortex and the latter close to the amygdaloid complex. (b) The full long axis of the hippocampus (red) can be seen in brains of rats, macaque monkeys and humans, with the entorhinal cortex (EC) shown in blue. (c) Drawings of Nissl cross-sections of mouse, rhesus and human hippocampi. A, anterior; C, caudal; D, dorsal; DG, dentate gyrus; L, lateral; M, medial; P, posterior; R, rostral; V, ventral. Adapted from (Strange et al., 2014)

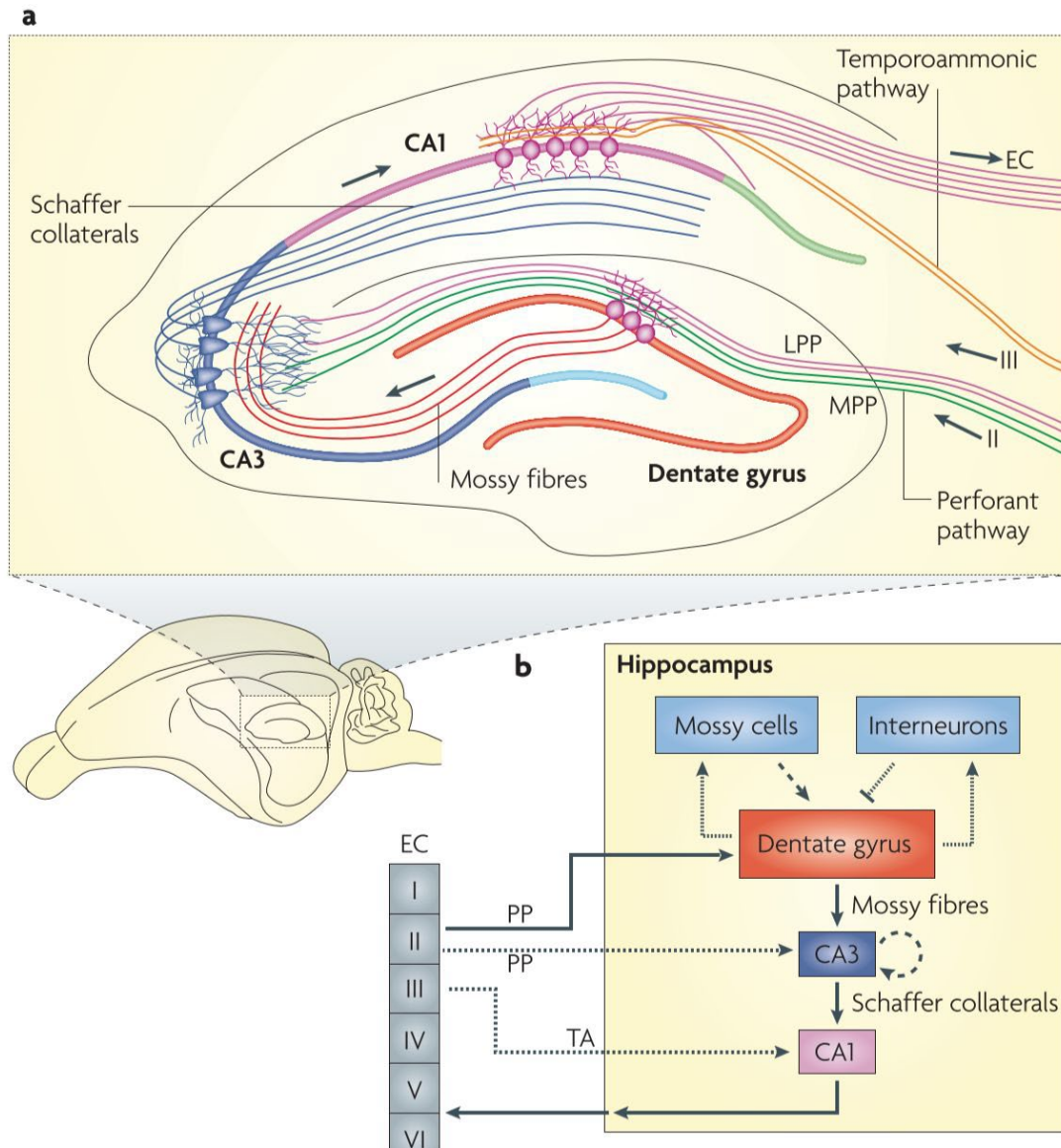
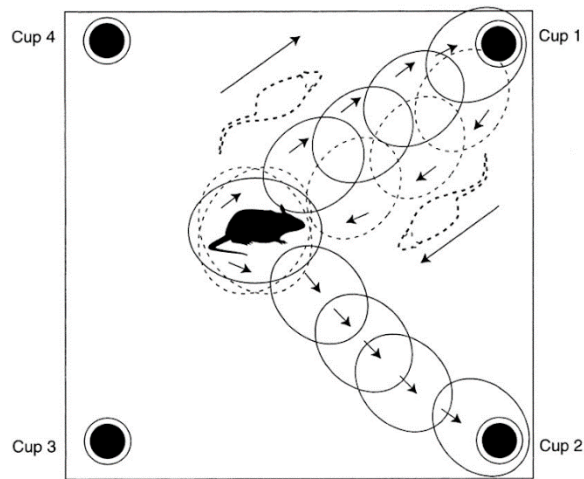


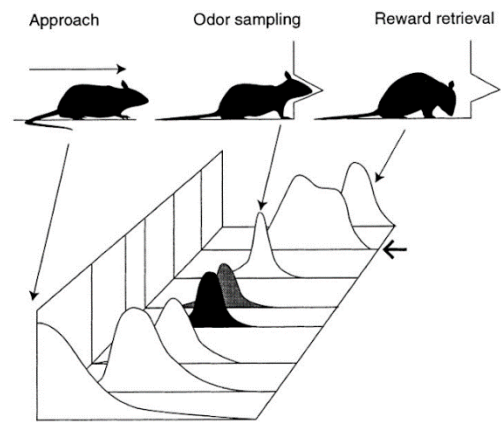
Figure 1.2: (a) The canonical trisynaptic loop is shown (solid arrows show EC-DG-CA3-CA1-EC unidirectional flow of information along principal cell layers of hippocampus), with layer II entorhinal fibers innervating the dentate gyrus and layer III axons synapsing onto CA1 pyramidal cells. Layer II fibers from the MEC target the middle third of granule cell dendrites, and LEC fibers synapse on the outer third of granule cell dendrites in the molecular layer of the dentate gyrus. Granule cell axons form the mossy fiber pathway and synapse onto CA3 pyramidal cells. CA3 pyramidal cell axons comprise the schaffer collateral pathway and synapse onto CA1 pyramidal cells. Finally, CA1 pyramidal cells send projections that exit the hippocampus and target deep layers of entorhinal cortex. (b), the schematic organization of the trisynaptic loop is shown. Granule cell activity in the dentate gyrus is modulated by the excitation/inhibition balance established through the activity of mossy cells and inhibitory interneurons, which provide feedforward and feedback inhibition onto granule cells. Figure adapted from (Deng et al., 2010).

Spatial Working Memory



A

Odor Guided Memory



B

Figure 1.3: Idealized neuronal firing patterns of an ensemble of hippocampal neurons. (a) Schematic firing patterns of place cells from a rat performing a spatial working memory task in an open arena. Arrows indicate place cell directionality. (b) Schematic nonspatial firing patterns of cells from a rat performing an olfactory discrimination task. Each panel illustrates the increased firing of a cell at a particular time during trial performance. The two curves with different closed patterns indicate cells that fire only during the presentation of a particular odor configuration. The arrow at the right of one curve indicates a cell that encodes the sequence of odor sampling and the behavioral response. Figure adapted from (Eichenbaum et al., 1987, 1999).

References for Chapter 1

- Acsády, L., Kamondi, A., Sík, A., Freund, T., & Buzsáki, G. (1998). GABAergic cells are the major postsynaptic targets of mossy fibers in the rat hippocampus. *The Journal of Neuroscience: The Official Journal of the Society for Neuroscience*, *18*(9), 3386–3403.
- Addis, D. R., & Tippett, L. J. (2004). Memory of myself: autobiographical memory and identity in Alzheimer's disease. *Memory*, *12*(1), 56–74.
- Adhikari, A., Topiwala, M. A., & Gordon, J. A. (2010). Synchronized activity between the ventral hippocampus and the medial prefrontal cortex during anxiety. *Neuron*, *65*(2), 257–269.
- Adhikari, A., Topiwala, M. A., & Gordon, J. A. (2011). Single units in the medial prefrontal cortex with anxiety-related firing patterns are preferentially influenced by ventral hippocampal activity. *Neuron*, *71*(5), 898–910.
- Ahmed, M. S., Priestley, J. B., Castro, A., Stefanini, F., Solis Canales, A. S., Balough, E. M., Lavoie, E., Mazzucato, L., Fusi, S., & Losonczy, A. (2020). Hippocampal Network Reorganization Underlies the Formation of a Temporal Association Memory. *Neuron*, *107*(2), 283–291.e6.
- Aimone, J. B., Deng, W., & Gage, F. H. (2011). Resolving new memories: a critical look at the dentate gyrus, adult neurogenesis, and pattern separation. *Neuron*, *70*(4), 589–596.
- Allegra, M., Posani, L., Gómez-Ocádiz, R., & Schmidt-Hieber, C. (2020). Differential Relation between Neuronal and Behavioral Discrimination during Hippocampal Memory Encoding. *Neuron*, *108*(6), 1103–1112.e6.

- Almeida, L. de, de Almeida, L., Idiart, M., & Lisman, J. E. (2012). The single place fields of CA3 cells: A two-stage transformation from grid cells. In *Hippocampus* (Vol. 22, Issue 2, pp. 200–208). <https://doi.org/10.1002/hipo.20882>
- Amaral, D. G., & Witter, M. P. (1989). The three-dimensional organization of the hippocampal formation: a review of anatomical data. *Neuroscience*, *31*(3), 571–591.
- Andersen, P., Department of Physiology Institute of Basic Medical Sciences Per Andersen, Morris, R., Amaral, D., Department of Psychiatry David Amaral, O'Keefe, J., Bliss, T., Professor Department of Anatomy and Developmental Biology Institute of Cognitive Neuroscience John O'Keefe, & Division of Neurophysiology Tim Bliss. (2007). *The Hippocampus Book*. Oxford University Press.
- Andersen, P., Holmqvist, B., & Voorhoeve, P. E. (1966). Entorhinal Activation of Dentate Granule Cells. In *Acta Physiologica Scandinavica* (Vol. 66, Issue 4, pp. 448–460). <https://doi.org/10.1111/j.1748-1716.1966.tb03223.x>
- Antonelli, F., Casciati, A., & Pazzaglia, S. (2019). Sonic hedgehog signaling controls dentate gyrus patterning and adult neurogenesis in the hippocampus. *Neural Regeneration Research*, *14*(1), 59–61.
- Aronov, D., Nevers, R., & Tank, D. W. (2017). Mapping of a non-spatial dimension by the hippocampal-entorhinal circuit. *Nature*, *543*(7647), 719–722.
- Arszovszki, A., Borhegyi, Z., & Klausberger, T. (2014). Three axonal projection routes of individual pyramidal cells in the ventral CA1 hippocampus. *Frontiers in Neuroanatomy*, *8*, 53.

- Bach, D. R., Hoffmann, M., Finke, C., Hurlemann, R., & Ploner, C. J. (2019). Disentangling Hippocampal and Amygdala Contribution to Human Anxiety-Like Behavior. *The Journal of Neuroscience: The Official Journal of the Society for Neuroscience*, 39(43), 8517–8526.
- Bagot, R. C., Parise, E. M., Peña, C. J., Zhang, H.-X., Maze, I., Chaudhury, D., Persaud, B., Cachope, R., Bolaños-Guzmán, C. A., Cheer, J. F., Deisseroth, K., Han, M.-H., & Nestler, E. J. (2015). Ventral hippocampal afferents to the nucleus accumbens regulate susceptibility to depression. In *Nature Communications* (Vol. 6, Issue 1). <https://doi.org/10.1038/ncomms8062>
- Bannerman, D. M., Rawlins, J. N. P., McHugh, S. B., Deacon, R. M. J., Yee, B. K., Bast, T., Zhang, W.-N., Pothuizen, H. H. J., & Feldon, J. (2004). Regional dissociations within the hippocampus--memory and anxiety. *Neuroscience and Biobehavioral Reviews*, 28(3), 273–283.
- Barker, J. M., Bryant, K. G., & Chandler, L. J. (2019). Inactivation of ventral hippocampus projections promotes sensitivity to changes in contingency. *Learning & Memory*, 26(1), 1–8.
- Beyeler, A., Chang, C.-J., Silvestre, M., Lévêque, C., Namburi, P., Wildes, C. P., & Tye, K. M. (2018). Organization of Valence-Encoding and Projection-Defined Neurons in the Basolateral Amygdala. *Cell Reports*, 22(4), 905–918.
- Bishop, N. A., Lu, T., & Yankner, B. A. (2010). Neural mechanisms of ageing and cognitive decline. *Nature*, 464(7288), 529–535.

- Bliss, T. V., & Lomo, T. (1973). Long-lasting potentiation of synaptic transmission in the dentate area of the anaesthetized rabbit following stimulation of the perforant path. *The Journal of Physiology*, *232*(2), 331–356.
- Brasted, P. J., Bussey, T. J., Murray, E. A., & Wise, S. P. (2003). Role of the hippocampal system in associative learning beyond the spatial domain. *Brain: A Journal of Neurology*, *126*(Pt 5), 1202–1223.
- Britt, J. P., Benaliouad, F., McDevitt, R. A., Stuber, G. D., Wise, R. A., & Bonci, A. (2012). Synaptic and Behavioral Profile of Multiple Glutamatergic Inputs to the Nucleus Accumbens. In *Neuron* (Vol. 76, Issue 4, pp. 790–803).
<https://doi.org/10.1016/j.neuron.2012.09.040>
- Brun, V. H., Leutgeb, S., Wu, H.-Q., Schwarcz, R., Witter, M. P., Moser, E. I., & Moser, M.-B. (2008). Impaired spatial representation in CA1 after lesion of direct input from entorhinal cortex. *Neuron*, *57*(2), 290–302.
- Bryant, K. G., & Barker, J. M. (2020). Arbitration of Approach-Avoidance Conflict by Ventral Hippocampus. *Frontiers in Neuroscience*, *14*, 615337.
- Burgos-Robles, A., Kimchi, E. Y., Izadmehr, E. M., Porzenheim, M. J., Ramos-Guasp, W. A., Nieh, E. H., Felix-Ortiz, A. C., Namburi, P., Leppla, C. A., Presbrey, K. N., Anandalingam, K. K., Pagan-Rivera, P. A., Anahtar, M., Beyeler, A., & Tye, K. M. (2017). Amygdala inputs to prefrontal cortex guide behavior amid conflicting cues of reward and punishment. *Nature Neuroscience*, *20*(6), 824–835.
- Burwell, R. D., & Witter, M. P. (2002). Basic anatomy of the parahippocampal region in monkeys and rats. In *The Parahippocampal Region Organization and Role in*

Cognitive Function (pp. 34–59).

<https://doi.org/10.1093/acprof:oso/9780198509172.003.0003>

Buzsaki, G., Horvath, Z., Urioste, R., Hetke, J., & Wise, K. (1992). High-frequency network oscillation in the hippocampus. In *Science* (Vol. 256, Issue 5059, pp. 1025–1027). <https://doi.org/10.1126/science.1589772>

Camina, E., & Güell, F. (2017). The Neuroanatomical, Neurophysiological and Psychological Basis of Memory: Current Models and Their Origins. *Frontiers in Pharmacology*, 8, 438.

Carr, M. F., Jadhav, S. P., & Frank, L. M. (2011). Hippocampal replay in the awake state: a potential substrate for memory consolidation and retrieval. In *Nature Neuroscience* (Vol. 14, Issue 2, pp. 147–153). <https://doi.org/10.1038/nn.2732>

Castelhano, J., Duarte, I., Bernardino, I., Pelle, F., Francione, S., Sales, F., & Castelo-Branco, M. (2022). Intracranial recordings in humans reveal specific hippocampal spectral and dorsal vs. ventral connectivity signatures during visual, attention and memory tasks. *Scientific Reports*, 12(1), 3488.

Cenquizca, L. A., & Swanson, L. W. (2007). Spatial organization of direct hippocampal field CA1 axonal projections to the rest of the cerebral cortex. In *Brain Research Reviews* (Vol. 56, Issue 1, pp. 1–26). <https://doi.org/10.1016/j.brainresrev.2007.05.002>

Chancey, J. H., Poulsen, D. J., Wadiche, J. I., & Overstreet-Wadiche, L. (2014). Hilar mossy cells provide the first glutamatergic synapses to adult-born dentate granule cells. *The Journal of Neuroscience: The Official Journal of the Society for Neuroscience*, 34(6), 2349–2354.

- Charara, A., & Grace, A. A. (2003). Dopamine receptor subtypes selectively modulate excitatory afferents from the hippocampus and amygdala to rat nucleus accumbens neurons. *Neuropsychopharmacology: Official Publication of the American College of Neuropsychopharmacology*, 28(8), 1412–1421.
- Chatterjee, A., Strauss, M. E., Smyth, K. A., & Whitehouse, P. J. (1992). Personality changes in Alzheimer's disease. *Archives of Neurology*, 49(5), 486–491.
- Chauhan, P., Jethwa, K., Rathawa, A., Chauhan, G., & Mehra, S. (2021). The Anatomy of the Hippocampus. In R. Pluta (Ed.), *Cerebral Ischemia*. Exon Publications.
- Chrobak, J. J., & Buzsáki, G. (1996). High-frequency oscillations in the output networks of the hippocampal-entorhinal axis of the freely behaving rat. *The Journal of Neuroscience: The Official Journal of the Society for Neuroscience*, 16(9), 3056–3066.
- Ciocchi, S., Passecker, J., Malagon-Vina, H., Mikus, N., & Klausberger, T. (2015). Brain computation. Selective information routing by ventral hippocampal CA1 projection neurons. *Science*, 348(6234), 560–563.
- Cohen, N. J., & Squire, L. R. (1980). Preserved learning and retention of pattern-analyzing skill in amnesia: dissociation of knowing how and knowing that. *Science*, 210(4466), 207–210.
- Colgin, L. L., Denninger, T., Fyhn, M., Hafting, T., Bonnevie, T., Jensen, O., Moser, M.-B., & Moser, E. I. (2009). Frequency of gamma oscillations routes flow of information in the hippocampus. *Nature*, 462(7271), 353–357.

- Csicsvari, J., Hirase, H., Mamiya, A., & Buzsáki, G. (2000). Ensemble patterns of hippocampal CA3-CA1 neurons during sharp wave-associated population events. *Neuron*, *28*(2), 585–594.
- Danielson, N. B., Kaifosh, P., Zaremba, J. D., Lovett-Barron, M., Tsai, J., Denny, C. A., Balough, E. M., Goldberg, A. R., Drew, L. J., Hen, R., Losonczy, A., & Kheirbek, M. A. (2016). Distinct Contribution of Adult-Born Hippocampal Granule Cells to Context Encoding. *Neuron*, *90*(1), 101–112.
- Danielson, N. B., Turi, G. F., Ladow, M., Chavlis, S., Petrantonakis, P. C., Poirazi, P., & Losonczy, A. (2017). In Vivo Imaging of Dentate Gyrus Mossy Cells in Behaving Mice. *Neuron*, *93*(3), 552–559.e4.
- Deacon, R. M. J., Bannerman, D. M., & Rawlins, J. N. P. (2002). Anxiolytic effects of cytotoxic hippocampal lesions in rats. *Behavioral Neuroscience*, *116*(3), 494–497.
- Deng, W., Aimone, J. B., & Gage, F. H. (2010). New neurons and new memories: how does adult hippocampal neurogenesis affect learning and memory? *Nature Reviews. Neuroscience*, *11*(5), 339–350.
- Dharani, K. (2015). Memory. In *The Biology of Thought* (pp. 53–74).
<https://doi.org/10.1016/b978-0-12-800900-0.00003-8>
- Diba, K., & Buzsáki, G. (2007). Forward and reverse hippocampal place-cell sequences during ripples. In *Nature Neuroscience* (Vol. 10, Issue 10, pp. 1241–1242).
<https://doi.org/10.1038/nn1961>
- Dickerson, B. C., & Eichenbaum, H. (2010). The episodic memory system: neurocircuitry and disorders. *Neuropsychopharmacology: Official Publication of the American College of Neuropsychopharmacology*, *35*(1), 86–104.

- Drew, L. J., Kheirbek, M. A., Luna, V. M., Denny, C. A., Clodt, M. A., Wu, M. V., Jain, S., Scharfman, H. E., & Hen, R. (2016). Activation of local inhibitory circuits in the dentate gyrus by adult-born neurons. *Hippocampus*, *26*(6), 763–778.
- Eichenbaum, H. (2017). On the Integration of Space, Time, and Memory. *Neuron*, *95*(5), 1007–1018.
- Eichenbaum, H., Dudchenko, P., Wood, E., Shapiro, M., & Tanila, H. (1999). The hippocampus, memory, and place cells: is it spatial memory or a memory space? *Neuron*, *23*(2), 209–226.
- Eichenbaum, H., Kuperstein, M., Fagan, A., & Nagode, J. (1987). Cue-sampling and goal-approach correlates of hippocampal unit activity in rats performing an odor-discrimination task. *The Journal of Neuroscience: The Official Journal of the Society for Neuroscience*, *7*(3), 716–732.
- Eichenbaum, H., Yonelinas, A. P., & Ranganath, C. (2007). The medial temporal lobe and recognition memory. *Annual Review of Neuroscience*, *30*, 123–152.
- Ekstrom, A. D., Kahana, M. J., Caplan, J. B., Fields, T. A., Isham, E. A., Newman, E. L., & Fried, I. (2003). Cellular networks underlying human spatial navigation. *Nature*, *425*(6954), 184–188.
- Fanselow, M. S., & Dong, H.-W. (2010). Are the dorsal and ventral hippocampus functionally distinct structures? *Neuron*, *65*(1), 7–19.
- Felix-Ortiz, A. C., Beyeler, A., Seo, C., Leppla, C. A., Wildes, C. P., & Tye, K. M. (2013). BLA to vHPC inputs modulate anxiety-related behaviors. *Neuron*, *79*(4), 658–664.

- Felix-Ortiz, A. C., Burgos-Robles, A., Bhagat, N. D., Leppla, C. A., & Tye, K. M. (2016). Bidirectional modulation of anxiety-related and social behaviors by amygdala projections to the medial prefrontal cortex. *Neuroscience*, *321*, 197–209.
- File, S. E., Gonzalez, L. E., & Andrews, N. (1996). Comparative study of pre- and postsynaptic 5-HT_{1A} receptor modulation of anxiety in two ethological animal tests. *The Journal of Neuroscience: The Official Journal of the Society for Neuroscience*, *16*(15), 4810–4815.
- Foster, D. J., & Wilson, M. A. (2006). Reverse replay of behavioural sequences in hippocampal place cells during the awake state. *Nature*, *440*(7084), 680–683.
- Freund, T. F., & Buzsáki, G. (1996). Interneurons of the hippocampus. *Hippocampus*, *6*(4), 347–470.
- Fyhn, M., Hafting, T., Treves, A., Moser, M.-B., & Moser, E. I. (2007). Hippocampal remapping and grid realignment in entorhinal cortex. *Nature*, *446*(7132), 190–194.
- Gage, F. H., Björklund, A., & Stenevi, U. (1983). Reinnervation of the partially deafferented hippocampus by compensatory collateral sprouting from spared cholinergic and noradrenergic afferents. *Brain Research*, *268*(1), 27–37.
- Gage, F. H., Coates, P. W., Palmer, T. D., Kuhn, H. G., Fisher, L. J., Suhonen, J. O., Peterson, D. A., Suhr, S. T., & Ray, J. (1995). Survival and differentiation of adult neuronal progenitor cells transplanted to the adult brain. *Proceedings of the National Academy of Sciences of the United States of America*, *92*(25), 11879–11883.
- Galloni, A. R., Samadzelkava, A., Hiremath, K., Oumnov, R., & Milstein, A. D. (2022). Recurrent Excitatory Feedback From Mossy Cells Enhances Sparsity and Pattern

- Separation in the Dentate Gyrus Indirect Feedback Inhibition. *Frontiers in Computational Neuroscience*, 16, 826278.
- Gergues, M. M., Han, K. J., Choi, H. S., Brown, B., Clausing, K. J., Turner, V. S., Vainchtein, I. D., Molofsky, A. V., & Kheirbek, M. A. (2020). Circuit and molecular architecture of a ventral hippocampal network. *Nature Neuroscience*, 23(11), 1444–1452.
- Girardeau, G., Benchenane, K., Wiener, S. I., Buzsáki, G., & Zugaro, M. B. (2009). Selective suppression of hippocampal ripples impairs spatial memory. In *Nature Neuroscience* (Vol. 12, Issue 10, pp. 1222–1223). <https://doi.org/10.1038/nn.2384>
- Girardeau, G., Inema, I., & Buzsáki, G. (2017). Reactivations of emotional memory in the hippocampus-amygdala system during sleep. *Nature Neuroscience*, 20(11), 1634–1642.
- Gomperts, S. N., Kloosterman, F., & Wilson, M. A. (2015). VTA neurons coordinate with the hippocampal reactivation of spatial experience. *eLife*, 4. <https://doi.org/10.7554/eLife.05360>
- GoodSmith, D., Chen, X., Wang, C., Kim, S. H., Song, H., Burgalossi, A., Christian, K. M., & Knierim, J. J. (2017). Spatial Representations of Granule Cells and Mossy Cells of the Dentate Gyrus. *Neuron*, 93(3), 677–690.e5.
- Goyal, A., Miller, J., Qasim, S. E., Watrous, A. J., Zhang, H., Stein, J. M., Inman, C. S., Gross, R. E., Willie, J. T., Lega, B., Lin, J.-J., Sharan, A., Wu, C., Sperling, M. R., Sheth, S. A., McKhann, G. M., Smith, E. H., Schevon, C., & Jacobs, J. (2020). Functionally distinct high and low theta oscillations in the human hippocampus. *Nature Communications*, 11(1), 2469.

- Grastyan, E., Lissak, K., Madarasz, I., & Donhoffer, H. (1959). Hippocampal electrical activity during the development of conditioned reflexes. *Electroencephalography and Clinical Neurophysiology*, 11(3), 409–430.
- Gray, J. A., & McNaughton, N. (2003). *The Neuropsychology of Anxiety: An Enquiry Into the Function of the Septo-hippocampal System*. Oxford University Press.
- Green, J. D., & Arduini, A. A. (1954). HIPPOCAMPAL ELECTRICAL ACTIVITY IN AROUSAL. In *Journal of Neurophysiology* (Vol. 17, Issue 6, pp. 533–557).
<https://doi.org/10.1152/jn.1954.17.6.533>
- Gupta, A. S., van der Meer, M. A. A., Touretzky, D. S., & Redish, A. D. (2010). Hippocampal replay is not a simple function of experience. *Neuron*, 65(5), 695–705.
- Hafting, T., Fyhn, M., Molden, S., Moser, M.-B., & Moser, E. I. (2005). Microstructure of a spatial map in the entorhinal cortex. *Nature*, 436(7052), 801–806.
- Hashimoto-dani, Y., Nasrallah, K., Jensen, K. R., Chávez, A. E., Carrera, D., & Castillo, P. E. (2017). LTP at Hilar Mossy Cell-Dentate Granule Cell Synapses Modulates Dentate Gyrus Output by Increasing Excitation/Inhibition Balance. *Neuron*, 95(4), 928–943.e3.
- Hasselmo, M. E., Fransen, E., Dickson, C., & Alonso, A. A. (2000). Computational modeling of entorhinal cortex. *Annals of the New York Academy of Sciences*, 911, 418–446.
- Henze, D. A., Wittner, L., & Buzsáki, G. (2002). Single granule cells reliably discharge targets in the hippocampal CA3 network in vivo. *Nature Neuroscience*, 5(8), 790–795.

- Hill, A. S., Sahay, A., & Hen, R. (2015). Increasing Adult Hippocampal Neurogenesis is Sufficient to Reduce Anxiety and Depression-Like Behaviors. In *Neuropsychopharmacology* (Vol. 40, Issue 10, pp. 2368–2378). <https://doi.org/10.1038/npp.2015.85>
- Hjorth-Simonsen, A., & Jeune, B. (1972). Origin and termination of the hippocampal perforant path in the rat studied by silver impregnation. *The Journal of Comparative Neurology*, 144(2), 215–232.
- Holmes, J. E., & Adey, W. R. (1960). Electrical activity of the entorhinal cortex during conditioned behavior. In *American Journal of Physiology-Legacy Content* (Vol. 199, Issue 5, pp. 741–744). <https://doi.org/10.1152/ajplegacy.1960.199.5.741>
- Hölscher, C., Anwyl, R., & Rowan, M. J. (1997). Stimulation on the positive phase of hippocampal theta rhythm induces long-term potentiation that can be depotentiated by stimulation on the negative phase in area CA1 in vivo. *The Journal of Neuroscience: The Official Journal of the Society for Neuroscience*, 17(16), 6470–6477.
- Hoover, W. B., & Vertes, R. P. (2007). Anatomical analysis of afferent projections to the medial prefrontal cortex in the rat. In *Brain Structure and Function* (Vol. 212, Issue 2, pp. 149–179). <https://doi.org/10.1007/s00429-007-0150-4>
- Huerta, P. T., & Lisman, J. E. (1995). Bidirectional synaptic plasticity induced by a single burst during cholinergic theta oscillation in CA1 in vitro. *Neuron*, 15(5), 1053–1063.
- Hultman, R., Ulrich, K., Sachs, B. D., Blount, C., Carlson, D. E., Ndubuizu, N., Bagot, R. C., Parise, E. M., Vu, M.-A. T., Gallagher, N. M., Wang, J., Silva, A. J., Deisseroth, K., Mague, S. D., Caron, M. G., Nestler, E. J., Carin, L., & Dzirasa, K. (2018). Brain-

wide Electrical Spatiotemporal Dynamics Encode Depression Vulnerability. *Cell*, 173(1), 166–180.e14.

Hyman, J. M., Wyble, B. P., Goyal, V., Rossi, C. A., & Hasselmo, M. E. (2003). Stimulation in hippocampal region CA1 in behaving rats yields long-term potentiation when delivered to the peak of theta and long-term depression when delivered to the trough. *The Journal of Neuroscience: The Official Journal of the Society for Neuroscience*, 23(37), 11725–11731.

Igarashi, K. M., Ito, H. T., Moser, E. I., & Moser, M.-B. (2014). Functional diversity along the transverse axis of hippocampal area CA1. *FEBS Letters*, 588(15), 2470–2476.

Ito, R., & Lee, A. C. H. (2016). The role of the hippocampus in approach-avoidance conflict decision-making: Evidence from rodent and human studies. *Behavioural Brain Research*, 313, 345–357.

Ito, R., Robbins, T. W., Pennartz, C. M., & Everitt, B. J. (2008). Functional interaction between the hippocampus and nucleus accumbens shell is necessary for the acquisition of appetitive spatial context conditioning. *The Journal of Neuroscience: The Official Journal of the Society for Neuroscience*, 28(27), 6950–6959.

Jacinto, L. R., Cerqueira, J. J., & Sousa, N. (2016). Patterns of Theta Activity in Limbic Anxiety Circuit Preceding Exploratory Behavior in Approach-Avoidance Conflict. In *Frontiers in Behavioral Neuroscience* (Vol. 10).

<https://doi.org/10.3389/fnbeh.2016.00171>

Jadhav, S. P., & Frank, L. M. (2009). Reactivating Memories for Consolidation. In *Neuron* (Vol. 62, Issue 6, pp. 745–746).

<https://doi.org/10.1016/j.neuron.2009.06.002>

- Jadhav, S. P., Kemere, C., German, P. W., & Frank, L. M. (2012). Awake hippocampal sharp-wave ripples support spatial memory. *Science*, 336(6087), 1454–1458.
- Jadhav, S. P., Rothschild, G., Roumis, D. K., & Frank, L. M. (2016). Coordinated Excitation and Inhibition of Prefrontal Ensembles during Awake Hippocampal Sharp-Wave Ripple Events. *Neuron*, 90(1), 113–127.
- Jarzebowski, P., Hay, Y. A., Grewe, B. F., & Paulsen, O. (2022). Different encoding of reward location in dorsal and intermediate hippocampus. *Current Biology: CB*, 32(4), 834–841.e5.
- Jensen, O., & Lisman, J. E. (2000). Position reconstruction from an ensemble of hippocampal place cells: contribution of theta phase coding. *Journal of Neurophysiology*, 83(5), 2602–2609.
- Ji, D., & Wilson, M. A. (2007). Coordinated memory replay in the visual cortex and hippocampus during sleep. In *Nature Neuroscience* (Vol. 10, Issue 1, pp. 100–107). <https://doi.org/10.1038/nn1825>
- Jimenez, J. C., Berry, J. E., Lim, S. C., Ong, S. K., Kheirbek, M. A., & Hen, R. (2020). Contextual fear memory retrieval by correlated ensembles of ventral CA1 neurons. *Nature Communications*, 11(1), 3492.
- Jimenez, J. C., Su, K., Goldberg, A. R., Luna, V. M., Biane, J. S., Ordek, G., Zhou, P., Ong, S. K., Wright, M. A., Zweifel, L., Paninski, L., Hen, R., & Kheirbek, M. A. (2018). Anxiety Cells in a Hippocampal-Hypothalamic Circuit. *Neuron*, 97(3), 670–683.e6.
- Jinde, S., Zsiros, V., & Nakazawa, K. (2013). Hilar mossy cell circuitry controlling dentate granule cell excitability. *Frontiers in Neural Circuits*, 7, 14.

- Jin, S.-W., & Lee, I. (2021). Differential encoding of place value between the dorsal and intermediate hippocampus. *Current Biology: CB*, 31(14), 3053–3072.e5.
- Johnson, A., & Redish, A. D. (2007). Neural ensembles in CA3 transiently encode paths forward of the animal at a decision point. *The Journal of Neuroscience: The Official Journal of the Society for Neuroscience*, 27(45), 12176–12189.
- Joo, H. R., & Frank, L. M. (2018). The hippocampal sharp wave-ripple in memory retrieval for immediate use and consolidation. *Nature Reviews. Neuroscience*, 19(12), 744–757.
- Jung, M. W., Wiener, S. I., & McNaughton, B. L. (1994). Comparison of spatial firing characteristics of units in dorsal and ventral hippocampus of the rat. *The Journal of Neuroscience: The Official Journal of the Society for Neuroscience*, 14(12), 7347–7356.
- Kaifosh, P., & Losonczy, A. (2016). Mnemonic Functions for Nonlinear Dendritic Integration in Hippocampal Pyramidal Circuits. *Neuron*, 90(3), 622–634.
- Karlsson, M. P., & Frank, L. M. (2009). Awake replay of remote experiences in the hippocampus. *Nature Neuroscience*, 12(7), 913–918.
- Kesner, R. P. (2013). An analysis of the dentate gyrus function. In *Behavioural Brain Research* (Vol. 254, pp. 1–7). <https://doi.org/10.1016/j.bbr.2013.01.012>
- Khan, U. A., Liu, L., Provenzano, F. A., Berman, D. E., Profaci, C. P., Sloan, R., Mayeux, R., Duff, K. E., & Small, S. A. (2014). Molecular drivers and cortical spread of lateral entorhinal cortex dysfunction in preclinical Alzheimer's disease. *Nature Neuroscience*, 17(2), 304–311.

- Kheirbek, M. A., Drew, L. J., Burghardt, N. S., Costantini, D. O., Tannenholz, L., Ahmari, S. E., Zeng, H., Fenton, A. A., & Hen, R. (2013). Differential control of learning and anxiety along the dorsoventral axis of the dentate gyrus. *Neuron*, *77*(5), 955–968.
- Kheirbek, M. A., & Hen, R. (2011). Dorsal vs Ventral Hippocampal Neurogenesis: Implications for Cognition and Mood. In *Neuropsychopharmacology* (Vol. 36, Issue 1, pp. 373–374). <https://doi.org/10.1038/npp.2010.148>
- Kheirbek, M. A., Klemenhagen, K. C., Sahay, A., & Hen, R. (2012). Neurogenesis and generalization: a new approach to stratify and treat anxiety disorders. *Nature Neuroscience*, *15*(12), 1613–1620.
- Kheirbek, M. A., Tannenholz, L., & Hen, R. (2012). NR2B-dependent plasticity of adult-born granule cells is necessary for context discrimination. *The Journal of Neuroscience: The Official Journal of the Society for Neuroscience*, *32*(25), 8696–8702.
- Khemka, S., Barnes, G., Dolan, R. J., & Bach, D. R. (2017). Dissecting the Function of Hippocampal Oscillations in a Human Anxiety Model. *The Journal of Neuroscience: The Official Journal of the Society for Neuroscience*, *37*(29), 6869–6876.
- Kirkby, L. A., Luongo, F. J., Lee, M. B., Nahum, M., Van Vleet, T. M., Rao, V. R., Dawes, H. E., Chang, E. F., & Sohal, V. S. (2018). An Amygdala-Hippocampus Subnetwork that Encodes Variation in Human Mood. In *Cell* (Vol. 175, Issue 6, pp. 1688–1700.e14). <https://doi.org/10.1016/j.cell.2018.10.005>
- Kjaerby, C., Athilingam, J., Robinson, S. E., Iafrati, J., & Sohal, V. S. (2016). Serotonin 1B Receptors Regulate Prefrontal Function by Gating Callosal and Hippocampal Inputs. *Cell Reports*, *17*(11), 2882–2890.

- Kjelstrup, K. B., Solstad, T., Brun, V. H., Hafting, T., Leutgeb, S., Witter, M. P., Moser, E. I., & Moser, M.-B. (2008). Finite scale of spatial representation in the hippocampus. *Science*, 321(5885), 140–143.
- Kjelstrup, K. G., Tuvnes, F. A., Steffenach, H.-A., Murison, R., Moser, E. I., & Moser, M.-B. (2002). Reduced fear expression after lesions of the ventral hippocampus. In *Proceedings of the National Academy of Sciences* (Vol. 99, Issue 16, pp. 10825–10830). <https://doi.org/10.1073/pnas.152112399>
- Knierim, J. J., & Neunuebel, J. P. (2016). Tracking the flow of hippocampal computation: Pattern separation, pattern completion, and attractor dynamics. *Neurobiology of Learning and Memory*, 129, 38–49.
- Komorowski, R. W., Garcia, C. G., Wilson, A., Hattori, S., Howard, M. W., & Eichenbaum, H. (2013). Ventral hippocampal neurons are shaped by experience to represent behaviorally relevant contexts. *The Journal of Neuroscience: The Official Journal of the Society for Neuroscience*, 33(18), 8079–8087.
- Komorski, S., Leszczyński, M. K., Justyniak, I., & Lewiński, J. (2020). Structural diversity of ethylzinc derivatives of 3,5-substituted pyrazoles. *Dalton Transactions*, 49(47), 17388–17394.
- Kondo, H., Lavenex, P., & Amaral, D. G. (2009). Intrinsic connections of the macaque monkey hippocampal formation: II. CA3 connections. *The Journal of Comparative Neurology*, 515(3), 349–377.
- Koutsoumpa, A., & Papatheodoropoulos, C. (2019). Short-term dynamics of input and output of CA1 network greatly differ between the dorsal and ventral rat hippocampus. *BMC Neuroscience*, 20(1), 35.

- Kunz, L., Brandt, A., Reinacher, P. C., Staresina, B. P., Reifensstein, E. T., Weidemann, C. T., Herweg, N. A., Patel, A., Tsitsiklis, M., Kempster, R., Kahana, M. J., Schulze-Bonhage, A., & Jacobs, J. (2021). A neural code for egocentric spatial maps in the human medial temporal lobe. *Neuron*, *109*(17), 2781–2796.e10.
- Lambert, H. K., & McLaughlin, K. A. (2019). Impaired hippocampus-dependent associative learning as a mechanism underlying PTSD: A meta-analysis. *Neuroscience and Biobehavioral Reviews*, *107*, 729–749.
- Le Duigou, C., Simonnet, J., Teleńczuk, M. T., Fricker, D., & Miles, R. (2014). Recurrent synapses and circuits in the CA3 region of the hippocampus: an associative network. *Frontiers in Cellular Neuroscience*, *7*, 262.
- Lee, A. T., Cunniff, M. M., See, J. Z., Wilke, S. A., Luongo, F. J., Ellwood, I. T., Ponnayolu, S., & Sohal, V. S. (2019). VIP Interneurons Contribute to Avoidance Behavior by Regulating Information Flow across Hippocampal-Prefrontal Networks. *Neuron*, *102*(6), 1223–1234.e4.
- LeGates, T. A., Kvarta, M. D., Tooley, J. R., Francis, T. C., Lobo, M. K., Creed, M. C., & Thompson, S. M. (2018). Reward behaviour is regulated by the strength of hippocampus-nucleus accumbens synapses. *Nature*, *564*(7735), 258–262.
- Lesting, J., Narayanan, R. T., Kluge, C., Sangha, S., Seidenbecher, T., & Pape, H.-C. (2011). Patterns of coupled theta activity in amygdala-hippocampal-prefrontal cortical circuits during fear extinction. *PloS One*, *6*(6), e21714.
- Leutgeb, S., & Leutgeb, J. K. (2007). Pattern separation, pattern completion, and new neuronal codes within a continuous CA3 map. *Learning & Memory*, *14*(11), 745–757.

- Leutgeb, S., Leutgeb, J. K., Treves, A., Moser, M.-B., & Moser, E. I. (2004). Distinct ensemble codes in hippocampal areas CA3 and CA1. *Science*, *305*(5688), 1295–1298.
- Likhtik, E., Stujenske, J. M., Topiwala, M. A., Harris, A. Z., & Gordon, J. A. (2014). Prefrontal entrainment of amygdala activity signals safety in learned fear and innate anxiety. *Nature Neuroscience*, *17*(1), 106–113.
- Lisman, J. (2005). The theta/gamma discrete phase code occurring during the hippocampal phase precession may be a more general brain coding scheme. *Hippocampus*, *15*(7), 913–922.
- Li, Y., Xu, J., Liu, Y., Zhu, J., Liu, N., Zeng, W., Huang, N., Rasch, M. J., Jiang, H., Gu, X., Li, X., Luo, M., Li, C., Teng, J., Chen, J., Zeng, S., Lin, L., & Zhang, X. (2017). A distinct entorhinal cortex to hippocampal CA1 direct circuit for olfactory associative learning. *Nature Neuroscience*, *20*(4), 559–570.
- Luna, V. M., Anacker, C., Burghardt, N. S., Khandaker, H., Andreu, V., Millette, A., Leary, P., Ravenelle, R., Jimenez, J. C., Mastrodonato, A., Denny, C. A., Fenton, A. A., Scharfman, H. E., & Hen, R. (2019). Adult-born hippocampal neurons bidirectionally modulate entorhinal inputs into the dentate gyrus. *Science*, *364*(6440), 578–583.
- Lomo, T. (1971). Patterns of activation in a monosynaptic cortical pathway: The perforant path input to the dentate area of the hippocampal formation. In *Experimental Brain Research* (Vol. 12, Issue 1). <https://doi.org/10.1007/bf00234414>
- MacDonald, C. J., Carrow, S., Place, R., & Eichenbaum, H. (2013). Distinct hippocampal time cell sequences represent odor memories in immobilized rats. *The*

Journal of Neuroscience: The Official Journal of the Society for Neuroscience,
33(36), 14607–14616.

Macedo, C. E., Angst, M.-J., Gobaille, S., Schleef, C., Guignard, B., Guiberteau, T.,
Louilot, A., & Sandner, G. (2012). Prefrontal dopamine release and sensory-specific
satiety altered in rats with neonatal ventral hippocampal lesions. *Behavioural Brain
Research*, 231(1), 97–104.

Malik, R., & Johnston, D. (2017). Dendritic GIRK Channels Gate the Integration
Window, Plateau Potentials, and Induction of Synaptic Plasticity in Dorsal But Not
Ventral CA1 Neurons. *The Journal of Neuroscience: The Official Journal of the
Society for Neuroscience*, 37(14), 3940–3955.

Malik, R., Li, Y., Schamiloglu, S., & Sohal, V. S. (2022). Top-down control of
hippocampal signal-to-noise by prefrontal long-range inhibition. *Cell*, 185(9), 1602–
1617.e17.

Maren, S., & Holt, W. G. (2004). Hippocampus and Pavlovian fear conditioning in rats:
muscimol infusions into the ventral, but not dorsal, hippocampus impair the
acquisition of conditional freezing to an auditory conditional stimulus. *Behavioral
Neuroscience*, 118(1), 97–110.

Masurkar, A. V., Srinivas, K. V., Brann, D. H., Warren, R., Lowes, D. C., & Siegelbaum,
S. A. (2017). Medial and Lateral Entorhinal Cortex Differentially Excite Deep versus
Superficial CA1 Pyramidal Neurons. *Cell Reports*, 18(1), 148–160.

McClelland, J. L., & Goddard, N. H. (1996). Considerations arising from a
complementary learning systems perspective on hippocampus and neocortex.
Hippocampus, 6(6), 654–665.

- McEchron, M. D., & Disterhoft, J. F. (1997). Sequence of single neuron changes in CA1 hippocampus of rabbits during acquisition of trace eyeblink conditioned responses. *Journal of Neurophysiology*, 78(2), 1030–1044.
- McHugh, T. J., Jones, M. W., Quinn, J. J., Balthasar, N., Coppari, R., Elmquist, J. K., Lowell, B. B., Fanselow, M. S., Wilson, M. A., & Tonegawa, S. (2007). Dentate gyrus NMDA receptors mediate rapid pattern separation in the hippocampal network. *Science*, 317(5834), 94–99.
- McNaughton, B. L., Battaglia, F. P., Jensen, O., Moser, E. I., & Moser, M.-B. (2006). Path integration and the neural basis of the “cognitive map.” *Nature Reviews Neuroscience*, 7(8), 663–678.
- McNaughton, B. L., & Morris, R. G. M. (1987). Hippocampal synaptic enhancement and information storage within a distributed memory system. In *Trends in Neurosciences* (Vol. 10, Issue 10, pp. 408–415). [https://doi.org/10.1016/0166-2236\(87\)90011-7](https://doi.org/10.1016/0166-2236(87)90011-7)
- Miller, J. F., Neufang, M., Solway, A., Brandt, A., Trippel, M., Mader, I., Hefft, S., Merkow, M., Polyn, S. M., Jacobs, J., Kahana, M. J., & Schulze-Bonhage, A. (2013). Neural activity in human hippocampal formation reveals the spatial context of retrieved memories. *Science*, 342(6162), 1111–1114.
- Milner, B., Squire, L. R., & Kandel, E. R. (1998). Cognitive neuroscience and the study of memory. *Neuron*, 20(3), 445–468.
- Ming, G.-L., & Song, H. (2011). Adult Neurogenesis in the Mammalian Brain: Significant Answers and Significant Questions. In *Neuron* (Vol. 70, Issue 4, pp. 687–702). <https://doi.org/10.1016/j.neuron.2011.05.001>

- Mitchell, S. J., & Ranck, J. B., Jr. (1980). Generation of theta rhythm in medial entorhinal cortex of freely moving rats. *Brain Research*, 189(1), 49–66.
- Moser, E., Moser, M. B., & Andersen, P. (1993). Spatial learning impairment parallels the magnitude of dorsal hippocampal lesions, but is hardly present following ventral lesions. *The Journal of Neuroscience: The Official Journal of the Society for Neuroscience*, 13(9), 3916–3925.
- Naber, P. A., Lopes da Silva, F. H., & Witter, M. P. (2001). Reciprocal connections between the entorhinal cortex and hippocampal fields CA1 and the subiculum are in register with the projections from CA1 to the subiculum. *Hippocampus*, 11(2), 99–104.
- Niediek, J., & Bain, J. (2014). Human single-unit recordings reveal a link between place-cells and episodic memory. *Frontiers in Systems Neuroscience*, 8, 158.
- O'Keefe, J., & Dostrovsky, J. (1971). The hippocampus as a spatial map. Preliminary evidence from unit activity in the freely-moving rat. In *Brain Research* (Vol. 34, Issue 1, pp. 171–175). [https://doi.org/10.1016/0006-8993\(71\)90358-1](https://doi.org/10.1016/0006-8993(71)90358-1)
- O'Keefe, J., & Nadel, L. (1978). *The Hippocampus as a Cognitive Map*. Oxford University Press, USA.
- O'Keefe, J., & Recce, M. L. (1993). Phase relationship between hippocampal place units and the EEG theta rhythm. *Hippocampus*, 3(3), 317–330.
- Okuyama, T., Kitamura, T., Roy, D. S., Itohara, S., & Tonegawa, S. (2016). Ventral CA1 neurons store social memory. *Science*, 353(6307), 1536–1541.
- Oliveira, C. L. de, de Oliveira, C. L., Bolzan, J. A., Surget, A., & Belzung, C. (2020). Do antidepressants promote neurogenesis in adult hippocampus? A systematic review

- and meta-analysis on naive rodents. In *Pharmacology & Therapeutics* (Vol. 210, p. 107515). <https://doi.org/10.1016/j.pharmthera.2020.107515>
- Overstreet-Wadiche, L. S., & Westbrook, G. L. (2006). Functional maturation of adult-generated granule cells. In *Hippocampus* (Vol. 16, Issue 3, pp. 208–215). <https://doi.org/10.1002/hipo.20152>
- Padilla-Coreano, N., Bolkan, S. S., Pierce, G. M., Blackman, D. R., Hardin, W. D., Garcia-Garcia, A. L., Spellman, T. J., & Gordon, J. A. (2016). Direct Ventral Hippocampal-Prefrontal Input Is Required for Anxiety-Related Neural Activity and Behavior. *Neuron*, *89*(4), 857–866.
- Padilla-Coreano, N., Canetta, S., Mikofsky, R. M., Alway, E., Passecker, J., Myroshnychenko, M. V., Garcia-Garcia, A. L., Warren, R., Teboul, E., Blackman, D. R., Morton, M. P., Hupalo, S., Tye, K. M., Kellendonk, C., Kupferschmidt, D. A., & Gordon, J. A. (2019). Hippocampal-Prefrontal Theta Transmission Regulates Avoidance Behavior. *Neuron*, *104*(3), 601–610.e4.
- Parfitt, G. M., Nguyen, R., Bang, J. Y., Aqrabawi, A. J., Tran, M. M., Seo, D. K., Richards, B. A., & Kim, J. C. (2017). Bidirectional Control of Anxiety-Related Behaviors in Mice: Role of Inputs Arising from the Ventral Hippocampus to the Lateral Septum and Medial Prefrontal Cortex. *Neuropsychopharmacology: Official Publication of the American College of Neuropsychopharmacology*, *42*(8), 1715–1728.
- Pavlidis, C., Greenstein, Y. J., Grudman, M., & Winson, J. (1988). Long-term potentiation in the dentate gyrus is induced preferentially on the positive phase of theta-rhythm. *Brain Research*, *439*(1-2), 383–387.

- Pennartz, C. M. A., Lee, E., Verheul, J., Lipa, P., Barnes, C. A., & McNaughton, B. L. (2004). The ventral striatum in off-line processing: ensemble reactivation during sleep and modulation by hippocampal ripples. *The Journal of Neuroscience: The Official Journal of the Society for Neuroscience*, *24*(29), 6446–6456.
- Pfeiffer, B. E., & Foster, D. J. (2013). Hippocampal place-cell sequences depict future paths to remembered goals. *Nature*, *497*(7447), 74–79.
- Pitkänen, A., Pikkarainen, M., Nurminen, N., & Ylinen, A. (2000). Reciprocal connections between the amygdala and the hippocampal formation, perirhinal cortex, and postrhinal cortex in rat. A review. *Annals of the New York Academy of Sciences*, *911*, 369–391.
- Poppenk, J., Evensmoen, H. R., Moscovitch, M., & Nadel, L. (2013). Long-axis specialization of the human hippocampus. In *Trends in Cognitive Sciences* (Vol. 17, Issue 5, pp. 230–240). <https://doi.org/10.1016/j.tics.2013.03.005>
- Pothuizen, H. H. J., Zhang, W.-N., Jongen-Rêlo, A. L., Feldon, J., & Yee, B. K. (2004). Dissociation of function between the dorsal and the ventral hippocampus in spatial learning abilities of the rat: a within-subject, within-task comparison of reference and working spatial memory. *The European Journal of Neuroscience*, *19*(3), 705–712.
- Poucet, B., Thinus-Blanc, C., & Muller, R. U. (1994). Place cells in the ventral hippocampus of rats. *Neuroreport*, *5*(16), 2045–2048.
- Rajaseethupathy, P., Sankaran, S., Marshel, J. H., Kim, C. K., Ferenczi, E., Lee, S. Y., Berndt, A., Ramakrishnan, C., Jaffe, A., Lo, M., Liston, C., & Deisseroth, K. (2015).

- Projections from neocortex mediate top-down control of memory retrieval. *Nature*, 526(7575), 653–659.
- Riaz, S., Schumacher, A., Sivagurunathan, S., Van Der Meer, M., & Ito, R. (2017). Ventral, but not dorsal, hippocampus inactivation impairs reward memory expression and retrieval in contexts defined by proximal cues. *Hippocampus*, 27(7), 822–836.
- Risold, P. Y., & Swanson, L. W. (1996). Structural evidence for functional domains in the rat hippocampus. *Science*, 272(5267), 1484–1486.
- Rogers, J. L., Hunsaker, M. R., & Kesner, R. P. (2006). Effects of ventral and dorsal CA1 subregional lesions on trace fear conditioning. *Neurobiology of Learning and Memory*, 86(1), 72–81.
- Rogers, J. L., & Kesner, R. P. (2006). Lesions of the dorsal hippocampus or parietal cortex differentially affect spatial information processing. *Behavioral Neuroscience*, 120(4), 852–860.
- Rolls, E. T. (2013a). A quantitative theory of the functions of the hippocampal CA3 network in memory. *Frontiers in Cellular Neuroscience*, 7, 98.
- Rolls, E. T. (2013b). The mechanisms for pattern completion and pattern separation in the hippocampus. *Frontiers in Systems Neuroscience*, 7, 74.
- Rosenbaum, R. S., Priselac, S., Köhler, S., Black, S. E., Gao, F., Nadel, L., & Moscovitch, M. (2000). Remote spatial memory in an amnesic person with extensive bilateral hippocampal lesions. *Nature Neuroscience*, 3(10), 1044–1048.

- Rotenberg, A., Mayford, M., Hawkins, R. D., Kandel, E. R., & Muller, R. U. (1996). Mice expressing activated CaMKII lack low frequency LTP and do not form stable place cells in the CA1 region of the hippocampus. *Cell*, *87*(7), 1351–1361.
- Rothschild, G., Eban, E., & Frank, L. M. (2017). A cortical-hippocampal-cortical loop of information processing during memory consolidation. *Nature Neuroscience*, *20*(2), 251–259.
- Royer, S., Sirota, A., Patel, J., & Buzsáki, G. (2010). Distinct representations and theta dynamics in dorsal and ventral hippocampus. *The Journal of Neuroscience: The Official Journal of the Society for Neuroscience*, *30*(5), 1777–1787.
- Sahay, A., Scobie, K. N., Hill, A. S., O'Carroll, C. M., Kheirbek, M. A., Burghardt, N. S., Fenton, A. A., Dranovsky, A., & Hen, R. (2011). Increasing adult hippocampal neurogenesis is sufficient to improve pattern separation. *Nature*, *472*(7344), 466–470.
- Santarelli, L., Saxe, M., Gross, C., Surget, A., Battaglia, F., Dulawa, S., Weisstaub, N., Lee, J., Duman, R., Arancio, O., Belzung, C., & Hen, R. (2003). Requirement of Hippocampal Neurogenesis for the Behavioral Effects of Antidepressants. In *Science* (Vol. 301, Issue 5634, pp. 805–809).
<https://doi.org/10.1126/science.1083328>
- Scharfman, H. E. (2016). The enigmatic mossy cell of the dentate gyrus. *Nature Reviews. Neuroscience*, *17*(9), 562–575.
- Scharfman, H. E., & Myers, C. E. (2012). Hilar mossy cells of the dentate gyrus: a historical perspective. *Frontiers in Neural Circuits*, *6*, 106.

- Schloesser, R. J., Manji, H. K., & Martinowich, K. (2009). Suppression of adult neurogenesis leads to an increased hypothalamo-pituitary-adrenal axis response. *Neuroreport*, *20*(6), 553–557.
- Segal, M., Disterhoft, J. F., & Olds, J. (1972). Hippocampal unit activity during classical aversive and appetitive conditioning. *Science*, *175*(4023), 792–794.
- Senzai, Y., & Buzsáki, G. (2017). Physiological Properties and Behavioral Correlates of Hippocampal Granule Cells and Mossy Cells. *Neuron*, *93*(3), 691–704.e5.
- Siegle, J. H., & Wilson, M. A. (2014). Enhancement of encoding and retrieval functions through theta phase-specific manipulation of hippocampus. *eLife*, *3*, e03061.
- Skaggs, W. E., McNaughton, B. L., Wilson, M. A., & Barnes, C. A. (1996). Theta phase precession in hippocampal neuronal populations and the compression of temporal sequences. *Hippocampus*, *6*(2), 149–172.
- Soltesz, I., Bourassa, J., & Deschênes, M. (1993). The behavior of mossy cells of the rat dentate gyrus during theta oscillations in vivo. *Neuroscience*, *57*(3), 555–564.
- Sosa, M., Joo, H. R., & Frank, L. M. (2020). Dorsal and Ventral Hippocampal Sharp-Wave Ripples Activate Distinct Nucleus Accumbens Networks. *Neuron*, *105*(4), 725–741.e8.
- Squire, L. R. (1992). Memory and the hippocampus: a synthesis from findings with rats, monkeys, and humans. *Psychological Review*, *99*(2), 195–231.
- Stefanini, F., Kushnir, L., Jimenez, J. C., Jennings, J. H., Woods, N. I., Stuber, G. D., Kheirbek, M. A., Hen, R., & Fusi, S. (2020). A Distributed Neural Code in the Dentate Gyrus and in CA1. *Neuron*, *107*(4), 703–716.e4.

- Stein, J. F. (1989). REPRESENTATION OF EGOCENTRIC SPACE IN THE POSTERIOR PARIETAL CORTEX. In *Quarterly Journal of Experimental Physiology* (Vol. 74, Issue 5, pp. 583–606). <https://doi.org/10.1113/expphysiol.1989.sp003314>
- Strange, B. A., Witter, M. P., Lein, E. S., & Moser, E. I. (2014). Functional organization of the hippocampal longitudinal axis. *Nature Reviews. Neuroscience*, 15(10), 655–669.
- Stujenske, J. M., Likhtik, E., Topiwala, M. A., & Gordon, J. A. (2014). Fear and safety engage competing patterns of theta-gamma coupling in the basolateral amygdala. *Neuron*, 83(4), 919–933.
- Surget, A., Tanti, A., Leonardo, E. D., Laugeray, A., Rainer, Q., Touma, C., Palme, R., Griebel, G., Ibarguen-Vargas, Y., Hen, R., & Belzung, C. (2011). Antidepressants recruit new neurons to improve stress response regulation. *Molecular Psychiatry*, 16(12), 1177–1188.
- Talassi, E., Cipriani, G., Bianchetti, A., & Trabucchi, M. (2007). Personality changes in Alzheimer's disease. *Aging & Mental Health*, 11(5), 526–531.
- Tannenholz, L., Jimenez, J. C., & Kheirbek, M. A. (2014). Local and regional heterogeneity underlying hippocampal modulation of cognition and mood. *Frontiers in Behavioral Neuroscience*, 8, 147.
- Tanti, A., Rainer, Q., Minier, F., Surget, A., & Belzung, C. (2012). Differential environmental regulation of neurogenesis along the septo-temporal axis of the hippocampus. *Neuropharmacology*, 63(3), 374–384.
- Taxidis, J., Pnevmatikakis, E. A., Dorian, C. C., Mylavarapu, A. L., Arora, J. S., Samadian, K. D., Hoffberg, E. A., & Golshani, P. (2020). Differential Emergence

- and Stability of Sensory and Temporal Representations in Context-Specific Hippocampal Sequences. *Neuron*, 108(5), 984–998.e9.
- Thompson, C. L., Pathak, S. D., Jeromin, A., Ng, L. L., MacPherson, C. R., Mortrud, M. T., Cusick, A., Riley, Z. L., Sunkin, S. M., Bernard, A., Puchalski, R. B., Gage, F. H., Jones, A. R., Bajic, V. B., Hawrylycz, M. J., & Lein, E. S. (2008). Genomic anatomy of the hippocampus. *Neuron*, 60(6), 1010–1021.
- Tolman, E. C. (1948). Cognitive maps in rats and men. *Psychological Review*, 55(4), 189–208.
- Trent, N. L., & Menard, J. L. (2010). The ventral hippocampus and the lateral septum work in tandem to regulate rats' open-arm exploration in the elevated plus-maze. *Physiology & Behavior*, 101(1), 141–152.
- Treves, A., & Rolls, E. T. (1992). Computational constraints suggest the need for two distinct input systems to the hippocampal CA3 network. *Hippocampus*, 2(2), 189–199.
- Treves, A., & Rolls, E. T. (1994). Computational analysis of the role of the hippocampus in memory. *Hippocampus*, 4(3), 374–391.
- Trivedi, M. (2004). Lesions of the ventral hippocampus, but not the dorsal hippocampus, impair conditioned fear expression and inhibitory avoidance on the elevated T-maze. In *Neurobiology of Learning and Memory* (Vol. 81, Issue 3, pp. 172–184). <https://doi.org/10.1016/j.nlm.2004.02.005>
- Trompoukis, G., & Papatheodoropoulos, C. (2020). Dorsal-Ventral Differences in Modulation of Synaptic Transmission in the Hippocampus. *Frontiers in Synaptic Neuroscience*, 12, 24.

- Tronel, S., Belnoue, L., Grosjean, N., Revest, J.-M., Piazza, P.-V., Koehl, M., & Abrous, D. N. (2012). Adult-born neurons are necessary for extended contextual discrimination. *Hippocampus*, *22*(2), 292–298.
- Tulving, E., Donaldson, W., & Bower, G. H. (1972). *Organization of Memory*.
- Vanderwolf, C. H. (1969). Hippocampal electrical activity and voluntary movement in the rat. *Electroencephalography and Clinical Neurophysiology*, *26*(4), 407–418.
- van Groen, T. (2001). Entorhinal cortex of the mouse: Cytoarchitectonical organization. In *Hippocampus* (Vol. 11, Issue 4, pp. 397–407). <https://doi.org/10.1002/hipo.1054>
- van Strien, N. M., Cappaert, N. L. M., & Witter, M. P. (2009). The anatomy of memory: an interactive overview of the parahippocampal-hippocampal network. *Nature Reviews. Neuroscience*, *10*(4), 272–282.
- Verney, C., Baulac, M., Berger, B., Alvarez, C., Vigny, A., & Helle, K. B. (1985). Morphological evidence for a dopaminergic terminal field in the hippocampal formation of young and adult rat. *Neuroscience*, *14*(4), 1039–1052.
- Verwer, R. W., Meijer, R. J., Van Uum, H. F., & Witter, M. P. (1997). Collateral projections from the rat hippocampal formation to the lateral and medial prefrontal cortex. *Hippocampus*, *7*(4), 397–402.
- Wallenstein, G. V., Eichenbaum, H., & Hasselmo, M. E. (1998). The hippocampus as an associator of discontinuous events. *Trends in Neurosciences*, *21*(8), 317–323.
- Willshaw, D. J., Dayan, P., & Morris, R. G. M. (2015). Memory, modelling and Marr: a commentary on Marr (1971) “Simple memory: a theory of archicortex.” *Philosophical Transactions of the Royal Society of London. Series B, Biological Sciences*, *370*(1666). <https://doi.org/10.1098/rstb.2014.0383>

- Wilson, M. A., & McNaughton, B. L. (1994). Reactivation of hippocampal ensemble memories during sleep. *Science*, *265*(5172), 676–679.
- Wirtshafter, H. S., & Disterhoft, J. F. (2022). Multi-Day Calcium Imaging of CA1 Hippocampus in Freely Moving Rats Reveals a High Preponderance of Place Cells with Consistent Place Fields. *The Journal of Neuroscience: The Official Journal of the Society for Neuroscience*. <https://doi.org/10.1523/JNEUROSCI.1750-21.2022>
- Witter, M. P. (2007). The perforant path: projections from the entorhinal cortex to the dentate gyrus. *Progress in Brain Research*, *163*, 43–61.
- Witter, M. P., Doan, T. P., Jacobsen, B., Nilssen, E. S., & Ohara, S. (2017). Architecture of the Entorhinal Cortex A Review of Entorhinal Anatomy in Rodents with Some Comparative Notes. *Frontiers in Systems Neuroscience*, *11*, 46.
- Witter, M. P., Groenewegen, H. J., Lopes da Silva, F. H., & Lohman, A. H. (1989). Functional organization of the extrinsic and intrinsic circuitry of the parahippocampal region. *Progress in Neurobiology*, *33*(3), 161–253.
- Wixted, J. T., Goldinger, S. D., Squire, L. R., Kuhn, J. R., Papesh, M. H., Smith, K. A., Treiman, D. M., & Steinmetz, P. N. (2018). Coding of episodic memory in the human hippocampus. *Proceedings of the National Academy of Sciences of the United States of America*, *115*(5), 1093–1098.
- Wood, E. R., Dudchenko, P. A., & Eichenbaum, H. (1999). The global record of memory in hippocampal neuronal activity. *Nature*, *397*(6720), 613–616.
- Woods, N. I., Vaaga, C. E., Chatzi, C., Adelson, J. D., Collie, M. F., Perederiy, J. V., Tovar, K. R., & Westbrook, G. L. (2018). Preferential Targeting of Lateral Entorhinal

Inputs onto Newly Integrated Granule Cells. *The Journal of Neuroscience: The Official Journal of the Society for Neuroscience*, 38(26), 5843–5853.

Yasuda, M., & Mayford, M. R. (2006). CaMKII activation in the entorhinal cortex disrupts previously encoded spatial memory. *Neuron*, 50(2), 309–318.

Yeates, D. C. M., Ussling, A., Lee, A. C. H., & Ito, R. (2020). Double dissociation of learned approach-avoidance conflict processing and spatial pattern separation along the dorsoventral axis of the dentate gyrus. *Hippocampus*, 30(6), 596–609.

Yeh, C.-Y., Asrican, B., Moss, J., Quintanilla, L. J., He, T., Mao, X., Cassé, F., Gebara, E., Bao, H., Lu, W., Toni, N., & Song, J. (2018). Mossy Cells Control Adult Neural Stem Cell Quiescence and Maintenance through a Dynamic Balance between Direct and Indirect Pathways. *Neuron*, 99(3), 493–510.e4.

Zeidman, P., & Maguire, E. A. (2016). Anterior hippocampus: the anatomy of perception, imagination and episodic memory. In *Nature Reviews Neuroscience* (Vol. 17, Issue 3, pp. 173–182). <https://doi.org/10.1038/nrn.2015.24>

Ziv, Y., Burns, L. D., Cocker, E. D., Hamel, E. O., Ghosh, K. K., Kitch, L. J., El Gamal, A., & Schnitzer, M. J. (2013). Long-term dynamics of CA1 hippocampal place codes. *Nature Neuroscience*, 16(3), 264–266.

Chapter 2: Neural dynamics underlying associative learning in the dorsal and ventral hippocampus

Introduction

As a child, an unexpected encounter with an ice cream truck can be a highly rewarding experience. To better predict the circumstances that led to this occurrence, the brain gathers information surrounding the incident, from broad cues associated with the availability of reward (the presence of music, the neighborhood in which the encounter occurred), to more detailed stimulus representations (the specific melody played, the precise location of the encounter), to the positive outcome from the experience of consuming ice cream. Following repeated encounters, the most predictive features are identified and used to inform behavior, such as grabbing your parents' money and running outside when the learned melody is heard.

The above illustrates a fundamental objective of the brain: to extract the underlying structure of the world and model its causal relationships. Moreover, the brain must be able to flexibly update these models as cue-outcome relationships change (e.g., when the melody is replaced, or the truck no longer carries your favorite flavors). While the importance of examining the population dynamics underlying cognitive processes is becoming increasingly appreciated (Ahmed et al., 2020; Ebitz & Hayden, 2021; Stefanini et al., 2020), it is still unclear how learned associations are represented at the population level and how these representations change as a function of learning.

One area heavily implicated in encoding learned associations is the hippocampus. Genetic, anatomical, and functional data suggest the dorsal and ventral subdivisions of the rodent HPC (dHPC and vHPC) play distinct roles when learning

about the world (Fanselow & Dong, 2010; Strange et al., 2014). Previous studies show neuronal responses in dHPC are relatively specific, encoding properties such as position within an environment, elapsed time, the identity of individual stimuli, and conjunctive representations such as object-location couplings (Kay & Frank, 2019; Komorowski et al., 2009; O'Keefe & Dostrovsky, 1971; Pastalkova et al., 2008; Taxis et al., 2020; Wood et al., 2000; Yu et al., 2018). In contrast, vHPC representations respond to more abstract elements that generalize across distinct objects and events (Harland et al., 2018; Knudsen & Wallis, 2021; Komorowski et al., 2013; Royer et al., 2010), which may reflect the overall valence of an experience (Cicchi et al., 2015; Jimenez et al., 2018). Thus, during learning detailed representations by dHPC may support the formation of associative memories based on local cues, such as the precise identity of an object in an environment, while broad vHPC representations may generalize knowledge across multiple experiences and/or attach significance to contexts in which associations occur.

While dHPC and vHPC may encode unique features of an explored environment, it remains unknown how these areas may be differentially engaged during the encoding of associative memories. Furthermore, how neural responses are further transformed when learned relationships are manipulated and updated is also unclear.

Here, we used 2-photon in vivo imaging of population activity in dCA1 or vCA1 to track the activity of the same neurons across multiple stages of learning as mice learned to associate odor stimuli with appetitive or aversive outcomes. This allowed us to examine how task-related information is differentially represented across the dorsoventral hippocampal axis and how these representations evolve with learning.

Further, we examined the stability of representations across training, the influence of different outcomes on these encoding properties, and how neural representations adapt when cue-outcome relationships are altered.

Results

Representations of odor identity across the dorsoventral axis of CA1

We imaged odor-evoked neural responses in dCA1 and vCA1 using high resolution 2-photon microscopy in mice expressing the calcium indicator GCaMP6f (**Figure 2.1a-c**). In dCA1, we found that both odors elicited robust neuronal responses (**Figure 2.1e**). To examine whether population responses were distinct for each odor, we trained a linear classifier to distinguish trial-type activity patterns (**Figure 2.1f**) and then tested classification accuracy using held-out trials. As the number of dimensions (ie, neurons) influences decoder performance, this parameter was held constant across comparisons (**Supplementary Table 1**). Decoding analyses showed that odor identity could be decoded from dCA1 population activity with high accuracy (**Figure 2.1g and S1-2**). Moreover, odor-evoked population responses could be accurately discriminated from ITI (baseline) activity (**Figure 2.1h-i**). Conversely, odor responses in vCA1 neurons were significantly weaker than in dCA1, and linear decoders performed significantly worse compared to dCA1 when reading out trial identity or discriminating odor-evoked activity from baseline activity (**Figure 2.1e-i and S1 -2**). Importantly, the number of neurons used for decoding was held constant across dCA1 and vCA1. While there was no difference in how well each odor could be discriminated from baseline activity for dCA1, we did observe a significant difference between odors for vCA1

(dCA1: Mann-Whitney $U = 70.5$, $p = 0.13$; vCA1: $U = 18$, $p = 0.017$), with the eventual CS- odor (odor 2) showing higher decoding accuracy. However, accuracy for this odor was still well below that observed for dCA1. Collectively, these data suggest that, during initial exposure to odorants that lack behavioral relevance or meaningful associations, odor identities are strongly represented in dCA1 but less so in vCA1.

Attaching behavioral significance to odors enhances their representations in vCA1

Given the role of the ventral hippocampus in emotional and motivational processes (Tannenholz et al., 2014), we reasoned that odor representations may be enhanced in vCA1 if paired with a salient outcome. To disambiguate odor representations from potential reward anticipation signals, we used a two-odor trace appetitive conditioning paradigm wherein the CS+ odor was separated from sucrose reward delivery by a 2s trace period. Following ~4 days of training, mice displayed anticipatory licks during the CS+ trace period, with minimal licking during all other task periods (**Figure 2.2a-d**).

In vCA1, learning of the odor-reward association was accompanied by an overall increase in mean activity during the CS+ odor presentation (**Figure 2.2e and S2a-c**) and heightened ability to discriminate population activity during the odor period (**Figure 2.2g,h and S2e**). This increase in trial-type decoding accuracy in vCA1 appeared to be driven by altered processing of the now-salient CS+ odor, as both odor-responsivity (**Figure 2.2e and S2c**) and accuracy for decoding odor period vs baseline activity (**Figure 2.2i,j, S2d**) increased with learning for the CS+ odor, but not CS-odor. Thus, assigning value to a stimulus leads to increased odor-evoked activity and encoding in ventral CA1. This was in contrast to dCA1, where odor decoding accuracy was high

prior to training and remained so with learning (**Figure 2.2g,h and S4a,c**). However, dCA1 did show a learning-related increase in the proportion of cells responsive to the CS+ odor, but not CS- odor (**S3d**), suggesting that stimulus representations in dCA1 may also be sensitive to perceived value.

We next examined representations in the trace period, during which learned animals anticipate reward availability. We found parallel changes in trace-period representations in dCA1 and vCA1 with learning (**Figure 2.2g-j and S4a-d**). Mean trace-period-evoked activity in both dCA1 and vCA1 markedly increased following CS+ delivery, but not CS- delivery. Correspondingly, CS+/CS- trial-type decoding accuracy during the trace period was significantly higher in both regions following learning. These trace-period representations emerged in concert with the initial signs of behavioral learning (**S4e,f**), and could not be explained solely by licking behavior (**S3c**), and were distinct from odor-period representations (**Figure 2.2k**).

Together, these data suggest that a representation of odor identity is present in dCA1, independent of learning, while representations in vCA1 show greater dependence on learned behavioral significance. In addition, with learning both vCA1 and dCA1 are recruited during the trace period prior to reward delivery, seemingly encoding information related to the expectation of reward.

Learned representations of task elements are modality-independent and learning-dependent

We next determined whether our results in CA1 generalized to other stimulus modalities, and whether neuronal changes that emerged with training were indeed

learning dependent. For this, we trained a separate cohort of mice on a more difficult auditory cue discrimination task (**Figure 2.3A,B**), where an auditory cue (CS+) and a sucrose reward were separated by a 2s trace period, while a distinct CS- auditory stimulus was unrewarded. Reward delivery was contingent on licking during a 2-second reward availability window directly following the trace period. Unlike the odor-based task, which all animals quickly learned, mice took longer to learn this task (11.7 ± 1.9 days) with some failing to learn altogether (**Figure 2.3C and S5E**).

As with the olfactory-based task, CS+ activity during tone presentation was more accurately classified from baseline activity in vCA1 after learning (**Figure 2.3D,E and S5C**), and classification of CS+/CS- tone identities likewise improved with learning (**Figure 2.3F,G**). This suggests that CS+ and CS- representations become more distinct in vCA1 over the course of discrimination training, regardless of the CS modality. In line with the odor-based task, we also found that decoding of CS+/CS- during the trace period was improved with learning in both regions (**Figure 2.3D-G**).

Interestingly, although the CS+ and CS- tones could each be decoded from baseline activity with moderate accuracy in dCA1 (**Figure 3D,E**), tone identity could not be decoded accurately from dCA1 population activity either before or after learning (both ~50% accuracy; **Figure 3F,G**). This contrasts with odorant identities, which could be consistently decoded with high accuracy, and is likely due to the greater ethological salience of odors vs tones. Despite this lack of strong encoding of tones in dCA1, these results are consistent with our odor task in that learning enhances the separability of cues in vCA1, but not dCA1.

A subset of vCA1 mice (n=3) failed to learn the tone-based version of the task, even after 20 days of training. In these “nonlearners” we found classification accuracy of CS+/CS- trial type during the tone or trace periods did not change between Early and Late sessions (**S5F,G**). Thus, representations that emerge with learning are not simply driven by repeated exposure to task stimuli.

Learned odor representations in vCA1 are sensitive to extinction but can be rapidly reinstated

While imbuing a stimulus with value enhances its representation in vCA1, how might stimulus representations change upon extinction of the odor-reward contingency? Would vCA1 continue to exhibit strong representations of odor, perhaps reflecting an enduring memory of the CS-US association, or would decoding performance fall back to baseline levels, suggesting vCA1 signals track current stimulus value?

After mice learned the odor-reward association, we extinguished it, omitting reward from CS+ trials. Mice rapidly extinguished the conditioned response early in the first session of extinction (**Figure 2.4a-c**). In an extinction retrieval session 24 hours later, we found that odor classification accuracy resembled that of early, pre-learning sessions; that is, low in vCA1 but high in dCA1 (**Figure 2.4d,e and 6a**).

The following day we reinstated conditioned responses in a reacquisition session. Animals rapidly resumed anticipatory licking behavior during CS+ trials, indicating an intact memory of the rewarded task structure. Correspondingly, odor identity classification accuracy increased in vCA1 (**Figure 2.4d,e and S6b**). These data indicate that the discriminability of odor representations in vCA1, is sensitive to the current value associated with an odor.

Task representations initially reorganize with learning, then stabilize

To probe the stability of odor and trace representations across different phases of training, we applied a cross-session classifier to neurons tracked across sessions (**Figure 2.5a,b**). For this, a linear classifier was trained to discriminate trial type in one session, and classification accuracy was tested using data from a separate session. When examining the odor period, we found a cross-session decoder performed poorly across initial learning (Early vs Late) in vCA1, in line with our observations that odor decoding accuracy increases in late sessions (**Figure 2.5c**). In dCA1, although odor identities were reliably represented both before and after discrimination training, we found that a cross session decoder performed poorly across learning, indicating that, as in vCA1, odor representations in this region are transformed with learning. Cross-session decoding of CS+/CS- using trace-period activity from Early to Late sessions was poor for both dCA1 and vCA1, suggesting a change in trace-period representations with learning (**Figure 2.5c**).

We next used cross-session decoding to examine the stability of task representations once learned. Using data from cells tracked across Late and Reacquisition sessions, we found that odor- and trace-period representations remained relatively stable across extinction in both vCA1 and dCA1, as trial type could be accurately classified across sessions during both periods (**Figure 2.5c**). This contrasts with the instability of odor representations observed during initial learning and indicates that, once learned, representations of odor and trace are to a large extent stable across days and across the degradation and reinstatement of odor-reward contingencies, This was also true in the absence of any additional learning (ie, no extinction training

between sessions, as similar results were found in a separate cohort of mice that were imaged in an odor-reward learning task in Early/Late sessions and an additional session (Post) four days following the Late session (**S9g,h**) Cross-session decoding results mirrored our previous findings; decoding accuracy was significantly lower from Early/Late sessions compared to Late/Post. Collectively these results indicate that CA1 may be a storage site for these odor-outcome representations .

To further probe how population activity changed across training, we used multidimensionality scaling (MDS) to visualize the geometric architecture of the representations (**Figure 2.5d,e**). When examining vCA1 odor-period representations, we found that CS+ representations, and to a lesser extent CS- representations, were modified with initial learning (Early vs Late) but remained relatively stable across extinction sessions (Late vs Reacquisition: **Figure 2.5d**). Intriguingly, this was not the case for dCA1, where the euclidean distance between CS+ or CS- representations did not differ across sessions. Analysis of trace-period representations produced similar results for both dCA1 and vCA1. Here, CS- representations showed little separation throughout training, while CS+ representations displayed a large change with initial learning that then stabilized across Late and Reacquisition sessions (**Figure 2.5e**). Analysis of single-cell responses showed a similar pattern; high turnover in the identity of odor- and trace-responsive cells during initial learning that subsequently stabilized across Late and Reacquisition sessions (**S7a-h**). Finally, we compared how decoder weights assigned to each cell changed across sessions in order to identify training-related changes in the contribution of individual cells to decoding. This analysis also revealed a stabilization of task representations following initial learning (**S7i,j**).

Long-timescale representations in vCA1

In vCA1, place fields are broader than those in dHPC, which has been hypothesized to allow vCA1 to contain global representations of behaviorally relevant contexts (Chockanathan & Padmanabhan, 2021; Harland et al., 2018; Jung et al., 1994; K. B. Kjelstrup et al., 2008). We likewise examined whether vCA1 contained more diffuse representations than dCA1 in our task as the mouse “moved” through the trial. We trained a linear classifier to discriminate trial type (CS+ vs CS-) using data from a single time bin, then tested classification accuracy on every other time bin (**Figure 2.6A**). We found that in vCA1, but not dCA1, there was a persistent trial-type representation throughout the trial duration, and trial-type could be decoded even when training and testing on time bins separated by +/- 5s seconds (**Figure 2.6B,C**). Importantly, this was only observed for time bins within the trial duration (1s post odor onset through 4s post reward delivery), and most prominently for sessions where the CS-US contingency had been learned and was actively being rewarded.

Pre-reward signals generalize across distinct predictive cues

Our results thus far show that, with learning, both hippocampal regions display strong representations during the odor and trace periods, and that these odor and trace representations can be well discriminated from one another. However, what information is being encoded during these epochs is not well elucidated by the two-odor task. Thus, to better address this question, we trained mice with four odor stimuli; two that were always followed by sucrose reward (CS1+ and CS2+), and two that were followed by no outcome (CS3- and CS4-). This design allowed us to directly test the similarity of

representations across trial types with distinct cue identities but the same outcome (**Figure 2.7a,b**).

We first tested how well a linear classifier could predict each of the four trial types using population activity during the odor or trace periods (**Figure 2.7c-f**). We found that, following learning (Late), odor identity could be predicted with high accuracy during the odor-delivery period for both dCA1 and vCA1. Conversely, although individual trial types remained discriminable during the trace period, classification accuracy was lower in both regions during this period, with classifier errors predominantly occurring between trial types with the same outcome (e.g., CS1+ vs CS2+). Thus, after learning, trace period activity is highly discriminable between trial type categories (CS+ vs CS-), but less so within each category.

The reduced decoding accuracy between CS1+ and CS2+ trial types during the trace period suggests a common signal across these trials. To more directly test this, we trained a linear classifier to discriminate activity between a reward-predictive trial type (e.g., CS1+) versus a non-predictive trial type (e.g., CS3-), then tested classification accuracy using data from the complementary trial types (CS2+ and CS4-), which the decoder had never seen (“outcome decoding”; see **Figure 2.7g**). Here, high decoding accuracy would indicate similar neural states across related trial types (e.g., CS1+ and CS2+).

Such outcome decoding was no better than chance for either task period prior to learning (**Figure 2.7h**). After learning, however, we found high outcome decoding accuracy during the trace period in both dCA1 and vCA1 (**Figure 2.7h**), further indicating that there exists a representation related to reward expectancy that is

independent of the identity of the cue that precedes it. Outcome decoding accuracy during the odor period was also high for vCA1, indicating that, in addition to encoding cue identity during this period, vCA1 populations simultaneously represent the predicted outcome associated with those cues. Together, these data suggest neural representations transition from encoding cue identity to outcome expectation in dCA1, while in vCA1 expected outcome is represented throughout the entire task period, and is multiplexed with information about specific cue identity during odor exposure. This was further corroborated by examining the similarity of population activity patterns across 1-second time bins that spanned the task duration (**Figure 2.7i**). Moreover, dimensionality reduction analysis returned results that were analogous with the decoding results above (**Figure 2.7j**).

Aversive conditioning and reversal learning

We next examined whether the neural changes associated with appetitive learning are also present during aversive (shock) conditioning, and how task representations might change when learned cue-outcome pairings were reversed. For this, we trained mice in an associative learning task with three novel CS odors (**Figure 2.8a**) that were paired with either sucrose (CS+rew), tail shock (CS+sh), or nothing (CS-). Once these pairings were well learned, we reversed the contingencies, where the previously rewarded odor was now paired with shock and vice-versa (**Figure 2.8c**).

Our behavioral data showed mice were able to more rapidly discriminate CS+ from CS- trials compared to the 2-odor task, likely because animals had formed a schema of the general task parameters during 2-odor training (ie, some odors are rewarded, others are not). Importantly, however, our 3-odor results examining CS+rew

and CS- trials closely mimicked 2-odor results, suggesting formation of a task schematic did not appreciably impact neural encoding of the learned task parameters.

Analysis of the odor period neural data revealed that CS+sh results were qualitatively similar to those for the CS+rew condition, with both trial types showing an increase in encoding with learning. (**Figure 2.8c and S10a-e**). Of note, however, was a difference in trace period decoding accuracy; although shock-trial accuracy increased with learning, it was significantly lower than reward (**Figure 2.8c**).

Following initial learning (Late session), animals were trained on reversed contingencies until anticipatory licks were only observed during the CS+rew trial (Late Reversal session. **Figure 2.8e**). Using neurons tracked across Late and Late Reversal, we first asked whether odor representations were dissociable from specific paired outcomes. We approached this using two methods: 1) training a classifier to discriminate odor period activity from ITI baseline activity during the final session prior to reversal (Late) and testing odor/ITI classification accuracy after the reversed contingencies had been learned (Late Reversal; **Figure 2.8g**); 2) training a linear classifier to discriminate reward and shock trials during Late and testing classification accuracy using Late Reversal data (**S10f-i**). In vCA1 and dCA1, both methods indicated that the neural representation for a specific odor remained intact regardless of whether the odor predicted sucrose or shock.

Next, we assessed whether outcome expectation signals during the trace period remained stable following reversal learning. For this, we performed the same analysis as above, but using trace period data. In both dCA1 and vCA1, the cross-session decoders performed well when decoding reward anticipation signals across reversal

(**Figure 2.8h and S10j**). These results mirrored our 4-odor results and suggest the hippocampus encodes a signal related to reward anticipation that is independent of the odor that precedes it. Surprisingly, there was not a conserved representation across reversal learning when anticipating shock (**Figure 6h and S10j**). Additional analyses revealed this was due to the absence of trace-period encoding during Late Reversal shock trials (**Figure 6f**). These results indicate that odor representations in both dCA1 and vCA1 are independent of the nature of the associated US, and that stable signals preceding reward, but not shock, emerge with learning in these regions.

Instrumental control of outcome increases task-related representations in associative learning

Why was pre-reward signaling so strong in dCA1 and vCA1, whereas pre-shock was not? A potential cause, we reasoned, may be the difference in the behavioral relevance of these outcomes; whereas reward trials required an operant response (licking), shock delivery was inescapable and thus behaviorally irrelevant. We thus developed a headfixed approach/avoidance task (**Figure 2.9a**). Here, mice headfixed on a running wheel were exposed to the 3-odor task from above, but could now run (> 4 cm/sec) during the odor and trace period to either escape shock or enable reward delivery, depending on the odor presented. Importantly, both shock escape and reward delivery required the same operant response.

Mice learned to escape shock and enable reward delivery over the course of ~5 days (**Figure 2.9b-d and S11a,b**), at which time we imaged neural activity. To minimize variability across trials and trial types, we only analyzed trials where animals displayed suprathreshold running (eg, avoided shock or earned sucrose reward). As opposed to our

previous data, we now were able to decode trace period activity with very high accuracy for shock trials (**Figure 2.9e**). Moreover, suprathreshold shock and reward trials could also be discriminated with high accuracy (**S11c,d**), indicating that the shared operant response (running) was not driving these results. Interestingly, CS- trace-period activity could be well discriminated from reward trials, but less so shock trials. Due to the fact that mice routinely ran above threshold during CS- trials (**Figure 2.9b and S11b**), it is possible that animals had not fully learned the task structure and/or interpreted the CS- odor as a potential cue for shock.

Finally, given recent reports describing the widespread influence of movement on neural activity (Musall et al., 2019; Stringer et al., 2019), we further probed whether running behavior may have contributed to our results. These analyses suggest running may indeed influence hippocampal activity, specifically in dCA1 (**S11e**). However, even in dCA1, high-speed vs low-speed running epochs during the ITI could only be weakly discriminated from one another (**S11g**), suggesting our main findings are driven by task properties and not running, per se, and that making an outcome behaviorally relevant may boost engagement of the hippocampus.

Discussion

Prior to cue-reward training, we found that dCA1 strongly encodes the identity of individual odors, in line with previous findings showing that environmental stimuli need not be paired with reward or other salient outcomes to be represented in dCA1 (Li et al., 2017; Taxidis et al., 2020). In contrast, vCA1 was less reactive to odors prior to training, and decoding of odor identity using population activity was inferior to that of dCA1. Instead, odor decoding was heavily influenced by salience, increasing for odors

predictive of salient outcomes (e.g., reward or shock), and decreasing in the absence of these outcomes (e.g., extinction). Such salience processing in vCA1 may be important for conveying stimulus-value information to the frontal cortex (Burton et al., 2009; Wikenheiser & Schoenbaum, 2016), passing information to emotional centers, such as the amygdala, for further processing (Felix-Ortiz et al., 2013; Graham et al., 2021; C. Xu et al., 2016), or alerting downstream regions mediating approach/avoidance behaviors (LeGates et al., 2018; Trouche et al., 2019). Although the accuracy of odor decoding in dCA1 was not influenced by salience (**Figure 2.4e**), at the single-cell level we found an increase in CS+ odor responsive cells following learning. These data extend previous findings showing the dorsal and intermediate HPC intensify activity for stimuli and locations with learned significance (Eichenbaum et al., 1987; Jin & Lee, 2021).

Following learning, odor representations remained relatively stable across sessions, including across extinction training, through three days devoid of additional training, or when the valence of the paired outcome was switched, indicating CA1 is a storage site for odor representations with learned relevance. Of note, however, across-session decoding was appreciably lower than within-session decoding. This would suggest that the level of representational drift between sessions is greater than that observed within a session similar, to what has been reported for CA1 spatial codes (Cai et al., 2016; Gonzalez et al., 2019; Hainmueller & Bartos, 2018; Kennedy & Shapiro, 2009; Mankin et al., 2012; Radvansky et al., 2021; Ziv et al., 2013). However, we also find that once the task is learned, the representation is stabilized as the level of drift is reduced as compared to changes seen early in learning, providing support for a stable hippocampal code after learning and in familiar environments (Liberti et al., 2022).

Specifically, what information is being encoded during odor presentation? Our results point to odor identity as the dominant representation in both dCA1 and vCA1. This is well supported by two findings: 1) two odors with the same outcome can be discriminated from one another with high accuracy, and 2) an odor's representation remains stable when its associated outcome is altered (eg, from reward to shock). In addition to odor identity representations, our “outcome decoding” analysis revealed that neuronal populations in vCA1 also multiplex information about the outcome associated with an odor. Consequently, a downstream recipient of these signals could not only decode whether reward is forthcoming, but at the same time the identity of the cue that preceded it, which may be important for updating cue value. Alternatively, it is possible that outcome and cue identity signals are each routed to distinct downstream targets (Beyeler et al., 2016; Nambodiri et al., 2019; Otis et al., 2017), consistent with vCA1 circuitry, where specialized functions are parsed across vCA1 projection pathways (Ciocchi et al., 2015; Jimenez et al., 2018; Shpokayte et al., 2022; Xia & Kheirbek, 2020; C. Xu et al., 2016).

In vCA1, we also found that a representation of outcome was not only present during odor delivery, but throughout the entire trial duration (**Figure 2.7i and S9f**), analogous to spatial representations in vCA1 that generalize across large swaths of space (Chockanathan & Padmanabhan, 2021; Jung et al., 1994; K. B. Kjelstrup et al., 2008). Thus, the broad firing observed in vCA1 during spatial exploration may reflect a more general property of this region that extends beyond representations of physical space. The currently observed representations stretching across cue, trace, and US periods may serve to link discontinuous cue-reward events, providing a neural substrate

through which credit can be assigned to the stimuli or actions that preceded reward delivery (Petter et al., 2018; Sosa & Giocomo, 2021; Stachenfeld et al., 2017). Alternatively, this signal may serve to “locate” the animal within the task space (Knudsen & Wallis, 2021), such as the task context currently being occupied (i.e., reward trial), and broadcast this information to downstream regions, such as the frontal cortex to retrieve context-relevant memories and guide behavior (Komorowski et al., 2013; Wikenheiser et al., 2017; Wikenheiser & Schoenbaum, 2016). These results are also in line with human studies of memory that suggest posterior (dorsal) HPC is associated with recall of detailed information, such as the temporal sequence of events, while anterior (ventral) HPC represents higher level information, such as the location of where the collection of events occurred (Harland et al., 2018; Poppenk et al., 2013)

In contrast to learning-related changes to cue representations that differed across hippocampal regions, neural transformations during the trace-period were remarkably similar across dorsal and ventral CA1. Here, both regions displayed robust increases in hippocampal recruitment and encoding of behaviorally relevant outcomes with learning. Changes in reward-related activation with learning has been well documented in HPC. In dCA1, neuronal activity has been shown to be modulated in rewarded tasks through various means, including accumulation of place fields at rewarded locations (Danielson et al., 2016; Dupret et al., 2010; Kaufman et al., 2020; Sato et al., n.d.; H. Xu et al., 2019) and, in tasks where goal location is dissociated from reward, an increase in out-of-field firing at the goal (Duvelle et al., 2019; Hok et al., 2007). Further, dedicated populations of goal-approach cells have been identified across the dorsoventral axis (Ciocchi et al., 2015; Eichenbaum et al., 1987; Gauthier &

Tank, 2018; Markus et al., 1995; Royer et al., 2010). Our results extend these findings beyond the spatial domain and show that ventral CA1 also contains a dedicated signal during reward anticipation that generalizes across predictive cues and is stable across days.

Considering the strong pre-reward signal observed with our appetitive conditioning tasks, we were surprised that anticipation of inescapable shock was only weakly encoded by both dCA1 and vCA1, despite robust activation of both regions in response to cue and shock deliveries. Moreover, shock anticipation signals were further diminished with subsequent training (from Late to Late Reversal sessions), eventually becoming indistinguishable from ITI activity. Although previous reports examining anticipation of aversive stimuli are mixed for dCA1 (Ahmed et al., 2020; MacDonald et al., 2013; Mount et al., 2021; Zhang et al., 2019), this finding is particularly surprising for vCA1, which is known to mediate anxiety and trace fear conditioning (Bangasser et al., 2006; Jimenez et al., 2018; K. G. Kjelstrup et al., 2002; McEchron et al., 1998). As the hippocampus is known to form a cognitive map of behaviorally relevant relationships, we reasoned a potential cause may be the lack of behavioral relevance of the inescapable shock (McKenzie et al., 2014; Nieh et al., 2021). Indeed, when mice were able to avoid shock via instrumental response, shock anticipation was strongly encoded in both dCA1 and vCA1. Whether the threat of shock (aversive) or anticipation of escape (potentially rewarding) best reflects animals' internal state during the trace period is uncertain, but it should be noted that sucrose and shock trials were well discriminated from one another during this time.

Our results show vast reorganization of hippocampal activity networks during associative learning. Unknown, however, are the mechanisms responsible for implementing this change. Dopaminergic, cholinergic, serotonergic, and adrenergic signals are all present to varying degrees across the DV axis of the hippocampus (Basu & Siegelbaum, 2015; Palacios-Filardo & Mellor, 2019), and each is integral for hippocampal plasticity and learning (Gu & Yakel, 2011; Kaufman et al., 2020; McNamara et al., 2014; Palacios-Filardo & Mellor, 2019; Teixeira et al., 2018). Locus coeruleus signaling, for one, mediates reward-dependent reorganization of place fields and may analogously promote changes in CS+ representations by integrating stimulus identity signals with reward-induced release of neuromodulators (Kaufman et al., 2020).

In addition to modulatory inputs, the HPC receives information from a multitude of extrahippocampal areas that may further shape CA1 network activity. The orbitofrontal cortex (OFC) is postulated to provide the hippocampus with information about expected outcomes (Wikenheiser & Schoenbaum, 2016), and may contribute to the reward-anticipation signals seen here. Input from the medial thalamus and/or amygdala to vCA1 could provide additional information regarding the learned salience or valence of stimuli (Beyeler et al., 2016; Felix-Ortiz et al., 2013; Gergues et al., 2020; Ramanathan et al., 2018). Additionally, we recently showed that odor representations in lateral entorhinal cortex (LEC) become more separable with learning (Woods et al., 2020) and may thus influence changing odor representations in CA1 across training.

Intrahippocampal signaling may also contribute to changes seen here. Although recurrent connectivity in CA1 is sparse (Deuchars & Thomson, 1996; Knowles & Schwartzkroin, 1981; Yang et al., 2014), learning is known to augment recurrent

interactions in the brain (Albieri et al., 2015; Biane et al., 2019) which can amplify inputs and induce attractor networks (Douglas & Martin, 2007; Lien & Scanziani, 2013), developments that could mediate the separation of odor representations we observed in vCA1. Additionally, inhibitory and astrocytic signaling may contribute to these changes (Bazargani & Attwell, 2016; Doron et al., 2022; Turi et al., 2019).

Recent work has highlighted functional differences that correlate with neurons' anatomical location within the CA1 network. For example, neural populations residing in superficial vs deep locations of CA1 display unique physiological properties and may also be preferentially tuned to distinct aspects of learning and environmental encoding (Danielson et al., 2016; Gava et al., 2021; Grosmark & Buzsáki, 2016; Navas-Olive et al., 2020; Soltesz & Losonczy, 2018). Future studies examining layer-specific differences in the representations reported here will be of considerable interest.

Finally, although previous reports have shown a positive relationship between movement and neural activity for a variety of “non-motor” brain regions (Musall et al., 2019; Stringer et al., 2019), we find mostly weak correlations between neural activity and licking, breathing or running behaviors in dCA1 and vCA1. Future studies can further elucidate how ongoing or task evoked behaviors such as postural adjustments and paw movement beyond running, or orofacial movements beyond licking or breathing may contribute to the hippocampal code for learning.

Here we have shown that dCA1 and vCA1 are largely attuned to different aspects of the world. In simplest terms, the hippocampus might thus be thought of as undergoing a shift from externally biased to internally biased encoding of environmental variables along the DV axis. Such a division of labor could facilitate learning (Harland et

al., 2018; Petter et al., 2018; Staresina & Davachi, 2009) and support the creation of a rich internal model that not only charts relationships in the world (dHPC), but also imbues certain relationships with meaning and emphasizes relevant stimuli (vHPC) (Collin et al., 2015; Harland et al., 2018; Shohamy & Wagner, 2008). Moreover, this simplified model is consistent with hippocampal lesion studies, where dHPC damage disproportionately affects declarative memory, and vHPC dysfunction is more closely associated with a failure to properly assign/update value, such as in PTSD, addiction, and depression (Fanselow & Dong, 2010; Strange et al., 2014).

On the other hand, we also saw a clear overlap in how some task variables are represented in dCA1 and vCA1. Why might these functionally distinct regions encode information that is seemingly redundant? As efferent connectivity patterns of dCA1 and vCA1 differ considerably (Bienkowski et al., 2018; Cenquizca & Swanson, 2007; Gergues et al., 2020; Strange et al., 2014), it is likely that each region is broadcasting this information to distinct downstream targets. When dCA1 and vCA1 outputs do converge onto the same region, these inputs may be handled differently, as appears to be the case with the NAc in reward learning (Sosa et al., 2020). Therefore, redundancy of representations across dorsal and ventral CA1 may be processed distinctly and uniquely influence ongoing operations. An interesting question for future inquiry is whether dCA1 and vCA1 inherit these overlapping representations from common or separate input source(s), or perhaps inform one another.

Methods

Mice

All procedures were conducted in accordance with the NIH Guide for the Care and Use of Laboratory Animals and institutional guidelines. Adult male C57BL/6J mice were supplied by Jackson Laboratory. Mice were kept on a 12-hour light cycle, with experiments conducted during the light portion.

Surgery

Animals were 11 – 15 weeks postnatal at time of surgery. Mice were anesthetized with 1.5% isoflurane with an O₂ flow rate of 1 L / min, and head-fixed in a stereotactic frame (David Kopf, Tujunga, CA). Eyes were lubricated with an ophthalmic ointment, and body temperature was maintained at 37°C with a warm water recirculator (Stryker, Kalamazoo, MI). The fur was shaved and incision site sterilized prior to beginning surgical procedures. Lidocaine, meloxicam, and slow-release buprenorphine were provided for analgesia.

GCaMP6f (2-odor and 3-odor experiments) or GCaMP8m (4-odor and approach-avoidance experiments) virus injection and GRIN lens implantation were conducted using methods previously described (Jimenez et al., 2018). Briefly, a craniotomy was made over the lens implantation site and dura was removed from the brain surface and cleaned with sterile saline and absorptive sponges (Fine Science Tools, Foster City, CA). A nanoject syringe (Drummond Scientific, Broomall, PA) was used to deliver GCaMP6f to vCA1 or dCA1 (left hemisphere for both). vCA1 coordinates were -3.16 A/P and -3.25 M/L. 150nl of virus was injected at each depth of -3.85, -3.55 and -3.3 (450nl total volume) with respect to bottom of skull at the medial edge of the craniotomy. dCA1

coordinates were -2 A/P, -1.65 M/L and -2.1 A/P, -1.45 M/L at depths -1.5, -1.25 D/V with respect to bregma. The needle was held in place for > 5 minutes prior to moving to the next D/V coordinate and remained in place for 10 minutes following the final injection before slowly removing from the brain. AAV1-SYN-GCaMP6f-WPRE-Sv40 (titer: $1.97E+13$) was supplied from University of Pennsylvania viral vector core and diluted 1:3 in 1x sterile PBS before injections. AAV1-SYN-jGCaMP8m-WPRE (titer: $2.4E+13$) was supplied from Addgene and diluted 1:3 in 1x sterile PBS before injections. For dCA1, prior to virus injection the overlying cortex was slowly aspirated until axonal fibers of the external capsule/alveus were visualized. Following virus injection, a 0.6mm (vCA1) or 1.0mm (dCA1) diameter GRIN lens (Inscopix, Palo Alto, CA) was slowly lowered in 0.1 mm D/V steps and then fixed to the skull with Metabond adhesive cement (Parkell, Edgewood, NY). vCA1 lens coordinates were -3.16 A/P, -3.5 M/L and -3.5 D/V (from bottom of skull at craniotomy; S1a). dCA1 lens coordinates were -2.05 A/P, -1.5 M/L, -0.95 D/V (from bregma; S1b). A custom-made titanium headbar was then attached to the skull using dental cement (Dentsply Sinora, Philadelphia, PA). A baseplate and cover (Inscopix, Palo Alto, CA) was also cemented on to protect the lens.

For dCA1 animals in the tone discrimination paradigm, a 3mm craniotomy was made, and the overlying cortex was aspirated until axonal fibers of the external capsule/alveus were visualized. The aspiration site was continuously irrigated with cold, sterile saline. Viral injections (120 nl per site) were performed at the same sites as above. A custom made dCA1 imaging window was implanted, which consisted of a 3mm round coverslip, #0 thickness (Warner Instruments, Hamden, CT) attached with

optical adhesive (#81, Norland Products, Cranbury, NJ) to a metal cannula containing 1/8" outer diameter and 1/16" in length (McMaster-Carr, Santa Fe Springs, CA). This window was carefully lowered into place, until it rested on top of the exposed tissue (S5b). The cannula was then cemented into place with Metabond adhesive, and a custom titanium headbar was cemented in place.

Verification of imaging sites and histological analysis

Dorsal and ventral CA1 imaging sites were verified in each animal included in final analysis (**S1a,b** and **S5a,b**). After all imaging sessions were completed, mice were injected with a lethal dose 2:1 ketamine/xylazine solution intraperitoneally. While the heart was still beating, mice were perfused transcardially using 4% PFA solution. Brains were extracted and placed in 4% PFA solution for 2-3 days to allow further fixation. After saturating with a 30% sucrose solution, coronal slices of 50-micron width were collected using a Leica SM2000 microtome. Slices were collected in 1x PBS solution and mounted onto glass slides, coverslipped with Fluoromount G with DAPI (Southern Biotech, Birmingham, AL).

Behavioral training

Four-to-six weeks following surgery, animals were handled and habituated to the experimenter, training environment and head fixation for one week. Following habituation, animals were water restricted to ~85-90% ad lib weight and underwent a 2-3 day pretraining period designed to introduce the liquid delivery apparatus, with free water rewards (~2 μ l each) intermittently delivered upon licking (up to 80 rewards in a 20 min session). Sucrose rewards (10% sucrose, 0.03% NaCl in water) were delivered

via a solenoid-gated gravity feed. Contact with a lick spout positioned in front of the mouth was measured using a capacitive touch MPR121 sensor (SparkFun, Boulder, CO). Stimulus delivery and sensor reading was controlled by an Arduino Mega with custom circuit boards (adapted from OpenMaze.org) and recorded via CoolTerm software. Once animals displayed consistent and motivated licking (80 rewards collected in a single session), lick training was complete and the pretraining odor exposure session was initiated the following day. Throughout training, animals were water restricted to ~85-90% ad lib weight. All training paradigms consisted of one training session/day, occurring at roughly the same time each day. Learning of the discrimination tasks was assessed using lick discriminability (d') for each session, which compares the rate of anticipatory licks during the trace period of CS+ trials with CS- trials:

$$d' = \frac{(\text{mean CS} + \text{licks} - \text{mean CS} - \text{licks})}{\frac{[\sigma(\text{CS} + \text{licks}) + \sigma(\text{CS} - \text{licks})]}{2}}$$

Learning was determined as a d' score > 1.5 for a session, with all Late session mice meeting this criterion.

Pretraining odor exposure

One day prior to conditioning, animals underwent a single session where they were passively exposed to neutral odors that would subsequently serve as CS+ and CS- odors during training. Each session consisted of 30 trials (15 of each odor) of 2 second odor presentations. There was no lick spout present during these sessions. The inter-trial interval between subsequent odor deliveries was chosen as a random sample from a uniform distribution between 17.5 and 27 seconds. Odors were delivered via a

custom-made olfactometer equipped with a mass flow controller (Alicat Scientific, Tucson, AZ) that maintained air flow at 2 liters per minute and prevented momentary pressure changes from solenoid valve switches (Clippard, Cincinnati, OH) upstream of the controller. Odors were delivered to mice via a customized nose cone, which contained an outlet where a gentle vacuum was applied to evacuate residual odor. Additionally, an ongoing charcoal filter vacuum system (Hydrobuilders Inc.) was used to evacuate any residual odors.

2-odor paradigm

Each associative learning session consisted of 120 trials (60 CS+ and 60 CS-, pseudo randomly presented). Two neutral odors served as CS+ and CS- cues (benzaldehyde or eugenol, 2s) with cue contingencies counterbalanced across mice. Presentation of the CS+ cue was followed by a 2s trace period and subsequent reward delivery (~2 μ l). No reward was available following the presentation of the CS- cue. Animals were not punished for off-target licking. The inter-trial interval between subsequent cues was chosen as a random sample from a uniform distribution between 17.5 and 27 seconds.

This task structure was administered over a period of ~7 days, in which day 1 and 4 were termed “Early” and “Late” learning, respectively. If an animal did not meet the learning criterion ($d' > 1.5$) on day 4 ($n=3$ animals), training continued until this criterion was met. The two days following the Late session extinction sessions, labeled as “Ext1” and “Ext2”, respectively, in which the odor-reward association was extinguished by removing the sucrose reward for CS+ trials (the lick spout remained in place). Ext2 was followed by a one-day reacquisition session, labeled as

“Reacquisition”, in which the sucrose reward was reintroduced for CS+ trials. A total of 11 vCA1 and 5 dCA1 animals were included in the data set.

2-tone paradigm

Each associative learning session consisted of 160 trials (80 CS+ and 80 CS-, pseudo randomly presented). Two auditory tones served as CS+ and CS- cues (2.5 kHz and 13kHz pulsing tones, 2s, 70 dBs) with cue contingencies counterbalanced across mice. Presentation of the CS+ cue was followed by a 2s trace period, then a 2s reward window which required a lick for sucrose reward delivery (~2 μ l, maximum one reward per trial). No reward was available following the presentation of the CS- cue. Animals were not punished for off-target licking. The inter-trial interval between subsequent cues was chosen as a random sample from a uniform distribution between 17.5 and 27 seconds. A total of 7 vCA1 and 2 dCA1 animals were included for analysis (a separate cohort of mice than that used for the odor-based experiments). In a subset of animals (n= 4 vCA1 and n = 2 dCA1), multiple z-planes were imaged across sessions. Imaging planes were separated by > 60 μ m to ensure there was no overlap of cells present across different z-planes.

3-odor paradigm

Following completion of 2-odor training, mice underwent 3-odor conditioning. Each session consisted of 120 trials (40 CS+rew. 40 CS+shock, 40 CS-, pseudo randomly presented). Three new neutral odors served as cues (o-toluidine, 2-heptanone, or +carvone; 2s). Presentation of the CS+ cue was followed by a 2s trace period and subsequent delivery of US (reward US = ~2 μ l 10% sucrose solution; shock

US = 0.125mA amplitude, 250ms duration). No US was presented following the presentation of the CS- cue. Animals were not punished for off-target licking. For reversal learning, CS+reward and CS+shock odor cues were switched, while the CS- odor remained the same. Shocks were delivered via a custom-made tail cuff driven by a precision animal shocker (Coulbourn Instruments, Holliston, MA). The inter-trial interval between subsequent cues was chosen as a random sample from a uniform distribution between 17.5 and 27 seconds. A total of 11 vCA1 and 3 dCA1 animals were included in the data set.

4-odor paradigm

A new cohort of animals without any previous discrimination training underwent 4-odor conditioning. Each session consisted of 120 trials (30 of each trial type, pseudo randomly presented). Four neutral odors served as cues (methylbutyrate, isoamyl acetate, eugenol, eucalyptol). Presentation of the CS+ cue was followed by a 2s trace period and subsequent delivery of 10% sucrose solution (~2 μ l). No US was presented following the presentation of the CS- cue. Animals were not punished for off-target licking. The inter-trial interval between subsequent cues was chosen as a random sample from a uniform distribution between 17 and 23 seconds. A total of 8 vCA1 and 5 dCA1 animals were included in the data set.

3-odor approach-avoidance paradigm.

Following 4-odor training, mice were habituated to head-fixed running on a 13 cm diameter wheel for ~20 minutes/day. Rotational speed was tracked using a rotary encoder (Yomo Electric Co., model E6A2) and assessed every 200 msec. Following 5-7 days of running wheel habituation, training began. Three new odors (o-toluidine, 2-heptanone, carvone) were used for this experiment. Each trial type (CS+ reward, CS+

shock, CS-) was presented 40 times/session, and were pseudo-randomly interleaved. Following ITI time elapse, animals were required to cease running for ≥ 0.6 sec before a trial could begin. Throughout training, a 4 cm/sec running speed threshold was used. Animals who displayed running speeds above this value at any point 0-3.4 sec following the onset of odor delivery would trigger reward delivery for CS+ reward trials, or cancel tail shock for CS+ shock trials. For this experiment, a lick spout remained out of reach of the animal, and was rotated into place at 3.4 sec post odor onset only on trials where animals exhibited suprathreshold speed at any point 0-3.4 sec following the onset of odor delivery. Rotation of spout into place took ~ 200 ms. The lick spout was rotated into place if suprathreshold running was exhibited regardless of the trial type during which running occurred (eg, spout was still rotated into place for suprathreshold shock and CS- trials, but no reward was delivered). This was to keep all trial types as similar as possible. If applicable, the lick spout was rotated back to home position at 8 sec. Animals were not punished for off-target licking or running, nor was subthreshold running punished for reward or CS- trials. The inter-trial interval between subsequent cues was chosen as a random sample from a uniform distribution between 17 and 23 seconds. A total of 8 vCA1 and 4 dCA1 animals were included in the data set.

2-photon imaging

Genetically encoded calcium imaging of GCaMP6f was used to assess the functional activity of individual neurons. Images were captured using an Ultima IV laser scanning microscope (Bruker Nano, Middleton, WI) equipped with resonant scanning mirrors and high-speed scan electronic controller, dual GaAsP PMTs (Hamamatsu

model 7422PA-40), and motorized z focus (100 nm step size). GCaMP signal was filtered through an ET-GFP (FITC/CY2) filter set. Laser signal was provided by a MaiTai DeepSee mode-locked Ti:Sapphire laser source (Spectra-Physics, Irvine, CA) providing > 150kW max output at 920 nm. Acquisition speed was 30Hz for 512 x 512 pixel images. Images were averaged both online and offline, yielding a final frame rate of 3.75Hz.

Prior to each conditioning session, the imaging field of view (FOV) was determined, and imaging was conducted at that FOV for the entire session. For animals with multiple FOVs across sessions, each FOV was separated by > 60 μm in the z-dimension (dorsal-ventral) to ensure no overlap of cells across different FOVs. To facilitate re-identification of a specific FOV across sessions, the top of the GRIN lens served as a reference z-plane. Optimal laser power was determined for each FOV based on GCaMP expression level and was kept constant across sessions for a specific FOV. For each trial, imaging began 8 sec prior to cue onset and was terminated 11 sec afterward (19 sec total).

Signal extraction and cross-session registration

Videos were motion corrected offline using non-rigid motion correction based on template matching (NoRMCorre or Suite2p (Pachitariu et al., 2018; Pnevmatikakis & Giovannucci, 2017)). Cell segmentation and calcium transient time series data were extracted using Constrained Non-negative Matrix Factorization for microEndoscopic data (CNMF-e), a semi-automated algorithm optimized for GRIN lens Ca^{2+} imaging to denoise, deconvolve and demix calcium imaging data (Zhou et al., 2018). Putative neurons were manually inspected for appropriate spatial properties and Ca^{2+} dynamics,

and were visually checked against the corresponding motion corrected video in ImageJ. Ca²⁺ transient events were extracted using the OASIS algorithm embedded within CNMFe (Friedrich et al., 2017). We used these inferred calcium events for all analyses, unless otherwise noted. Denoising (CNMFe) and deconvolution (OASIS) steps were applied identically to vCA1 and dCA1.

Registration of cells across sessions imaged at the same FOV used probabilistic modeling of similarities between cell pairs across sessions (CellReg, (Friedrich et al., 2017; Sheintuch et al., 2017)). Briefly, spatial footprint maps were generated for each session by projecting the spatial filter of each cell onto a single image. Spatial footprint images from sessions imaged at the same FOV were then aligned. The distribution of similarities between pairs of neighboring cells were subsequently modeled via centroid distance to obtain an estimation for their probability of being the same cell (P_{same}). Cells were then registered across sessions via a clustering procedure that utilizes the previously obtained probabilities, with a probability threshold of 0.8. The average P_{same} value for registered cells was 0.95. All putative matches were visually inspected. There was no difference across regions for the proportion of cells registered (mean \pm StDev: dCA1: 0.46 \pm 0.13; vCA1: 0.49 \pm 0.14; U test, $p = 0.4$).

Data analysis

For statistical analyses and figures, calcium event activity was separated into 1-second bins and average activity during each bin was used. When reporting specific epochs of task results, “odor period” constituted the final 1-second bin of odor delivery (1-sec to 2-sec post odor onset), while “trace period” constituted the final 1-second bin of the trace period prior to reward delivery (1-sec to 2-sec post odor offset), unless

otherwise noted. These time bins were chosen to ensure odor was being experienced throughout the entire odor bin and to minimize any residual odor effects during trace period analysis. All statistical analyses were two-sided. For all figures: * $p < 0.05$, ** $p < 0.01$, *** $p < 0.001$. See Table S1 for all statistical analysis details.

Population decoding

A linear decoder was used to discriminate activity patterns into two discrete categories (Bishop, 2006):

$$y(t) = \theta(W\vec{r}(t) + b)$$

where y is the predicted label of the population activity pattern \vec{r} recorded at time \vec{r} and takes two values corresponding to two classes of patterns to decode (for example, two odor identities), W is the vector of weights assigned to each cell, and b is a bias term constant. Decoding parameters were attained via a supervised learning protocol with labeled data and used a support-vector machine (SVM) with a linear kernel (python/scikit/linearSVC). Results are reported as the generalized performance of the decoder using cross-validation, a standard machine learning procedure to avoid data overfitting. When multiple categories were involved, e.g., more than two trial types, multiple linear decoders were trained on pairs of discrete categories combined using majority-based error-correction codes.

We defined the patterns of calcium activity by computing the mean event rates for each individual cell during one-second time bins. Pseudo-population recordings were generated by combining cell datas across multiple animals/FOVs. For decoding, one-half of trials were randomly selected from each class and pseudo-population activity from these trials was used to train the decoder, while the remaining held-out half was

used to evaluate the decoder's generalization performance. When comparing decoding accuracy between neural populations of different size, we trained our decoder on a random subsample of cells from the more numerous population equal to that of the smaller population. We repeated the operation 100 times and then combined the cross-validated decoding accuracies of all random choices together to get a single sample of decoding accuracies (i.e. single data point reflecting the mean of all 100 iterations). We repeated the procedure 10 times to perform statistical comparisons across groups and against chance performance. A two-sided Mann-Whitney U Test was used to compare decoding accuracies between groups, and Bonferroni correction used for multiple comparisons.

For decoding against baseline, we used population activity during the 1-second time bin that began three seconds prior to CS onset as baseline data. Cross-time-bin and cross-session decoding followed the same procedure as within-session decoding. In the case of cross-session decoding, only cells registered across the compared sessions were included.

In all decoding line plots (eg, **Figure 2.1g**), each data point represents the decoding accuracy for the 1-second time bin ending at that point. For example, a data point at 2 seconds post odor onset represents decoding accuracy using activity extracted from 1-2 seconds post odor onset.

For decoder weights analysis, we used the weight assigned to individual cells by the decoder after fitting the model to the data. Similar to previous findings we found a strong correlation between decoder weight and cell activity (Stefanini et al., 2020). To thus minimize the effect of activity, we regressed out the components explained by

activity. For this, for each time bin that we analyzed we linearly regressed mean total activity for each cell vs the decoder weight assigned for that cell. We used the residuals from this analysis for comparisons of decoder weights across sessions.

For decoding distant time bins in our cross-time-bin decoding analysis (**Figure 2.6 and 2.7i**), we took the average of all decoding runs for each cross-time-bin comparison that was separated by 3 or more bins. Further, we only included comparisons where both train and test data occurred at least 1 second after odor onset (that is, pre-trial data was excluded).

Multidimensional Scaling (MDS)

We performed 2-dimensional MDS scaling of event data using python/scikit/MDS. As with decoding, we combined all cells recorded from a particular region (e.g., vCA1) across all mice into one pseudo-population. For each trial type, 100 trials were randomly selected for analysis, and MDS was performed. The Euclidean distance was taken between each trial type, and this process was repeated 100 times. Bar charts of Euclidean distance show the mean \pm SD of all runs.

Pattern similarity

To compute pattern similarities, we computed mean event rates during each time bin. We then computed the mean cosine similarities (Pearson correlation) between every pair of patterns as:

$$s = \frac{1}{N} \sum_{i,j \neq i}^N \frac{\vec{r}_i \vec{r}_j}{|\vec{r}_i| |\vec{r}_j|}$$

where \vec{r}_i and \vec{r}_j are the patterns of population activities for trial/time bin i and j , and N is the total number of pairs of patterns counted once. (McKenzie et al., 2014).

Single-cell responsivity

Data used for heatmaps of calcium-traces or inferred events were not binned. For each cell, z-scores were computed over the entire dataset for a specific condition (e.g., CS+ trials). To identify cells whose activity was modulated during specific epochs (e.g., CS+ period, trace period, etc.), for each trial containing the specified epoch the average event magnitude during the 1s epoch was compared to the average event magnitude during a 1s baseline period immediately prior to cue onset for that trial. P-values were determined using a two-tailed Mann Whitney U test and the False Discovery Rate (FDR) was applied to correct for multiple comparisons. Cells with an adjusted p-value < 0.05 were classified as responsive. Fisher's exact test was used to compare whether the proportion of selective cells for a specific epoch (e.g., CS+ Early vs CS+ Late) significantly differed ($p < 0.05$).

To compare the persistence of CS+-trial-related activity in vCA1 vs dCA1 neurons, we first parsed CS+ trial data into odd or even trials and averaged activity for each cell across these trials. We then extracted cells whose peak activity during odd trials occurred between odor onset and US onset. Average activity for these cells during even trials was then collected +/- 4 seconds around the time point of odd-trial peak activity, normalized to the amplitude of odd-trial peak activity, and plotted (**S2d**).

Behavior-neural activity correlation

We determined whether activity of dCA1 or vCA1 neurons were correlated with licking, breathing, and running. We regressed the lick and breath rates across the session against calcium events. We also regressed the velocity against calcium events but only during 4-7.5 seconds after odor exposure to remove arduino-related artifacts in velocity recording when lick spout was rotated in or out of position (rotated in at 3.4 s; rotated out at 8 s). We fitted a linear regression model to predict lick, breathing, or running rates and used the explained variance (R^2) as a measure of goodness of fit to compare the results across animals and days. We divided each analyzed session in 10 time-contiguous blocks and computed the generalization performance of the model with 10-fold cross-validation over these blocks to avoid overfitting. Regression was performed with regular linear regression with Lasso, and verified that there are low correlations across behavior and calcium activity and lick and breathing results are not qualitatively different.

Decoding high- vs low-speed running

Neural activity and running speed during the ITI (5-10s post odor onset) were averaged in 1 sec time bins. For each of the five bins, the median running speed was assessed for each individual animal and trials with speeds above or below this value were separated (trials with no running were excluded). The number of trials included for each condition (ie, low or high-speed) was matched by subsampling from the condition with larger trial number. Linear decoding followed the same procedures as above. Statistical comparisons of accuracy vs theoretical chance or across hippocampus

regions used the average decoding accuracies obtained for individual time bins for each trial type (reward, shock, or CS- trial). Thus, in total 15 data points were included for statistical comparisons per region. (5 time bins x 3 trial types = 15 data points/region).

Aha analysis

We identified the first moment of distinguished licking behavior between CS+ and CS- trials by locating in all mice in the 2-odor paradigm an “aha” moment. This was calculated by averaging across every 4 trials the cumulative CS+ and CS- lick rates, taking the slope of the difference in cumulative licking between these bins, and checking if 1) the difference exceeded the previous bin’s slope ≥ 1 standard deviation of the difference line up to that bin, and 2) the slope increase exceeded 1/3 of the difference between the previous set of trials. The averaging and thresholding with an increased slope relative to previous trials limited detection of instances where a short sequence of successfully discriminated trials were followed by a return to incorrect lickings, which would not represent a true aha moment. For potential aha moments detected on the first day of learning, we set a threshold of a minimum of 80 licks so that only mice who demonstrated lick rates similar to or above the baseline we required during lick training could be considered to have learned. All aha moments detected by this method were cross-checked with examining the raw licking data to ensure accuracy. Aha moments across mice spanned the first two days of learning, with 62% of mice reaching an aha moment on the first day or learning, and all mice reaching an aha moment by the end of the second day.

For aha population decoding analysis, we used 30 trials before or after the aha moment. For mice where the aha moment was < 30 trials from the end of the first or

beginning of the second day of learning, trials from both days were included in order to reach the full 30 trials, and only cells registered across both sessions were included.

Active time bins analysis

For this analysis, time series data were binned into 0.25 sec time bins to provide greater resolution. Because the Pre session only contained 15 trials of each trial type, only the first 15 trials of each trial type were included for all sessions examined. For each trial (defined as 0 - 8 seconds post odor onset) and each time bin within that trial (32 time bins total) we examined whether an event was present. The data presented show the number of time bins where an event was detected for at least one trial. For example, a cell that fired during time bin 5, and only time bin 5, on every trial would produce a score of 1. A cell firing on time bin 5 and 10 on trial 1, bins 7 and 10 on trial 7, and no firing on all other trials would produce a score of 3. A maximum score of 32 indicates that each of the 32 individual time bins registered an event on at least one of the 15 trials. This analysis was repeated for each cell. To compare whether individual cells changed with learning, we only included cross-registered cells.

Effect size estimation

For Mann Whitney U tests and Wilcoxon tests versus chance, effect size was determined using:

$$r = |z|/\sqrt{N}$$

where N is the total sample size and

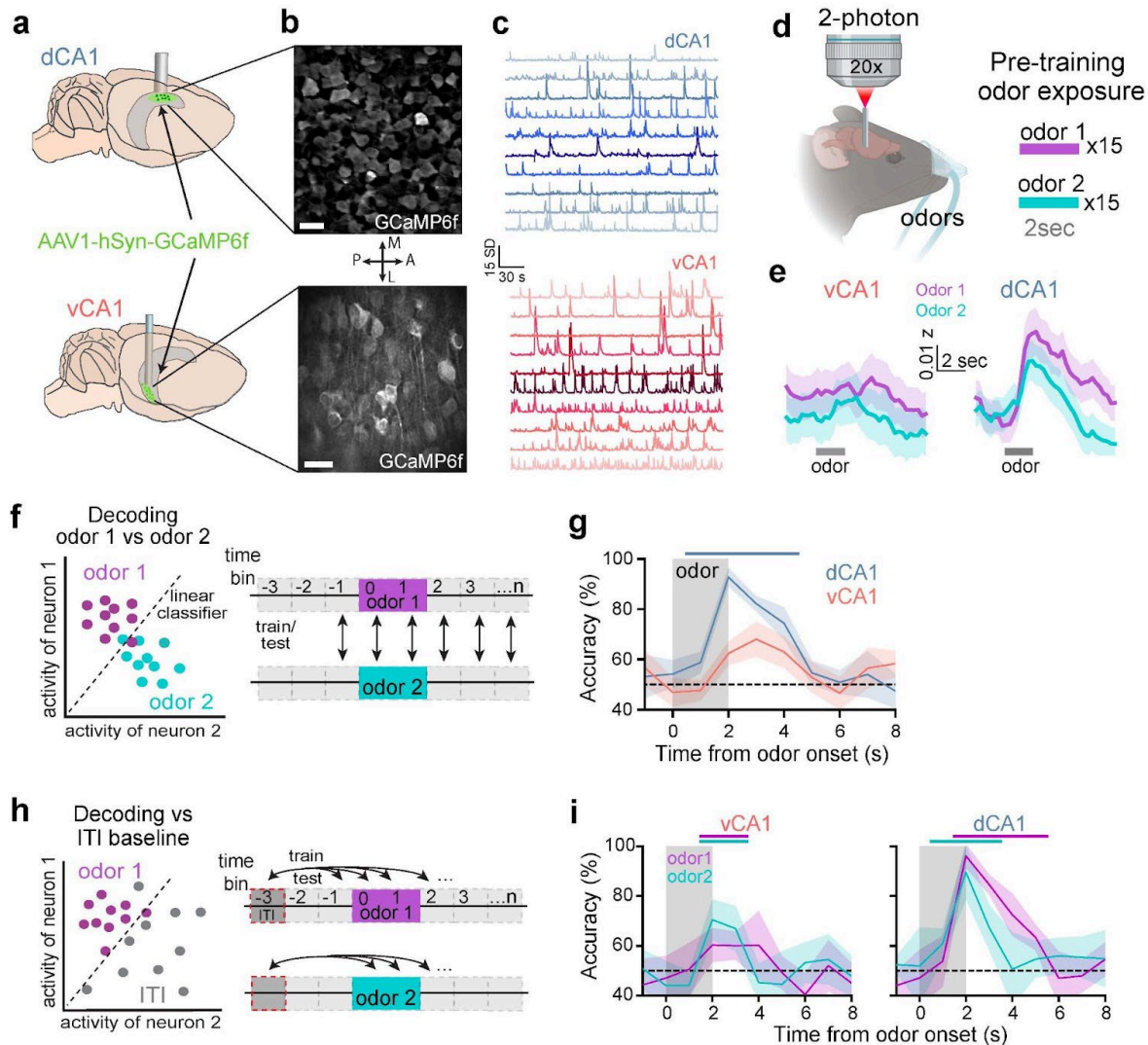
$$z = \frac{U - \frac{(n_1 n_2)}{2}}{\sqrt{\frac{n_1 n_2 (n_1 + n_2 + 1)}{12}}}$$

Where n_1 is the sample size of sample 1, n_2 the sample size of sample2, and U is the U test statistic obtained from the statistical test output. For t-test analysis, Cohen's d was used, defined as the difference between group means, divided by their pooled variance.

For Fisher's analysis, the odds ratio was obtained directly from the test output.

For one-way ANOVA, η^2 was obtained directly from the test output.

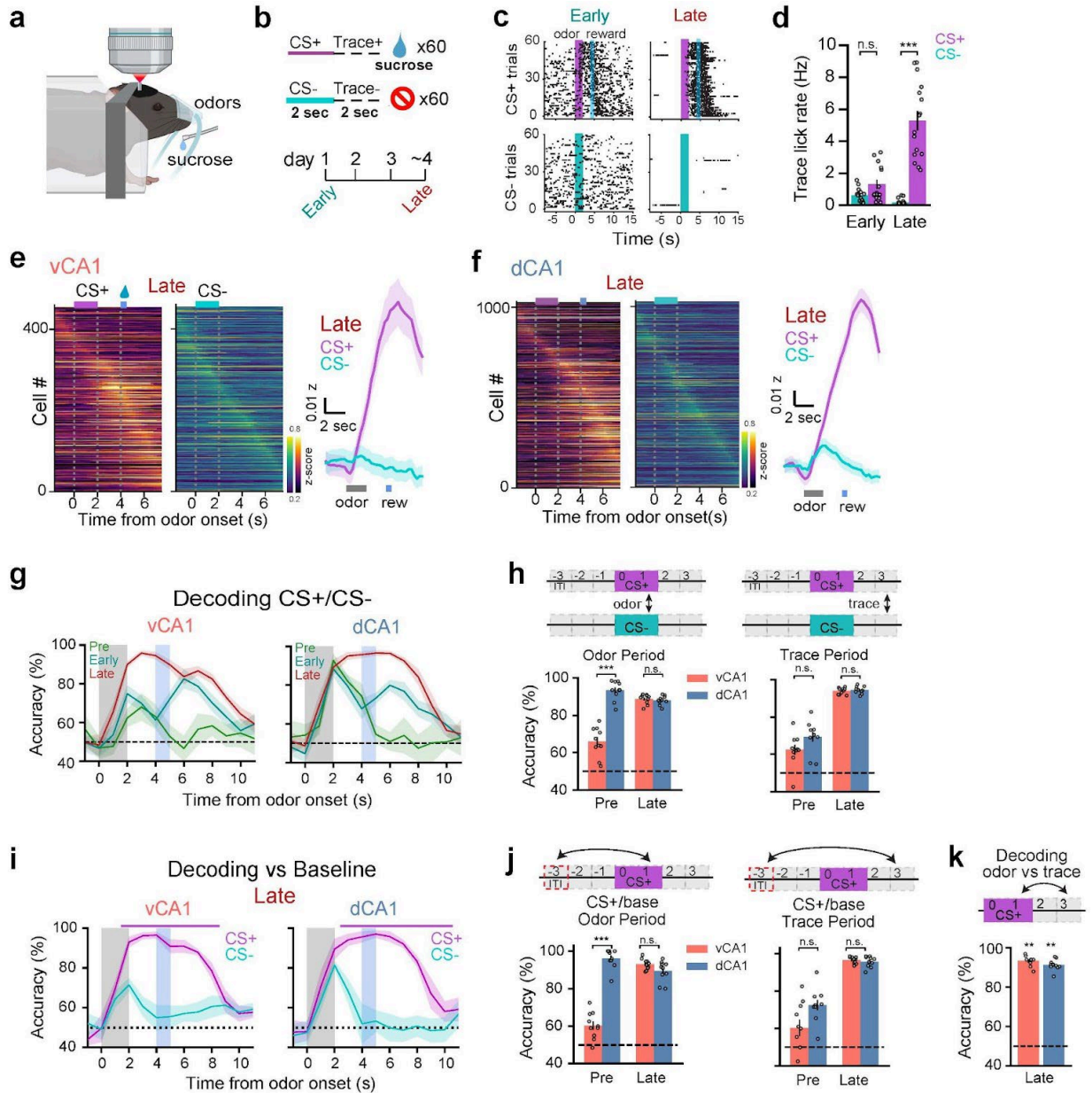
Figure 2.1 Prior to conditioning, odor stimuli are more strongly represented in dCA1 versus vCA1.



a. AAV virus expressing GCaMP6f was targeted to dCA1 or vCA1, and a GRIN lens was implanted above the injection site. **b and c.** Sample FOVs demonstrating (B) GCaMP expression and (C) time series data of denoised fluorescent traces. Scale bar in (B) = 25 μ m. **d.** Calcium signals were imaged while mice received 30 trials of 2 sec odor exposures (15 of each odor). **e.** Population mean (\pm SEM) of z-scored fluorescent signals occurring around the onset of odor1 (purple) or odor2 (cyan). Grey bar = odor delivery period. $n = 11$ vCA1 and 5 dCA1 mice. **f.** (left) Simplified schematic of decoding procedure illustrated using only 2 neurons. Each dot represents the single-trial “population” activity vector during odor 1 (purple) or odor 2 (cyan) delivery. (right) Linear classifiers were trained to distinguish population activity patterns occurring during odor 1 trials versus odor 2 trials for each 1-second time bin. **g.** Population-activity decoding accuracy for odor 1 versus odor 2 trials (\pm SD). Colored-coded bar above the graph denotes time bins where accuracy is significantly higher for dCA1 compared to vCA1 (p

< 0.01, Mann-Whitney U test; n= 454 cells for each region). **h.** (left) Simplified decoding schematic. Each dot represents the single-trial “population” activity vector during baseline (grey) or odor delivery (purple) periods. (right) Linear classifiers were trained to distinguish population activity patterns occurring during baseline from those occurring at time bin t . **i.** Same as **g** above, but decoding versus baseline for each time bin t . Color-coded bars above the graph denote time bins for each hpc region where decoding accuracy is significantly greater than chance ($p < 0.01$, Mann-Whitney U test; n= 454 cells for each region).

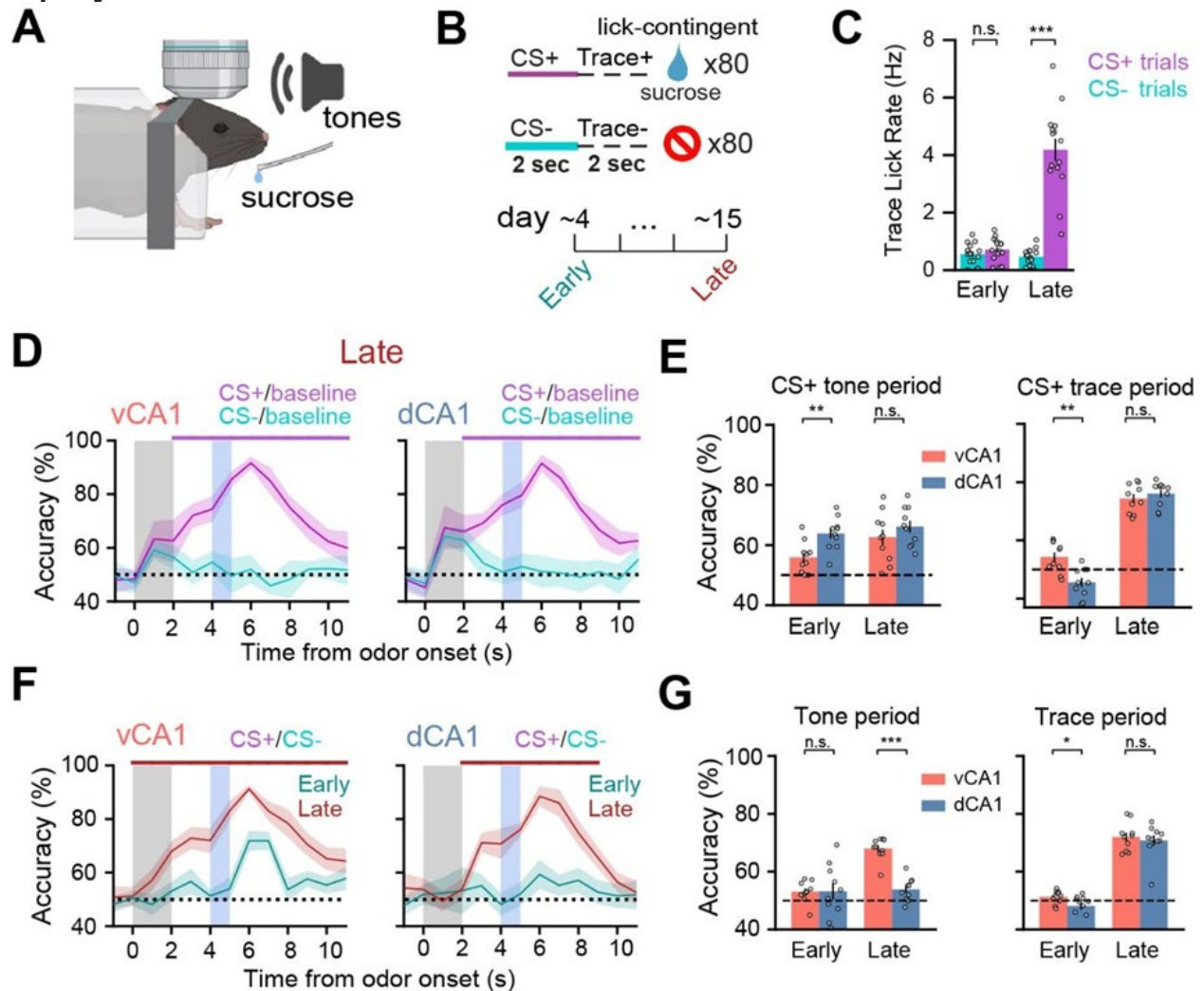
Figure 2.2 Discrimination training enhances task representations.



a-b. Task schematics. Calcium activity was imaged while headfixed mice were trained on an cue-outcome discrimination task over the course of ~4 days. Neurons were tracked over the duration of training. **c.** Lick rasters for an individual animal. Black tick = lick. During the first session of training (Early) licking is unstructured but becomes restricted to the time periods directly before and after reward delivery following CS+/CS- discrimination learning (Late). **d.** Mean lick rates during the 2-second pre-reward (trace) period for all animals (\pm SEM, Mann-Whitney U test; $n = 11$ vCA1, 5 dCA1). **e.** (left)

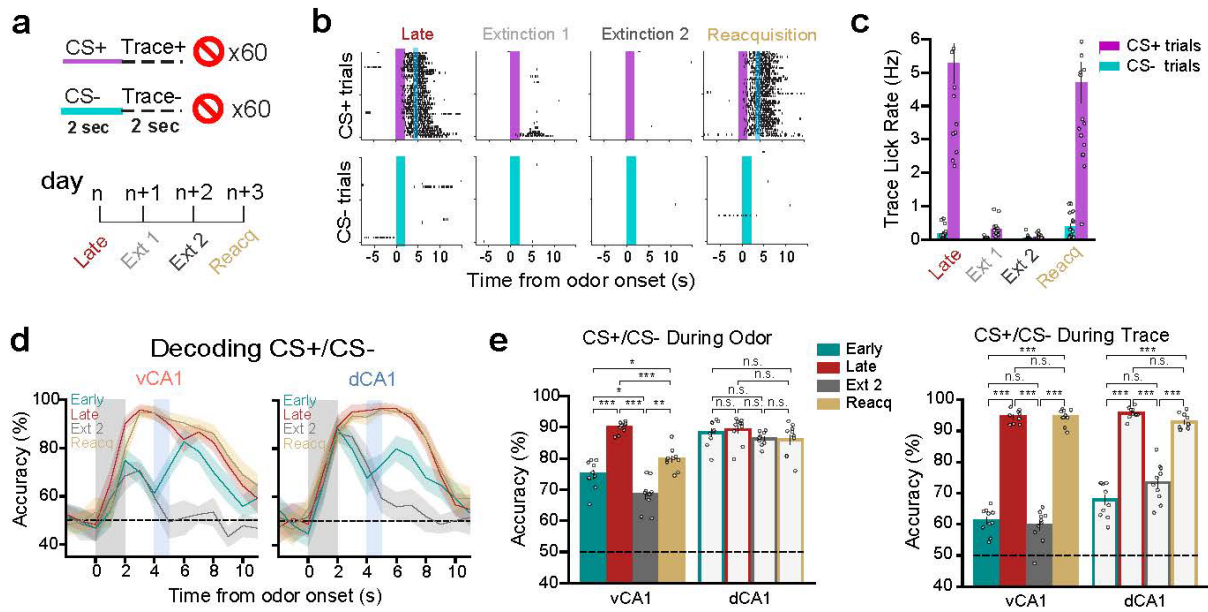
Mean z-scored fluorescent signals for all vCA1 cells during Late session, ordered by peak time bin. See **S3A** for Early session. (right) Population mean (\pm SEM). **f.** Same as in **e**, but for dCA1. **g.** Trial type decoding accuracies (\pm SD). Analyses used 454 cells. Odor delivery period = vertical grey bar. Sucrose delivery period (CS+ trials only) = vertical blue bar. Odor-period encoding selectively increases in vCA1, while trace period representations increase in both vCA1 and dCA1. **h.** Decoding accuracies for CS+ vs CS- during odor (left) or trace (right) periods (\pm SEM, Mann-Whitney U test). Individual data points represent individual decoding iterations. **i.** Decoding accuracies for each trial type vs ITI baseline (\pm SD). Color-coded bar above shows periods where the CS+ decoding accuracy vs baseline is significantly greater than that of CS- ($p < 0.01$, Mann-Whitney U test). Note the low decoding accuracy for CS- trials in vCA1 animals, suggesting trial type decoding in **g** is largely being driven by increased responsiveness to the behaviorally meaningful CS+ trials. **j.** same as **h**, but decoding CS+ vs ITI baseline. **k.** Decoding analysis shows population activity patterns during odor and trace periods could be well distinguished from one another in both areas. For all figures: * $p < 0.05$, ** $p < 0.01$, *** $p < 0.001$. See Table S1 for all statistical analysis details.

Figure 2.3 Learned odor representations are sensitive to extinction but can be rapidly reinstated.



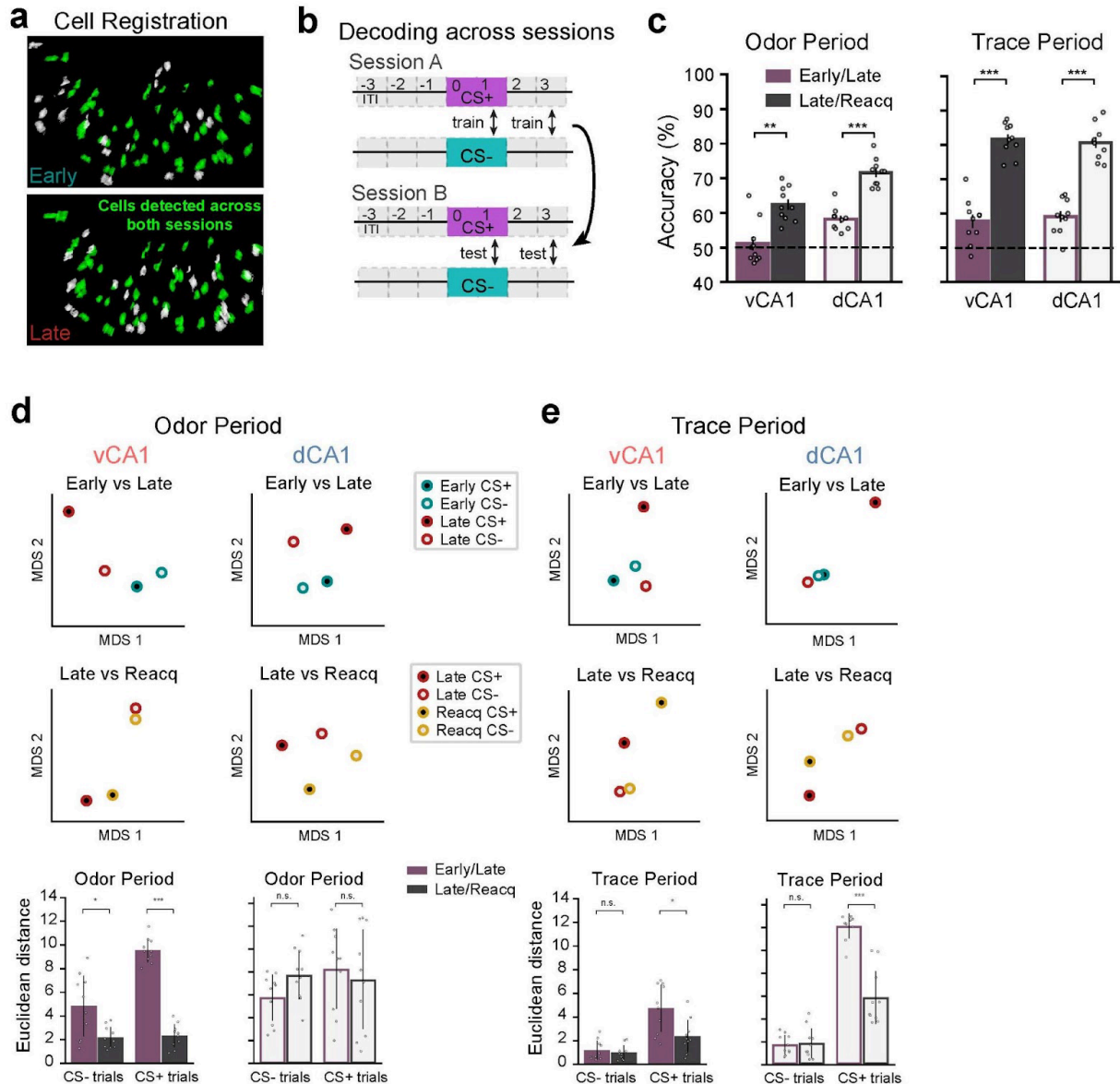
A-B. Task schematics. **C.** Mean lick rates during the 2-second pre-reward (trace) period for all animals (\pm SEM, Mann-Whitney U test). **D.** Decoding accuracies vs baseline (\pm SD). Color-coded bar above shows periods where the corresponding trial type accuracy is significantly greater than the opposing trial type ($p < 0.01$, Mann-Whitney U test). **E.** CS+ vs baseline decoding accuracies during odor (left) or trace (right) periods (\pm SEM, Mann-Whitney U test). **F and G.** Same as **D.** and **E.** but decoding trial type.

Figure 2.4 Learned odor representations are sensitive to extinction but can be rapidly reinstated.



a. Task schematic. Following acquisition of the cue-outcome discrimination task, mice were run through 2 days of extinction training where reward was omitted from all trials. The following day, animals underwent a Reacquisition session where the odor-sucrose contingency was restored. **b.** Lick rasters from an individual animal. Mice displayed a near absence of licking during the second day of extinction training and rapid resumption of anticipatory licking during the reacquisition session, illustrating an intact memory of the task structure. **c.** Mean trace-period lick rates (\pm SEM) across all animals ($n = 11$ vCA1, 5 dCA1). **d.** Trial-type decoding accuracies (\pm SD). Analyses used 454 cells for each region. Early and Late are as in **Figure 2.2g** and are shown for reference. **e.** Trial type decoding accuracies during odor (left) or trace (right) periods (\pm SEM, Mann-Whitney U test). Odor-period decoding accuracy tracked with odor-value in vCA1, but not dCA1. Trace-period accuracy tracked reward expectation in both hippocampal regions.

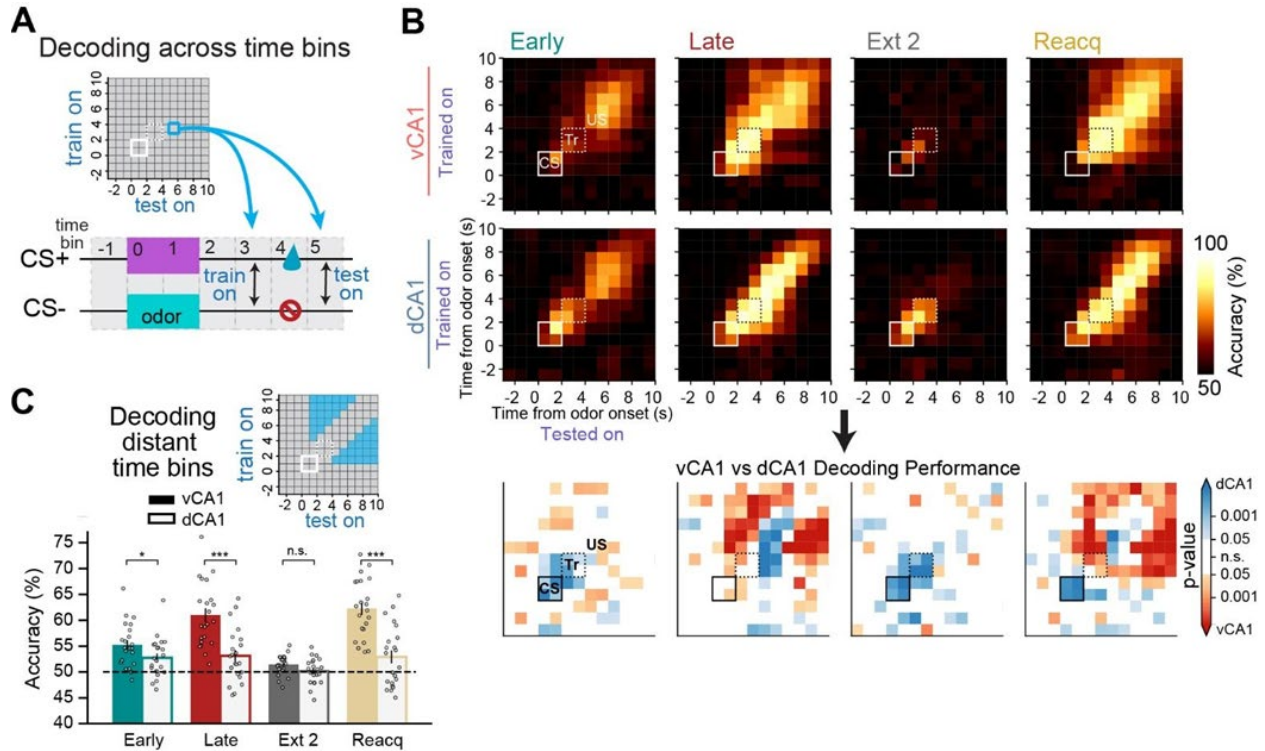
Figure 2.5 Task representations stabilize with learning



a. Example of cells from the same FOV registered across Early and Late sessions. **b.** Across-session trial-type decoding schematic. A linear decoder was trained to discriminate CS+ vs CS- population activity during one session, and classification accuracy was tested using activity patterns from a different session. **c.** Across-session decoding is significantly higher for odor and trace periods following learning (Late/Reacquisition), indicating a stabilization of task representations with learning. Despite high odor-period decoding accuracy in dCA1 for Early and Late sessions individually (**Figure 2.4e**), decoding across these sessions was comparatively low. Thus, while dCA1 activity distinguishes odors robustly at all training points, odor representations are transformed with learning. **d.** To analyze within-and across-session similarity between trial type population activity patterns, we projected the hyper-

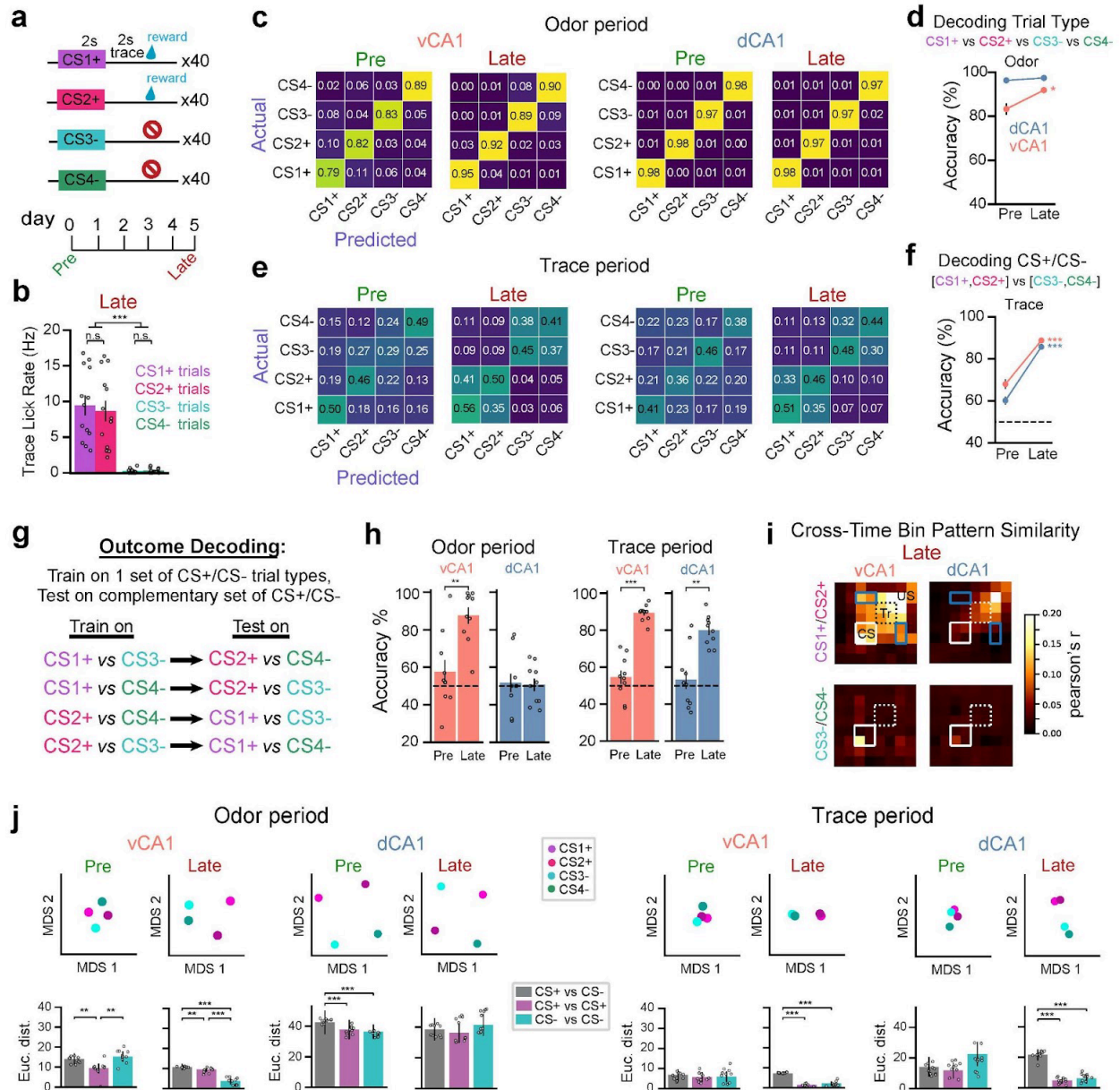
dimensional neural data onto 2-dimensional space via multidimensional scaling (MDS; see Methods). Here, the relationship between activity patterns is represented in geometrical space; the closer two points are in space, the more similar their activity patterns are. (top) 2-D dot plots showing an individual MDS run. (bottom) Average Euclidean distance (\pm SD) between specified points for 10 MDS runs. In vCA1, CS+ odor representations show considerable transformation with initial learning (Early/Late), but then largely stabilize (Late/Reacquisition), while CS- odor representations show comparatively little change with learning. dCA1 odor representations fluctuate across all sessions. **e**. Same as in **d**, but for trace-period representations. CS- trace representations show little change with learning, while CS+ representations show large initial changes with learning that then stabilize.

Figure 2.6 Long timescale representations in vCA1.



A. A linear classifier was trained to discriminate trial type using data from a single time bin, then tested for decoding accuracy on all other time bins. Each square is the decoding accuracy for the corresponding time bins on the x- and y-axes. The blue square shows the result corresponding to training the classifier on activity three seconds post odor onset and testing five seconds post odor onset. **B.** Decoding across time bins during different sessions of the 2-odor task. Closed white square denotes odor period (CS). Dashed square denotes trace period (Tr). Matrix at bottom reports p-values comparing the decoding accuracies of vCA1 and dCA1 (Mann-Whitney U test). **C.** Analysis of cross-time-bin decoding results for comparisons separated by at least 2 time bins (\pm SEM, Mann-Whitney U test). Inset: blue filling shows data bins that were included for analysis.

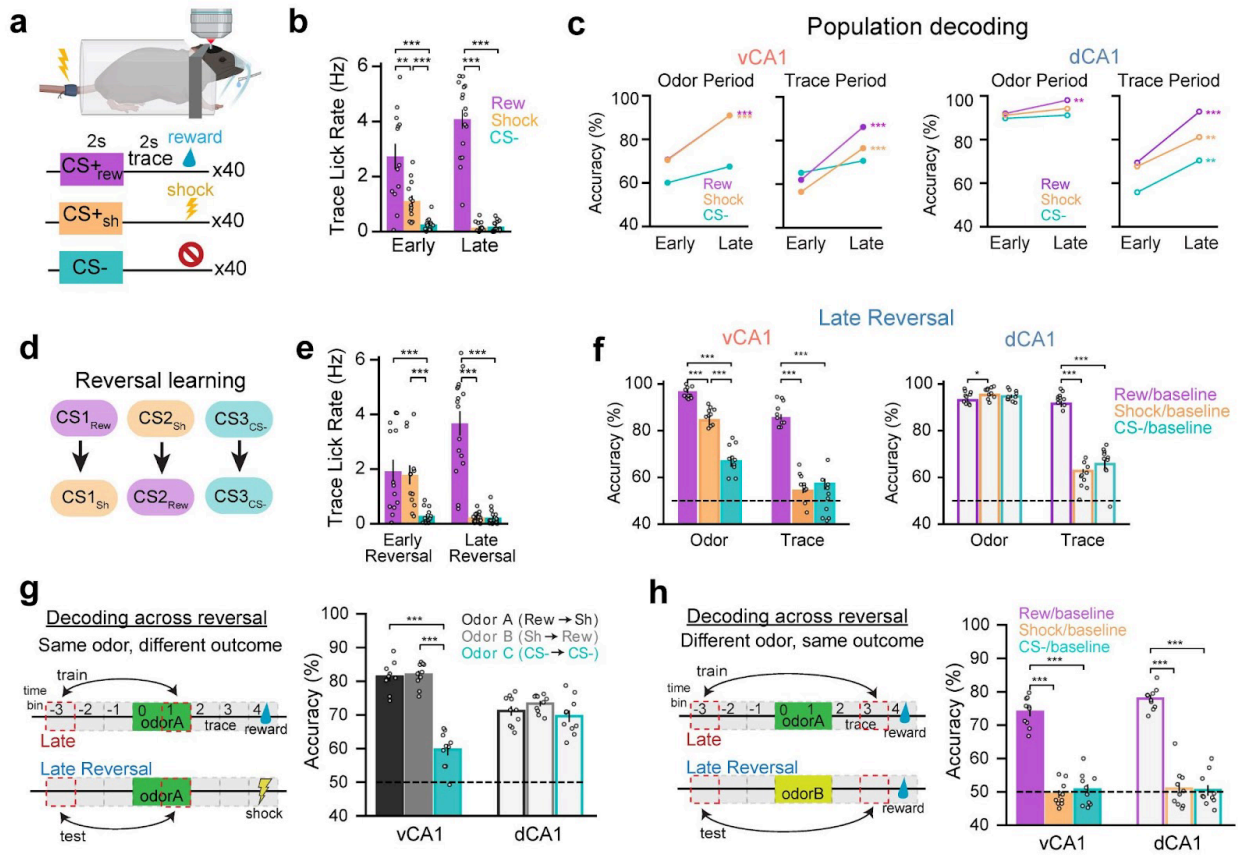
Figure 2.7 Individual odor representations dominate dCA1, while vCA1 incorporates information about future outcome. Both regions represent anticipated outcome during the trace period.



a. 4-odor task schematic. Each trial, animals received 1 of 4 odor cues, 2 of which predicted sucrose reward, while the remaining 2 odors were not associated with an outcome. **b.** Mean trace-period lick rates during the Late session (\pm SEM, Mann-Whitney U test). Data points represent individual animals ($n = 8$ vCA1, 5 dCA1). **c.** Confusion matrices for decoding trial type from population activity (analyses used 150 cells for each region). The y-axis denotes the actual trial type experienced and the x-axis indicates the proportion of trials that each trial type was classified as. The ascending diagonal represents the proportion of trials correctly classified, while other row entries

indicate the proportion of trials where the actual state was incorrectly identified as the corresponding trial type. **d.** Consistent with results from the 2-odor experiment, average trial-type classification accuracy during the odor period was unchanged with learning in dCA1, but significantly increased in vCA1. **e.** Same as in c, but decoding using trace-period activity patterns. Unlike the odor period, there is an increased incidence of parallel trial types (e.g., CS1+ and CS2+) being confused during trace, indicative of similar representations. **f.** CS+ trial types could be better discriminated from CS- trial types with learning in both vCA1 and dCA1. **g and h.** A linear classifier was trained to discriminate activity between reward-predictive and non-predictive trial types (e.g., CS1+ vs CS3-), then tested using data from the complementary trial types (CS2+ and CS4-). The mean for all combinations of trial-type pairs is presented in h (\pm SEM, Mann-Whitney U test), with individual data points reporting individual decoding iterations. Although individual odor representations in vCA1 are well discriminated in the Late session (as seen in d), future outcome can also be decoded with high accuracy during this time, suggesting vCA1 multiplexes information about odor identity and its associated outcome when presented with an odor cue. **i.** Pearson's correlation of neural activity patterns across CS+ (top) or CS- (bottom) trial types. Correlations were assessed both within (across the diagonal) and across time bins. White box shows time of odor presentation (CS); dashed box shows 2-second trace period (Tr). vCA1 displayed elevated pattern similarity between CS1+ and CS2+ trials that spanned across all task time bins. Blue boxes denote the data points that report similarity between odor-period and sucrose representations. **j.** Visualization of within-session pattern similarities via MDS. (top) example MDS run. (bottom) Average (\pm SEM, Mann-Whitney U test) of 10 runs. Following training, trace-period representations cluster into groups based on trial type.

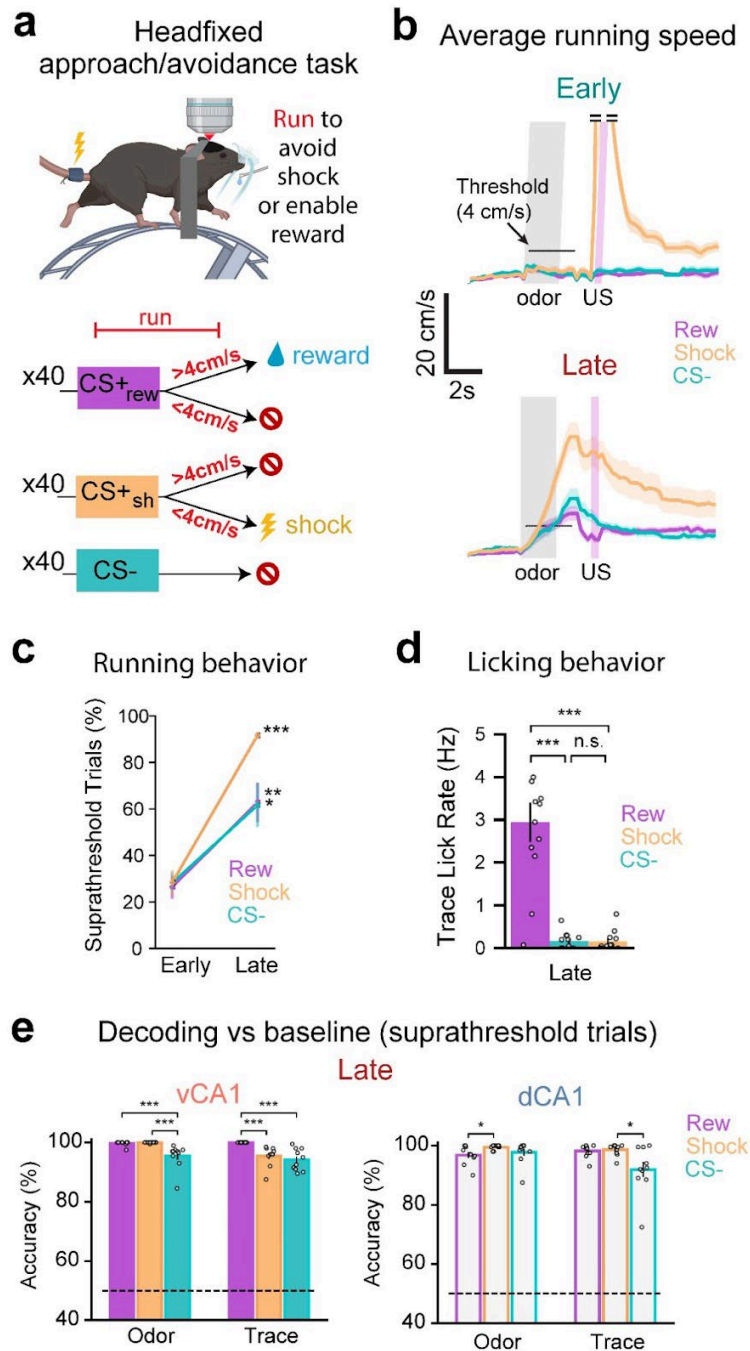
Figure 2.8 Aversive conditioning and reversal learning.



a. Task schematic. Three novel odors were used, each predicting either sucrose reward (CS+rew), inescapable tail shock (CS+sh), or nothing. **b.** Mean trace-period lick rates across all animals (\pm SEM, Mann-Whitney U test). **c.** Comparison of trial type decoding accuracy for Early and Late sessions. Analyses used 444 cells. See **S10d,e** for confusion matrices. Odor-period changes mirrored those of the 2-odor task (ie, increased decoding accuracy for odors with learned value; CS+rew and CS+shock). Interestingly, trace-period analysis showed decoding accuracy was lower for CS+sh trials compared to CS+rew. Statistics compare Early vs Late decoding accuracies (\pm SEM, Mann-Whitney U test) **d.** Reversal learning schematic. The identity of odors predicting sucrose and shock was swapped, while CS- odor remained the same. **e.** Mean trace lick rates across all animals (\pm SEM, Mann-Whitney U test;). Data points represent individual animals (n = 11 vCA1, 3 dCA1). **f.** Within-session decoding accuracies for each trial type vs baseline during odor (left) or trace (right) periods (\pm SEM, Mann-Whitney U test). Note the near absence of decoding accuracy above chance during the trace period for CS+sh trials. **g.** (left) Schematic showing cross-session odor vs baseline decoding for a specific odor paired with different outcomes. (right) Cross-session decoding accuracies indicate that an odor's representation is conserved even when the outcome associated with the odor changes (\pm SEM, Mann-Whitney U test). Analyses used 281 cells for each region. **h.** Same as in g, but decoding during outcome anticipation (trace period) for a specific outcome preceded by different

odors. Reward-anticipation-like signals are conserved across different predictive cues, while shock anticipatory coding, which is only weakly present in Late Reversal (f), are not.

Figure 2.9 Instrumental control of outcomes increases task-related representations in associative learning



a. To assess whether the behaviorally irrelevant nature of the inescapable shock contributed to the decoding accuracy differences observed for CS+sh and CS+rew (**Figure 2.8**), we implemented a new task, headfixed approach-avoidance. Mice running on a wheel could escape shock delivery or enable sucrose delivery if running velocity reached ≥ 4 cm/s during the odor and trace periods. **b.** Mean task running velocity

across all animals for each trial type (mean \pm SD). **c.** The percentage of trials with suprathreshold running significantly increased for all trial types from Early to Late sessions. **d.** Mean trace lick rates across all animals (\pm SEM, Mann-Whitney U test). Data points represent individual animals (n = 8 vCA1, 4 dCA1). **e.** With the shock outcome behaviorally relevant, CS+sh trials can now be decoded from baseline activity with high accuracy during the trace period (\pm SEM, Mann-Whitney U test). Analyses used 340 cells for each region. Subthreshold trials excluded.

References for Chapter 2

- Ahmed, M. S., Priestley, J. B., Castro, A., Stefanini, F., Solis Canales, A. S., Balough, E. M., Lavoie, E., Mazzucato, L., Fusi, S., & Losonczy, A. (2020). Hippocampal Network Reorganization Underlies the Formation of a Temporal Association Memory. *Neuron*, *107*(2), 283–291.e6.
- Albieri, G., Barnes, S. J., de Celis Alonso, B., Cheetham, C. E. J., Edwards, C. E., Lowe, A. S., Karunaratne, H., Dear, J. P., Lee, K. C., & Finnerty, G. T. (2015). Rapid Bidirectional Reorganization of Cortical Microcircuits. *Cerebral Cortex*, *25*(9), 3025–3035.
- Bangasser, D. A., Waxler, D. E., Santollo, J., & Shors, T. J. (2006). Trace conditioning and the hippocampus: the importance of contiguity. *The Journal of Neuroscience: The Official Journal of the Society for Neuroscience*, *26*(34), 8702–8706.
- Basu, J., & Siegelbaum, S. A. (2015). The Corticohippocampal Circuit, Synaptic Plasticity, and Memory. *Cold Spring Harbor Perspectives in Biology*, *7*(11).
<https://doi.org/10.1101/cshperspect.a021733>
- Bazargani, N., & Attwell, D. (2016). Astrocyte calcium signaling: the third wave. *Nature Neuroscience*, *19*(2), 182–189.
- Beyeler, A., Namburi, P., Glober, G. F., Simonnet, C., Calhoon, G. G., Conyers, G. F., Luck, R., Wildes, C. P., & Tye, K. M. (2016). Divergent Routing of Positive and Negative Information from the Amygdala during Memory Retrieval. *Neuron*, *90*(2), 348–361.

- Biane, J. S., Takashima, Y., Scanziani, M., Conner, J. M., & Tuszynski, M. H. (2019). Reorganization of Recurrent Layer 5 Corticospinal Networks Following Adult Motor Training. *The Journal of Neuroscience: The Official Journal of the Society for Neuroscience*, 39(24), 4684–4693.
- Bienkowski, M. S., Bowman, I., Song, M. Y., Gou, L., Ard, T., Cotter, K., Zhu, M., Benavidez, N. L., Yamashita, S., Abu-Jaber, J., Azam, S., Lo, D., Foster, N. N., Hintiryan, H., & Dong, H.-W. (2018). Integration of gene expression and brain-wide connectivity reveals the multiscale organization of mouse hippocampal networks. *Nature Neuroscience*, 21(11), 1628–1643.
- Bishop, C. M. (2006). *Pattern Recognition and Machine Learning*. Springer Verlag.
- Burton, B. G., Hok, V., Save, E., & Poucet, B. (2009). Lesion of the ventral and intermediate hippocampus abolishes anticipatory activity in the medial prefrontal cortex of the rat. *Behavioural Brain Research*, 199(2), 222–234.
- Cai, D. J., Aharoni, D., Shuman, T., Shobe, J., Biane, J., Song, W., Wei, B., Veshkini, M., La-Vu, M., Lou, J., Flores, S. E., Kim, I., Sano, Y., Zhou, M., Baumgaertel, K., Lavi, A., Kamata, M., Tuszynski, M., Mayford, M., ... Silva, A. J. (2016). A shared neural ensemble links distinct contextual memories encoded close in time. *Nature*, 534(7605), 115–118.
- Cenquizca, L. A., & Swanson, L. W. (2007). Spatial organization of direct hippocampal field CA1 axonal projections to the rest of the cerebral cortex. *Brain Research Reviews*, 56(1), 1–26.

- Chockanathan, U., & Padmanabhan, K. (2021). Divergence in Population Coding for Space between Dorsal and Ventral CA1. *eNeuro*, 8(5).
<https://doi.org/10.1523/ENEURO.0211-21.2021>
- Ciocchi, S., Passecker, J., Malagon-Vina, H., Mikus, N., & Klausberger, T. (2015). Brain computation. Selective information routing by ventral hippocampal CA1 projection neurons. *Science*, 348(6234), 560–563.
- Collin, S. H. P., Milivojevic, B., & Doeller, C. F. (2015). Memory hierarchies map onto the hippocampal long axis in humans. *Nature Neuroscience*, 18(11), 1562–1564.
- Danielson, N. B., Zaremba, J. D., Kaifosh, P., Bowler, J., Ladow, M., & Losonczy, A. (2016). Sublayer-Specific Coding Dynamics during Spatial Navigation and Learning in Hippocampal Area CA1. *Neuron*, 91(3), 652–665.
- Deuchars, J., & Thomson, A. M. (1996). CA1 pyramid-pyramid connections in rat hippocampus in vitro: dual intracellular recordings with biocytin filling. *Neuroscience*, 74(4), 1009–1018.
- Doron, A., Rubin, A., Benmelech-Chovav, A., Benaim, N., Carmi, T., Refaeli, R., Novick, N., Kreisel, T., Ziv, Y., & Goshen, I. (2022). Hippocampal astrocytes encode reward location. *Nature*, 609(7928), 772–778.
- Douglas, R. J., & Martin, K. A. C. (2007). Recurrent neuronal circuits in the neocortex. *Current Biology: CB*, 17(13), R496–R500.
- Dupret, D., O'Neill, J., Pleydell-Bouverie, B., & Csicsvari, J. (2010). The reorganization and reactivation of hippocampal maps predict spatial memory performance. *Nature Neuroscience*, 13(8), 995–1002.

- Duvelle, É., Grieves, R. M., Hok, V., Poucet, B., Arleo, A., Jeffery, K. J., & Save, E. (2019). Insensitivity of Place Cells to the Value of Spatial Goals in a Two-Choice Flexible Navigation Task. *The Journal of Neuroscience: The Official Journal of the Society for Neuroscience*, *39*(13), 2522–2541.
- Ebitz, R. B., & Hayden, B. Y. (2021). The population doctrine in cognitive neuroscience. *Neuron*, *109*(19), 3055–3068.
- Eichenbaum, H., Kuperstein, M., Fagan, A., & Nagode, J. (1987). Cue-sampling and goal-approach correlates of hippocampal unit activity in rats performing an odor-discrimination task. *The Journal of Neuroscience: The Official Journal of the Society for Neuroscience*, *7*(3), 716–732.
- Fanselow, M. S., & Dong, H.-W. (2010). Are the Dorsal and Ventral Hippocampus Functionally Distinct Structures? In *Neuron* (Vol. 65, Issue 1, pp. 7–19).
<https://doi.org/10.1016/j.neuron.2009.11.031>
- Felix-Ortiz, A. C., Beyeler, A., Seo, C., Leppla, C. A., Wildes, C. P., & Tye, K. M. (2013). BLA to vHPC inputs modulate anxiety-related behaviors. *Neuron*, *79*(4), 658–664.
- Friedrich, J., Zhou, P., & Paninski, L. (2017). Fast online deconvolution of calcium imaging data. *PLoS Computational Biology*, *13*(3), e1005423.
- Gauthier, J. L., & Tank, D. W. (2018). A Dedicated Population for Reward Coding in the Hippocampus. *Neuron*, *99*(1), 179–193.e7.
- Gava, G. P., McHugh, S. B., Lefèvre, L., Lopes-Dos-Santos, V., Trouche, S., El-Gaby, M., Schultz, S. R., & Dupret, D. (2021). Integrating new memories into the hippocampal network activity space. *Nature Neuroscience*, *24*(3), 326–330.

- Gergues, M. M., Han, K. J., Choi, H. S., Brown, B., Clausing, K. J., Turner, V. S., Vainchtein, I. D., Molofsky, A. V., & Kheirbek, M. A. (2020). Circuit and molecular architecture of a ventral hippocampal network. *Nature Neuroscience*, *23*(11), 1444–1452.
- Gonzalez, W. G., Zhang, H., Harutyunyan, A., & Lois, C. (2019). Persistence of neuronal representations through time and damage in the hippocampus. *Science*, *365*(6455), 821–825.
- Graham, J., D'Ambra, A. F., Jung, S. J., Teratani-Ota, Y., Vishwakarma, N., Venkatesh, R., Parigi, A., Antzoulatos, E. G., Fioravante, D., & Wiltgen, B. J. (2021). High-Frequency Stimulation of Ventral CA1 Neurons Reduces Amygdala Activity and Inhibits Fear. *Frontiers in Behavioral Neuroscience*, *15*, 595049.
- Grosmark, A. D., & Buzsáki, G. (2016). Diversity in neural firing dynamics supports both rigid and learned hippocampal sequences. *Science*, *351*(6280), 1440–1443.
- Gu, Z., & Yakel, J. L. (2011). Timing-dependent septal cholinergic induction of dynamic hippocampal synaptic plasticity. *Neuron*, *71*(1), 155–165.
- Hainmueller, T., & Bartos, M. (2018). Parallel emergence of stable and dynamic memory engrams in the hippocampus. In *Nature* (Vol. 558, Issue 7709, pp. 292–296). <https://doi.org/10.1038/s41586-018-0191-2>
- Harland, B., Contreras, M., & Fellous, J.-M. (2018). A Role for the Longitudinal Axis of the Hippocampus in Multiscale Representations of Large and Complex Spatial Environments and Mnemonic Hierarchies. In *The Hippocampus - Plasticity and Functions*. <https://doi.org/10.5772/intechopen.71165>

- Hok, V., Lenck-Santini, P.-P., Roux, S., Save, E., Muller, R. U., & Poucet, B. (2007). Goal-related activity in hippocampal place cells. *The Journal of Neuroscience: The Official Journal of the Society for Neuroscience*, 27(3), 472–482.
- Jimenez, J. C., Su, K., Goldberg, A. R., Luna, V. M., Biane, J. S., Ordek, G., Zhou, P., Ong, S. K., Wright, M. A., Zweifel, L., Paninski, L., Hen, R., & Kheirbek, M. A. (2018). Anxiety Cells in a Hippocampal-Hypothalamic Circuit. *Neuron*, 97(3), 670–683.e6.
- Jin, S.-W., & Lee, I. (2021). Differential encoding of place value between the dorsal and intermediate hippocampus. In *Current Biology* (Vol. 31, Issue 14, pp. 3053–3072.e5). <https://doi.org/10.1016/j.cub.2021.04.073>
- Jung, M. W., Wiener, S. I., & McNaughton, B. L. (1994). Comparison of spatial firing characteristics of units in dorsal and ventral hippocampus of the rat. In *The Journal of Neuroscience* (Vol. 14, Issue 12, pp. 7347–7356). <https://doi.org/10.1523/jneurosci.14-12-07347.1994>
- Kaufman, A. M., Geiller, T., & Losonczy, A. (2020). A Role for the Locus Coeruleus in Hippocampal CA1 Place Cell Reorganization during Spatial Reward Learning. *Neuron*, 105(6), 1018–1026.e4.
- Kay, K., & Frank, L. M. (2019). Three brain states in the hippocampus and cortex. In *Hippocampus* (Vol. 29, Issue 3, pp. 184–238). <https://doi.org/10.1002/hipo.22956>
- Kennedy, P. J., & Shapiro, M. L. (2009). Motivational states activate distinct hippocampal representations to guide goal-directed behaviors. *Proceedings of the National Academy of Sciences of the United States of America*, 106(26), 10805–10810.

- Kjelstrup, K. B., Solstad, T., Brun, V. H., Hafting, T., Leutgeb, S., Witter, M. P., Moser, E. I., & Moser, M.-B. (2008). Finite scale of spatial representation in the hippocampus. *Science*, *321*(5885), 140–143.
- Kjelstrup, K. G., Tuvnes, F. A., Steffenach, H.-A., Murison, R., Moser, E. I., & Moser, M.-B. (2002). Reduced fear expression after lesions of the ventral hippocampus. *Proceedings of the National Academy of Sciences of the United States of America*, *99*(16), 10825–10830.
- Knowles, W. D., & Schwartzkroin, P. A. (1981). Local circuit synaptic interactions in hippocampal brain slices. *The Journal of Neuroscience: The Official Journal of the Society for Neuroscience*, *1*(3), 318–322.
- Knudsen, E. B., & Wallis, J. D. (2021). Hippocampal neurons construct a map of an abstract value space. *Cell*, *184*(18), 4640–4650.e10.
- Komorowski, R. W., Garcia, C. G., Wilson, A., Hattori, S., Howard, M. W., & Eichenbaum, H. (2013). Ventral hippocampal neurons are shaped by experience to represent behaviorally relevant contexts. *The Journal of Neuroscience: The Official Journal of the Society for Neuroscience*, *33*(18), 8079–8087.
- Komorowski, R. W., Manns, J. R., & Eichenbaum, H. (2009). Robust conjunctive item-place coding by hippocampal neurons parallels learning what happens where. *The Journal of Neuroscience: The Official Journal of the Society for Neuroscience*, *29*(31), 9918–9929.
- LeGates, T. A., Kvarita, M. D., Tooley, J. R., Francis, T. C., Lobo, M. K., Creed, M. C., & Thompson, S. M. (2018). Reward behaviour is regulated by the strength of hippocampus-nucleus accumbens synapses. *Nature*, *564*(7735), 258–262.

- Liberti, W. A., 3rd, Schmid, T. A., Forli, A., Snyder, M., & Yartsev, M. M. (2022). A stable hippocampal code in freely flying bats. *Nature*, *604*(7904), 98–103.
- Lien, A. D., & Scanziani, M. (2013). Tuned thalamic excitation is amplified by visual cortical circuits. *Nature Neuroscience*, *16*(9), 1315–1323.
- Li, Y., Xu, J., Liu, Y., Zhu, J., Liu, N., Zeng, W., Huang, N., Rasch, M. J., Jiang, H., Gu, X., Li, X., Luo, M., Li, C., Teng, J., Chen, J., Zeng, S., Lin, L., & Zhang, X. (2017). A distinct entorhinal cortex to hippocampal CA1 direct circuit for olfactory associative learning. *Nature Neuroscience*, *20*(4), 559–570.
- MacDonald, C. J., Carrow, S., Place, R., & Eichenbaum, H. (2013). Distinct hippocampal time cell sequences represent odor memories in immobilized rats. *The Journal of Neuroscience: The Official Journal of the Society for Neuroscience*, *33*(36), 14607–14616.
- Mankin, E. A., Sparks, F. T., Slayyeh, B., Sutherland, R. J., Leutgeb, S., & Leutgeb, J. K. (2012). Neuronal code for extended time in the hippocampus. *Proceedings of the National Academy of Sciences of the United States of America*, *109*(47), 19462–19467.
- Markus, E. J., Qin, Y. L., Leonard, B., Skaggs, W. E., McNaughton, B. L., & Barnes, C. A. (1995). Interactions between location and task affect the spatial and directional firing of hippocampal neurons. *The Journal of Neuroscience: The Official Journal of the Society for Neuroscience*, *15*(11), 7079–7094.
- McEchron, M. D., Bouwmeester, H., Tseng, W., Weiss, C., & Disterhoft, J. F. (1998). Hippocampectomy disrupts auditory trace fear conditioning and contextual fear conditioning in the rat. *Hippocampus*, *8*(6), 638–646.

- McKenzie, S., Frank, A. J., Kinsky, N. R., Porter, B., Rivière, P. D., & Eichenbaum, H. (2014). Hippocampal representation of related and opposing memories develop within distinct, hierarchically organized neural schemas. *Neuron*, *83*(1), 202–215.
- McNamara, C. G., Tejero-Cantero, Á., Trouche, S., Campo-Urriza, N., & Dupret, D. (2014). Dopaminergic neurons promote hippocampal reactivation and spatial memory persistence. *Nature Neuroscience*, *17*(12), 1658–1660.
- Mount, R. A., Sridhar, S., Hansen, K. R., Mohammed, A. I., Abdulkerim, M., Kessel, R., Nazer, B., Gritton, H. J., & Han, X. (2021). Distinct neuronal populations contribute to trace conditioning and extinction learning in the hippocampal CA1. *eLife*, *10*.
<https://doi.org/10.7554/eLife.56491>
- Musall, S., Kaufman, M. T., Juavinett, A. L., Gluf, S., & Churchland, A. K. (2019). Single-trial neural dynamics are dominated by richly varied movements. *Nature Neuroscience*, *22*(10), 1677–1686.
- Namboodiri, V. M. K., Otis, J. M., van Heeswijk, K., Voets, E. S., Alghorazi, R. A., Rodriguez-Romaguera, J., Mihalas, S., & Stuber, G. D. (2019). Single-cell activity tracking reveals that orbitofrontal neurons acquire and maintain a long-term memory to guide behavioral adaptation. *Nature Neuroscience*, *22*(7), 1110–1121.
- Navas-Olive, A., Valero, M., Jurado-Parras, T., de Salas-Quiroga, A., Averkin, R. G., Gambino, G., Cid, E., & de la Prida, L. M. (2020). Multimodal determinants of phase-locked dynamics across deep-superficial hippocampal sublayers during theta oscillations. *Nature Communications*, *11*(1), 2217.

- Nieh, E. H., Schottdorf, M., Freeman, N. W., Low, R. J., Lewallen, S., Koay, S. A., Pinto, L., Gauthier, J. L., Brody, C. D., & Tank, D. W. (2021). Geometry of abstract learned knowledge in the hippocampus. *Nature*, *595*(7865), 80–84.
- O'Keefe, J., & Dostrovsky, J. (1971). The hippocampus as a spatial map. Preliminary evidence from unit activity in the freely-moving rat. *Brain Research*, *34*(1), 171–175.
- Otis, J. M., Namboodiri, V. M. K., Matan, A. M., Voets, E. S., Mohorn, E. P., Kosyk, O., McHenry, J. A., Robinson, J. E., Resendez, S. L., Rossi, M. A., & Stuber, G. D. (2017). Prefrontal cortex output circuits guide reward seeking through divergent cue encoding. *Nature*, *543*(7643), 103–107.
- Pachitariu, M., Stringer, C., & Harris, K. D. (2018). Robustness of Spike Deconvolution for Neuronal Calcium Imaging. *The Journal of Neuroscience: The Official Journal of the Society for Neuroscience*, *38*(37), 7976–7985.
- Palacios-Filardo, J., & Mellor, J. R. (2019). Neuromodulation of hippocampal long-term synaptic plasticity. *Current Opinion in Neurobiology*, *54*, 37–43.
- Pastalkova, E., Itskov, V., Amarasingham, A., & Buzsáki, G. (2008). Internally generated cell assembly sequences in the rat hippocampus. *Science*, *321*(5894), 1322–1327.
- Paxinos, G., & Keith B. J. Franklin, M. A. (2019). *Paxinos and Franklin's the Mouse Brain in Stereotaxic Coordinates*. Academic Press.
- Petter, E. A., Gershman, S. J., & Meck, W. H. (2018). Integrating Models of Interval Timing and Reinforcement Learning. *Trends in Cognitive Sciences*, *22*(10), 911–922.

- Pnevmatikakis, E. A., & Giovannucci, A. (2017). NoRMCorre: An online algorithm for piecewise rigid motion correction of calcium imaging data. *Journal of Neuroscience Methods*, 291, 83–94.
- Poppenk, J., Evensmoen, H. R., Moscovitch, M., & Nadel, L. (2013). Long-axis specialization of the human hippocampus. *Trends in Cognitive Sciences*, 17(5), 230–240.
- Radvansky, B. A., Oh, J. Y., Climer, J. R., & Dombeck, D. A. (2021). Behavior determines the hippocampal spatial mapping of a multisensory environment. *Cell Reports*, 36(5), 109444.
- Ramanathan, K. R., Ressler, R. L., Jin, J., & Maren, S. (2018). Nucleus Reuniens Is Required for Encoding and Retrieving Precise, Hippocampal-Dependent Contextual Fear Memories in Rats. *The Journal of Neuroscience: The Official Journal of the Society for Neuroscience*, 38(46), 9925–9933.
- Royer, S., Sirota, A., Patel, J., & Buzsáki, G. (2010). Distinct representations and theta dynamics in dorsal and ventral hippocampus. *The Journal of Neuroscience: The Official Journal of the Society for Neuroscience*, 30(5), 1777–1787.
- Sato, M., Mizuta, K., Islam, T., Kawano, M., Takekawa, T., Gomez-Dominguez, D., Kim, K., Yamakawa, H., Ohkura, M., Fukai, T., Nakai, J., & Hayashi, Y. (n.d.). *Dynamic embedding of salience coding in hippocampal spatial maps*.
<https://doi.org/10.1101/266767>
- Sheintuch, L., Rubin, A., Brande-Eilat, N., Geva, N., Sadeh, N., Pinchasof, O., & Ziv, Y. (2017). Tracking the Same Neurons across Multiple Days in Ca Imaging Data. *Cell Reports*, 21(4), 1102–1115.

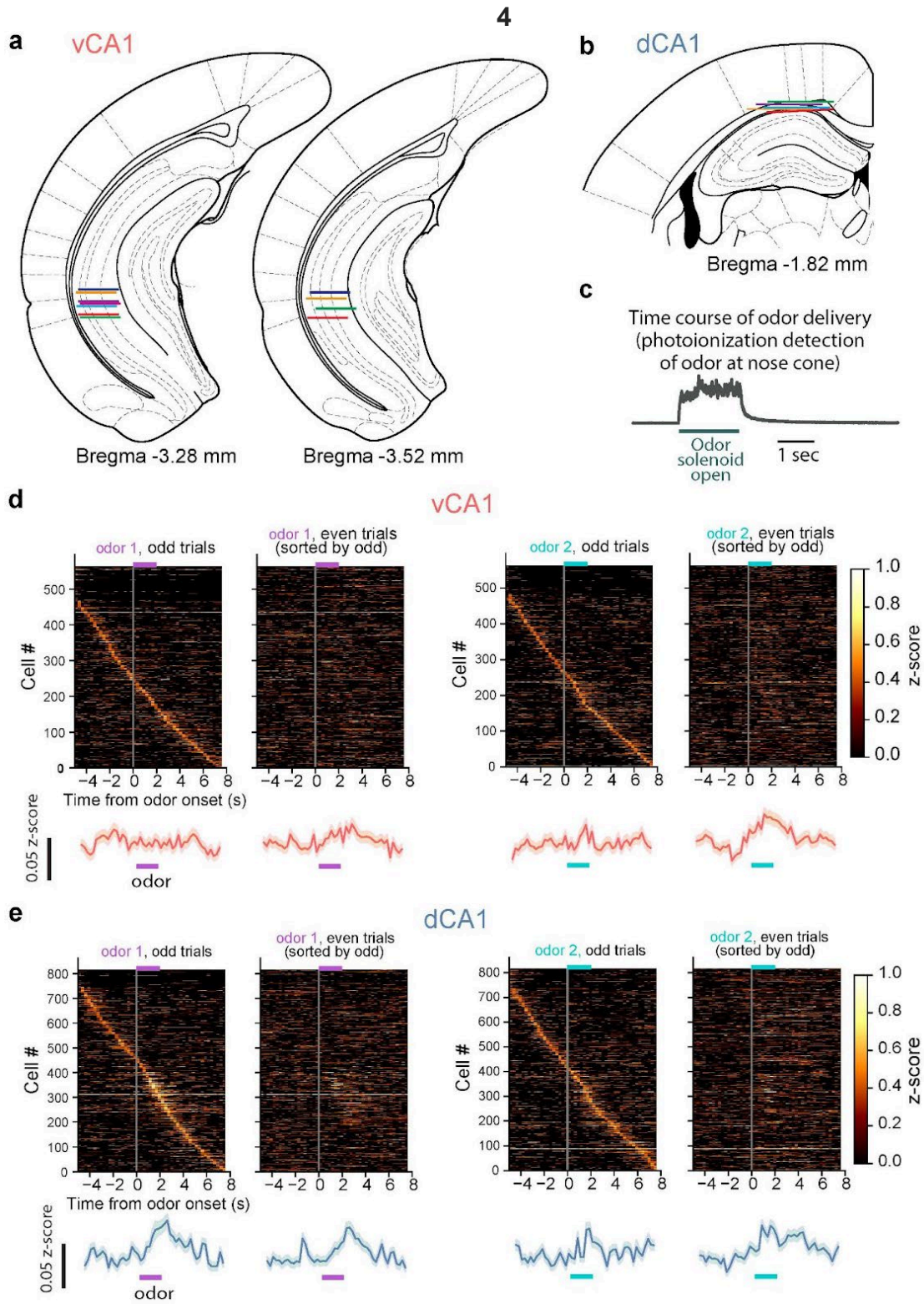
- Shohamy, D., & Wagner, A. D. (2008). Integrating memories in the human brain: hippocampal-midbrain encoding of overlapping events. *Neuron*, *60*(2), 378–389.
- Shpokayte, M., McKissick, O., Guan, X., Yuan, B., Rahsepar, B., Fernandez, F. R., Ruesch, E., Grella, S. L., White, J. A., Liu, X. S., & Ramirez, S. (2022). Hippocampal cells segregate positive and negative engrams. *Communications Biology*, *5*(1), 1009.
- Soltész, I., & Losonczy, A. (2018). CA1 pyramidal cell diversity enabling parallel information processing in the hippocampus. *Nature Neuroscience*, *21*(4), 484–493.
- Sosa, M., & Giocomo, L. M. (2021). Navigating for reward. *Nature Reviews. Neuroscience*, *22*(8), 472–487.
- Sosa, M., Joo, H. R., & Frank, L. M. (2020). Dorsal and Ventral Hippocampal Sharp-Wave Ripples Activate Distinct Nucleus Accumbens Networks. *Neuron*, *105*(4), 725–741.e8.
- Stachenfeld, K. L., Botvinick, M. M., & Gershman, S. J. (2017). The hippocampus as a predictive map. *Nature Neuroscience*, *20*(11), 1643–1653.
- Staresina, B. P., & Davachi, L. (2009). Mind the gap: binding experiences across space and time in the human hippocampus. *Neuron*, *63*(2), 267–276.
- Stefanini, F., Kushnir, L., Jimenez, J. C., Jennings, J. H., Woods, N. I., Stuber, G. D., Kheirbek, M. A., Hen, R., & Fusi, S. (2020). A Distributed Neural Code in the Dentate Gyrus and in CA1. *Neuron*, *107*(4), 703–716.e4.
- Strange, B. A., Witter, M. P., Lein, E. S., & Moser, E. I. (2014). Functional organization of the hippocampal longitudinal axis. *Nature Reviews. Neuroscience*, *15*(10), 655–669.

- Stringer, C., Pachitariu, M., Steinmetz, N., Reddy, C. B., Carandini, M., & Harris, K. D. (2019). Spontaneous behaviors drive multidimensional, brainwide activity. *Science*, *364*(6437), 255.
- Tannenholz, L., Jimenez, J. C., & Kheirbek, M. A. (2014). Local and regional heterogeneity underlying hippocampal modulation of cognition and mood. In *Frontiers in Behavioral Neuroscience* (Vol. 8).
<https://doi.org/10.3389/fnbeh.2014.00147>
- Taxidis, J., Pnevmatikakis, E. A., Dorian, C. C., Mylavarapu, A. L., Arora, J. S., Samadian, K. D., Hoffberg, E. A., & Golshani, P. (2020). Differential Emergence and Stability of Sensory and Temporal Representations in Context-Specific Hippocampal Sequences. *Neuron*, *108*(5), 984–998.e9.
- Teixeira, C. M., Rosen, Z. B., Suri, D., Sun, Q., Hersh, M., Sargin, D., Dincheva, I., Morgan, A. A., Spivack, S., Krok, A. C., Hirschfeld-Stoler, T., Lambe, E. K., Siegelbaum, S. A., & Ansorge, M. S. (2018). Hippocampal 5-HT Input Regulates Memory Formation and Schaffer Collateral Excitation. *Neuron*, *98*(5), 992–1004.e4.
- Trouche, S., Koren, V., Doig, N. M., Ellender, T. J., El-Gaby, M., Lopes-Dos-Santos, V., Reeve, H. M., Perestenko, P. V., Garas, F. N., Magill, P. J., Sharott, A., & Dupret, D. (2019). A Hippocampus-Accumbens Tripartite Neuronal Motif Guides Appetitive Memory in Space. *Cell*, *176*(6), 1393–1406.e16.
- Turi, G. F., Li, W.-K., Chavlis, S., Pandi, I., O'Hare, J., Priestley, J. B., Grosmark, A. D., Liao, Z., Ladow, M., Zhang, J. F., Zemelman, B. V., Poirazi, P., & Losonczy, A. (2019). Vasoactive Intestinal Polypeptide-Expressing Interneurons in the

- Hippocampus Support Goal-Oriented Spatial Learning. *Neuron*, 101(6), 1150–1165.e8.
- Wikenheiser, A. M., Marrero-Garcia, Y., & Schoenbaum, G. (2017). Suppression of Ventral Hippocampal Output Impairs Integrated Orbitofrontal Encoding of Task Structure. *Neuron*, 95(5), 1197–1207.e3.
- Wikenheiser, A. M., & Schoenbaum, G. (2016). Over the river, through the woods: cognitive maps in the hippocampus and orbitofrontal cortex. *Nature Reviews Neuroscience*, 17(8), 513–523.
- Wood, E. R., Dudchenko, P. A., Robitsek, R. J., & Eichenbaum, H. (2000). Hippocampal neurons encode information about different types of memory episodes occurring in the same location. *Neuron*, 27(3), 623–633.
- Woods, N. I., Stefanini, F., Apodaca-Montano, D. L., Tan, I. M. C., Biane, J. S., & Kheirbek, M. A. (2020). The Dentate Gyrus Classifies Cortical Representations of Learned Stimuli. *Neuron*, 107(1), 173–184.e6.
- Xia, F., & Kheirbek, M. A. (2020). Circuit-Based Biomarkers for Mood and Anxiety Disorders. In *Trends in Neurosciences* (Vol. 43, Issue 11, pp. 902–915). <https://doi.org/10.1016/j.tins.2020.08.004>
- Xu, C., Krabbe, S., Gründemann, J., Botta, P., Fadok, J. P., Osakada, F., Saur, D., Grewe, B. F., Schnitzer, M. J., Callaway, E. M., & Lüthi, A. (2016). Distinct Hippocampal Pathways Mediate Dissociable Roles of Context in Memory Retrieval. *Cell*, 167(4), 961–972.e16.

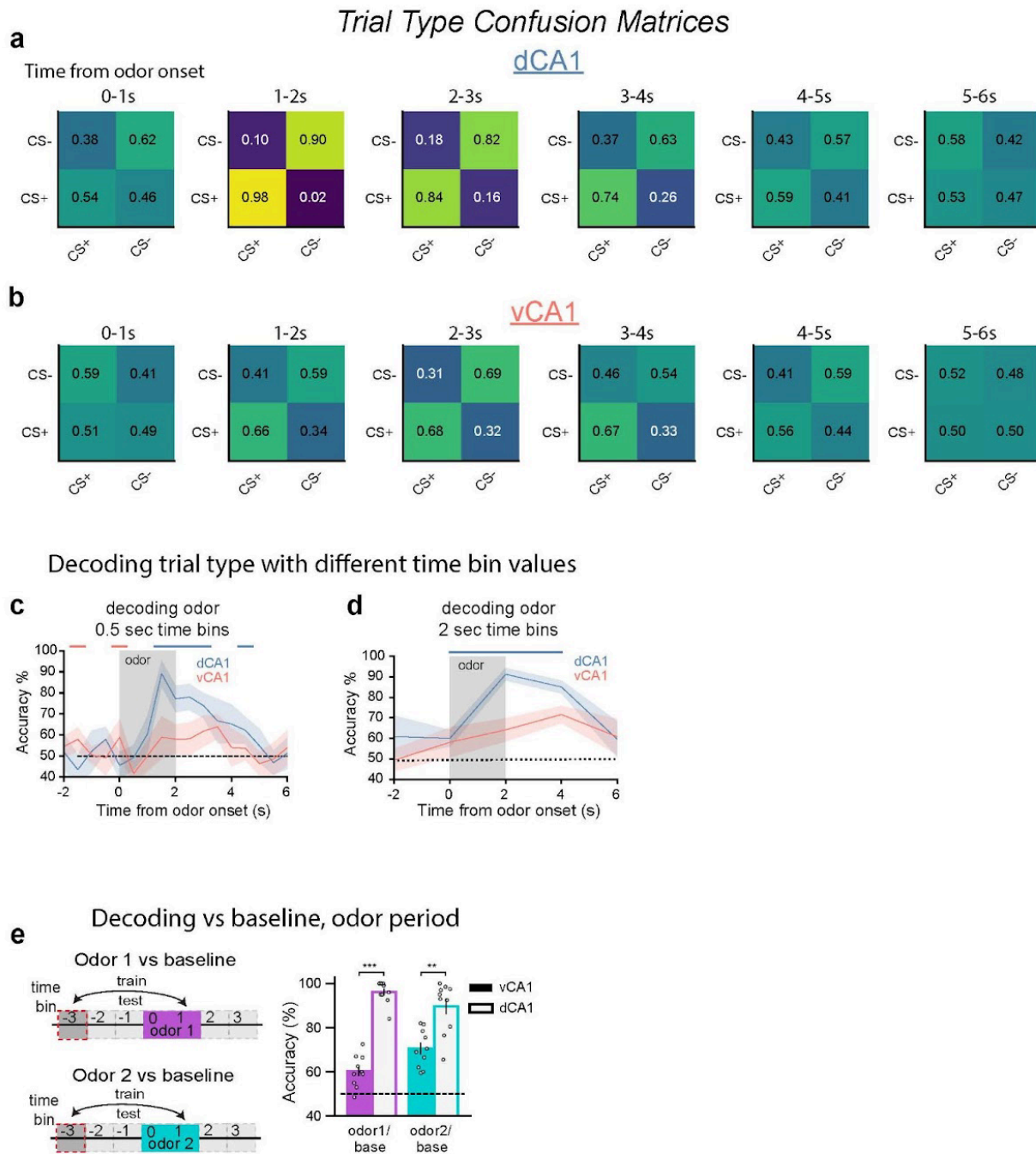
- Xu, H., BaracsKay, P., O'Neill, J., & Csicsvari, J. (2019). Assembly Responses of Hippocampal CA1 Place Cells Predict Learned Behavior in Goal-Directed Spatial Tasks on the Radial Eight-Arm Maze. *Neuron*, *101*(1), 119–132.e4.
- Yang, S., Yang, S., Moreira, T., Hoffman, G., Carlson, G. C., Bender, K. J., Alger, B. E., & Tang, C.-M. (2014). Interlamellar CA1 network in the hippocampus. *Proceedings of the National Academy of Sciences of the United States of America*, *111*(35), 12919–12924.
- Yu, J. Y., Liu, D. F., Loback, A., Grossrubatscher, I., & Frank, L. M. (2018). Specific hippocampal representations are linked to generalized cortical representations in memory. In *Nature Communications* (Vol. 9, Issue 1).
<https://doi.org/10.1038/s41467-018-04498-w>
- Zhang, L., Chen, X., Sindreu, C., Lu, S., Storm, D. R., Zweifel, L. S., & Xia, Z. (2019). Dynamics of a hippocampal neuronal ensemble encoding trace fear memory revealed by in vivo Ca²⁺ imaging. *PLoS One*, *14*(7), e0219152.
- Zhou, P., Resendez, S. L., Rodriguez-Romaguera, J., Jimenez, J. C., Neufeld, S. Q., Giovannucci, A., Friedrich, J., Pnevmatikakis, E. A., Stuber, G. D., Hen, R., Kheirbek, M. A., Sabatini, B. L., Kass, R. E., & Paninski, L. (2018). Efficient and accurate extraction of in vivo calcium signals from microendoscopic video data. *eLife*, *7*. <https://doi.org/10.7554/eLife.28728>
- Ziv, Y., Burns, L. D., Cocker, E. D., Hamel, E. O., Ghosh, K. K., Kitch, L. J., El Gamal, A., & Schnitzer, M. J. (2013). Long-term dynamics of CA1 hippocampal place codes. *Nature Neuroscience*, *16*(3), 264–266.

Supplementary Figure 1 Implant localization and pre-training neural activity.



(Continued) Supplementary Figure 1 (related to Figure 2.1) a-b. Reconstructed GRIN lens implant locations for all vCA1 **a.** and dCA1 **b.** animals used in odor-based studies. Colored lines indicate the estimated location of the lens impression left on the tissue. Atlas images adapted from (Paxinos & Keith B. J. Franklin, 2019). **c.** Time course of odor presence at the nose cone. **d.** Cross-validated neural activity during the Pre session. Each trial type (odor1 or odor2) was separated into odd and even trials, and vCA1 neural activity was z-scored. For each time bin, z-scores were averaged across all trial subsets, and sorted by peak firing rate latency during odd trials. Population mean is shown below (\pm SEM). **e.** same as d, but for dCA1.

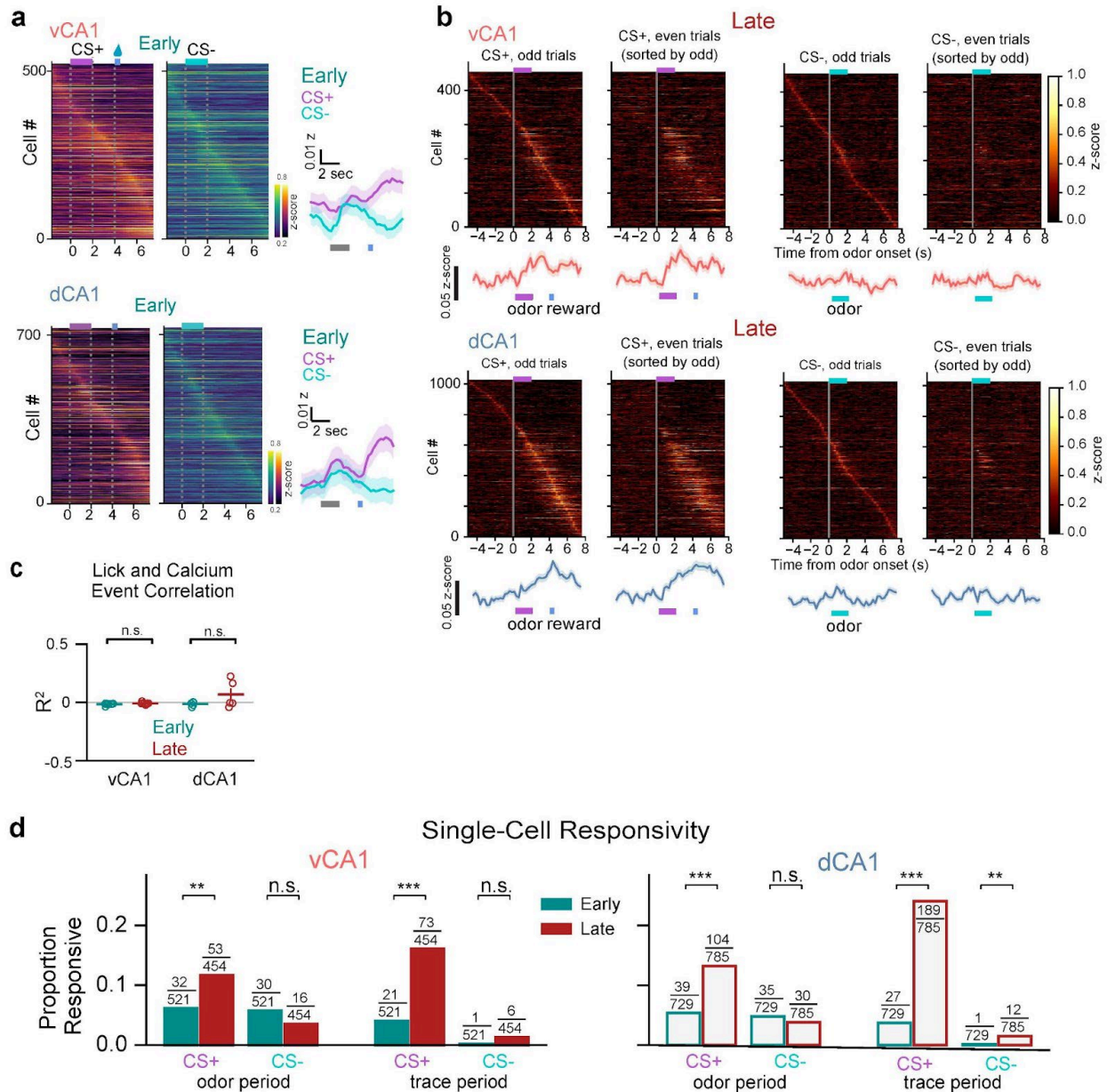
Supplementary Figure 2 Population decoding of odor presentations prior to training.



Supplementary Figure 2 (related to Figure 2.1) a-b. Decoding confusion matrices. Actual trial type is on y-axis, trial type predicted by classifier is denoted by x-axis. Odor delivery period = 0-2s; trace period = 2-4s; sucrose delivery = 4s (CS+ trials only). **c-d.** Decoding trial type when using different time bin durations over which cell activity is averaged. Regardless of time bin duration used, dCA1 shows significantly higher

decoding accuracy than vCA1 both during and soon after odor presentation. Color-coded bars above the plot show time bins where the correspondingly colored region is significantly greater (n=454 cells). **e.** Odor-period decoding. Population activity during the last second of odor delivery was used to decode odor 1 or odor 2 from baseline. Data points report results of individual decoding iterations.

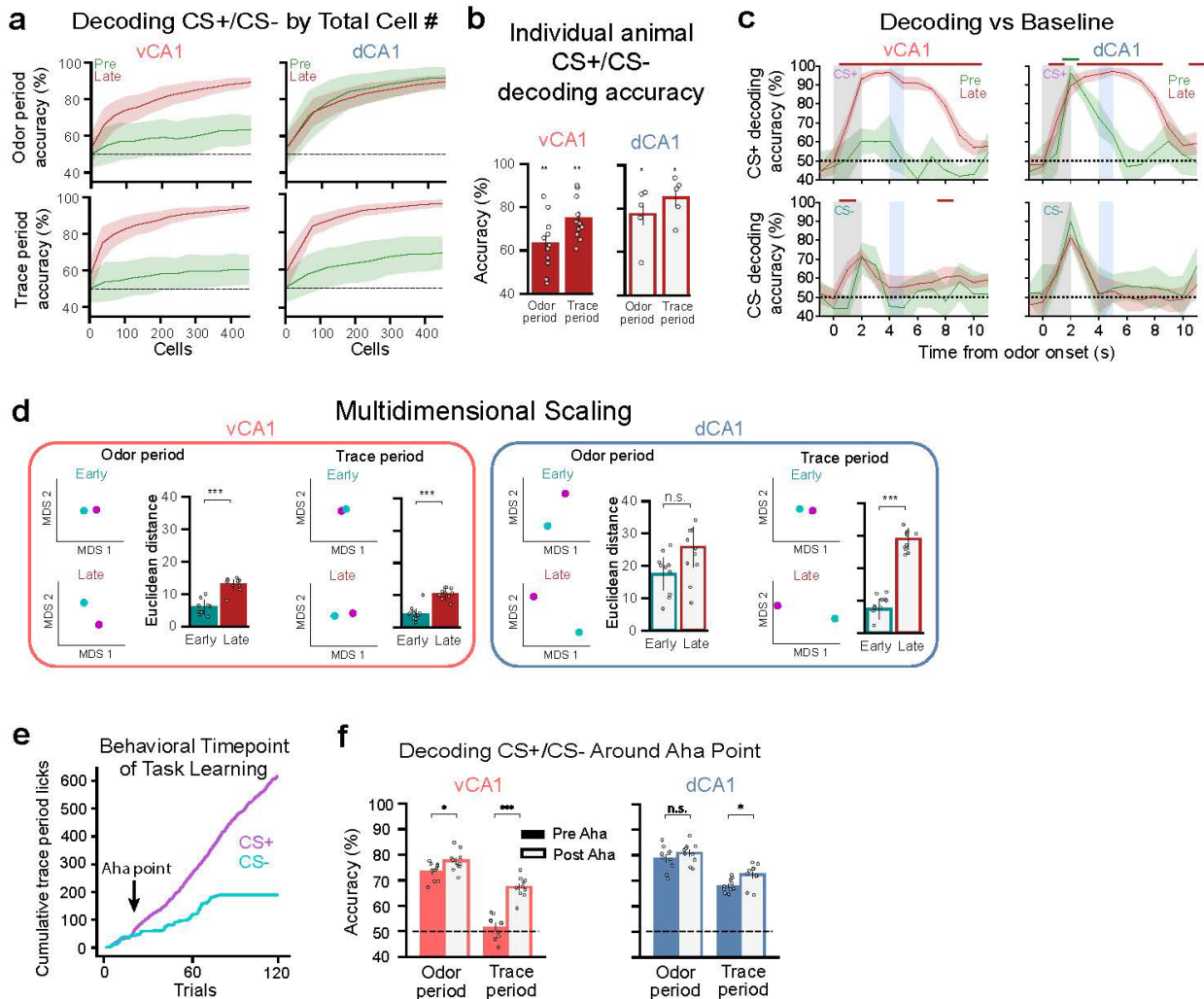
Supplementary Figure 3 Learning-related changes in neural activity.



Supplementary Figure 3 (related to Figure 2.2) a. (left) Mean z-scored fluorescent signals for all recorded cells during the Late session, ordered by peak time bin. See Fig. 2E and 2F for Late session. (right) Population mean (\pm SEM). **b.** Cross-validated neural activity. Each trial type (CS+ or CS-) was separated into odd and even trials, and neural activity was z-scored. For each time bin, z-scores were averaged across all trial subsets, and sorted by peak firing rate latency during odd trials. Population mean is shown directly below heatmap (\pm SEM). **c.** Linear regression of lick rates and Ca²⁺ in vCA1 (n = 11) and dCA1 (n = 5) during Early and Late associative learning sessions (see Methods). We found that neural activity is not significantly correlated to lick rates (R^2 is approximately zero for all animals in both sessions; t-test, $p > 0.05$). **d.** Proportion

of neurons whose activity was significantly modulated during odor- or trace-period compared to pre-odor baseline (deemed “responsive cells”). Numerator denotes the number of responsive cells. Denominator denotes the total number of cells recorded. Fisher’s exact test. Statistical power for the pre-training session (Pre) was too low for meaningful analysis (only 15 trials/trial-type in Pre vs 60 trials/trail-type in Early and Late).

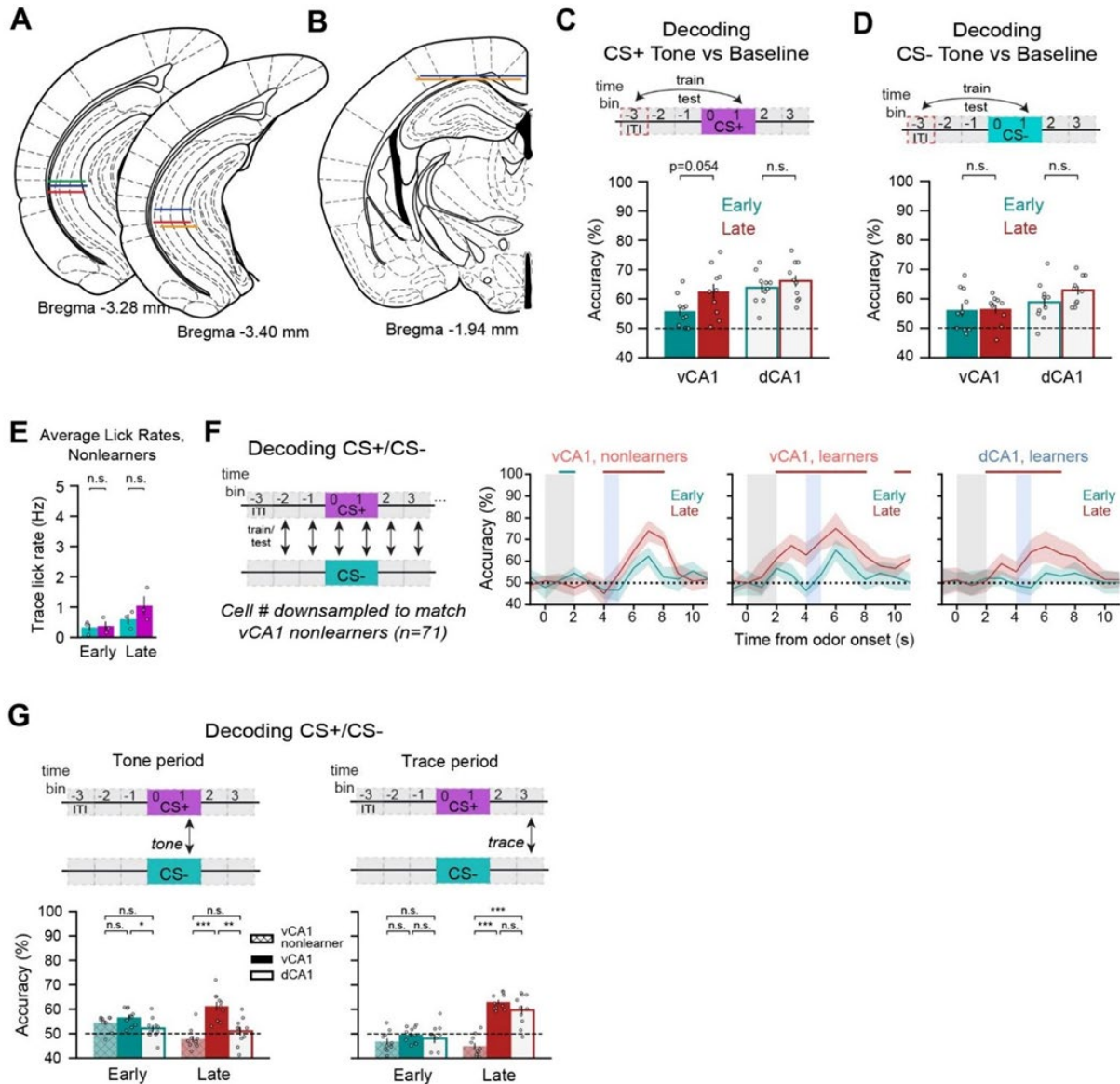
Supplementary Figure 4 Learning-related changes in population decoding.



Supplementary Figure 4 (related to Figure 2.2) a. Relationship between trial-type decoding accuracy and total number of cells included in analysis (\pm SD). **b.** Trial-type decoding accuracy for individual animals during the Late session. Here, individual data points correspond to performance of individual mice (\pm SEM, Mann-Whitney U test vs chance). **c.** Population-activity decoding accuracy for CS+ or CS- trials from baseline (\pm SD). Color-coded bar above shows periods where the corresponding trial type accuracy is significantly greater than the opposing trial type ($p < 0.01$, Mann-Whitney U test). **d.** Visualization of population activity pattern similarity for CS+ and CS- trials via MDS dimensionality reduction. Dot plots show a sample MDS run, bar charts plot the average of 10 runs (\pm SEM, Mann-Whitney U test). **e.** Sample cumulative licking during the trace period for CS+ and CS- trials from the Early and second day of learning. The Aha point, in this example at trial 20, represents the first moment the difference between the cumulative licking in CS+ and CS- trials exceeded the learning threshold (see Methods). **f.** Trial-type decoding accuracy during odor or trace periods using 30 CS+ and CS- trials before and after the Aha point. In vCA1, decoding accuracy significantly increases after the aha point for the odor and trace periods ($p < .01$ and $p < .001$,

respectively, Mann-Whitney U test). Before the aha point, decoding during trace is not significantly different from chance ($p = .88$, Wilcoxon test). In dCA1, aha decoding does not significantly increase during the odor period and increases by a small but significant amount during trace period ($p < .05$, Mann-Whitney U test). dCA1 trace period decoding before the aha point is already significantly above chance ($p < .01$, Wilcoxon test).

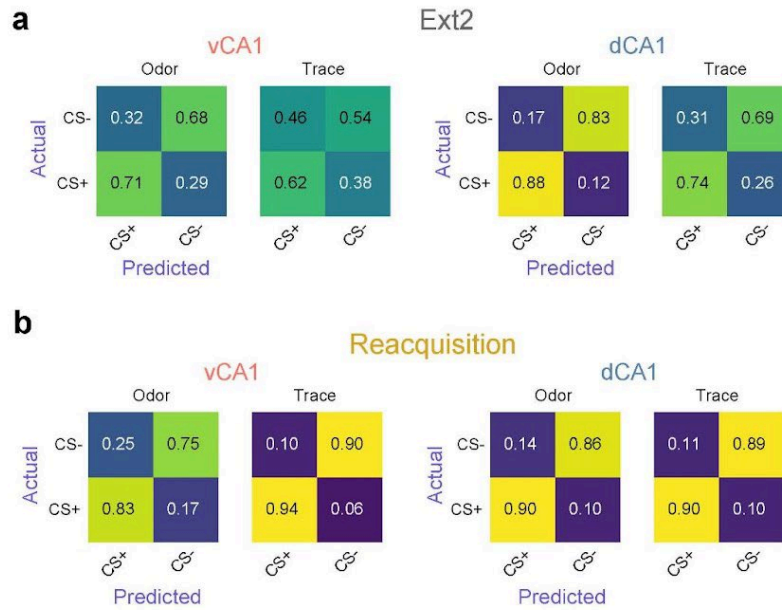
Supplementary Figure 5 Mice that fail to learn the task do not show representational changes.



Supplementary Figure 5 (related to Figure 2.3) A.-B. Location of GRIN lens implants in vCA1 **A.** and window implants in dCA1 **B.** for animals used in the tone associative learning study. Atlas images adapted from (Paxinos & Keith B. J. Franklin, 2019). **C. and D.** Population decoding CS+ (C) or CS- (D) tone vs ITI baseline **E.** Average trace-period lick rates for vCA1 animals who failed to learn the discrimination task. **F.** Trial-type decoding accuracy (±SD). Because decoding performance is correlated with the number of cells included for analysis (see Extended Data Fig. 2E), we downsampled the number of cells in vCA1 and dCA1 “learners” to each match “nonlearners” (n=71 cells). Color-coded bar above shows periods where the corresponding trial type accuracy is significantly greater than the opposing trial type (p < 0.01, Mann-Whitney U test). Note

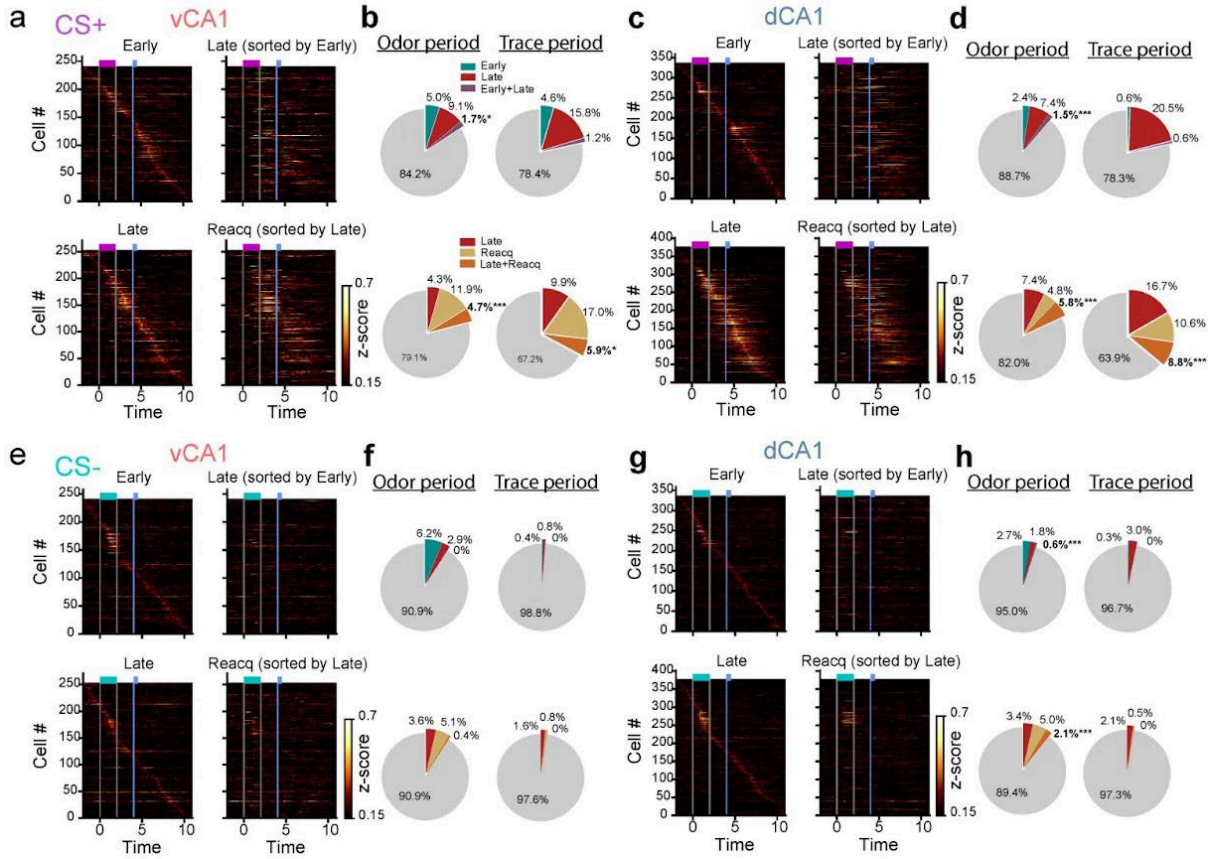
the absence of odor- and trace-period decoding in nonlearners during the Late session.
G. Trial-type decoding performance during the odor- (left) and trace-period (right) epochs (\pm SEM, Mann-Whitney U test).

Supplementary Figure 6 Decoding Confusion Matrices

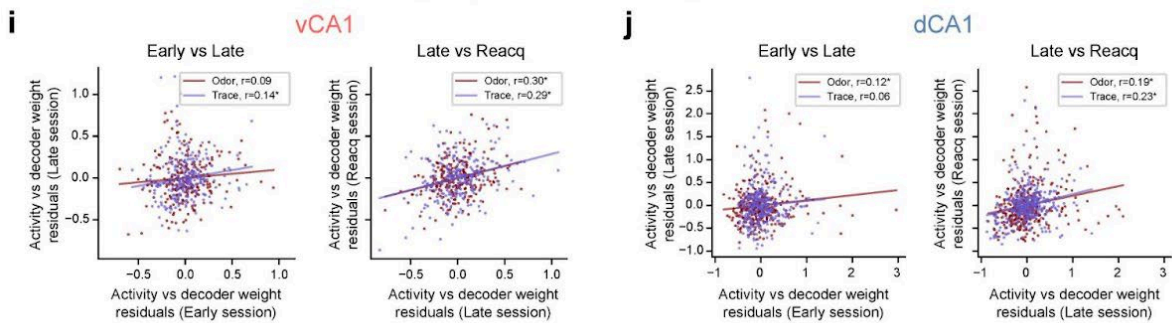


Supplementary Figure 6 (Related to Figure 2.4) a.-b. Decoding confusion matrices for **a.** Extinction day 2 and **b.** Reacquisition sessions.

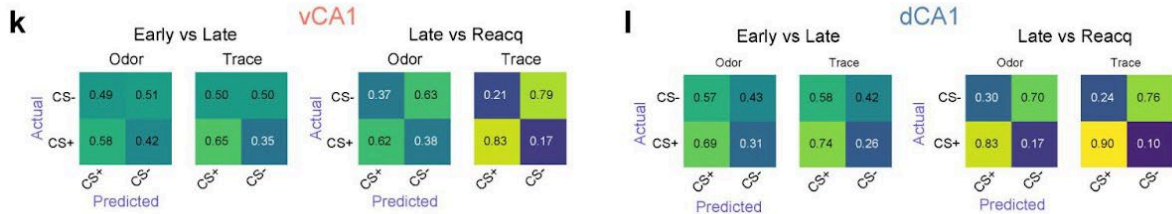
Supplementary Figure 7 Tracking Single-cell and population dynamics across training reveals stability of task encoding accompanies learning.



Correlating single-cell decoder weights across sessions

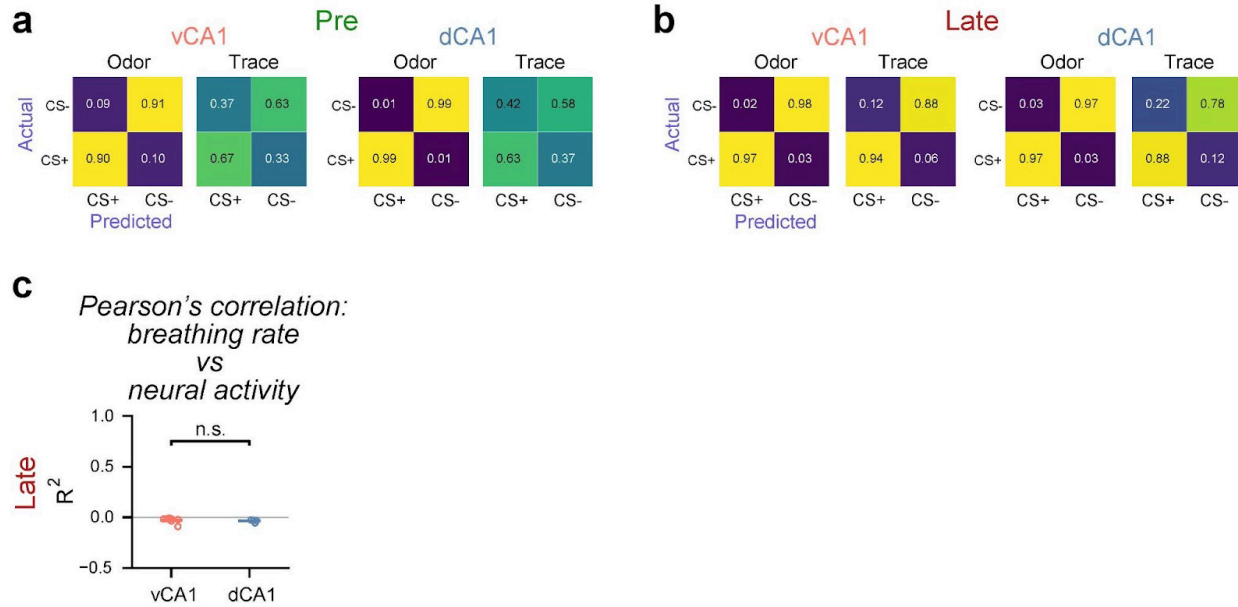


Decoding confusion matrices



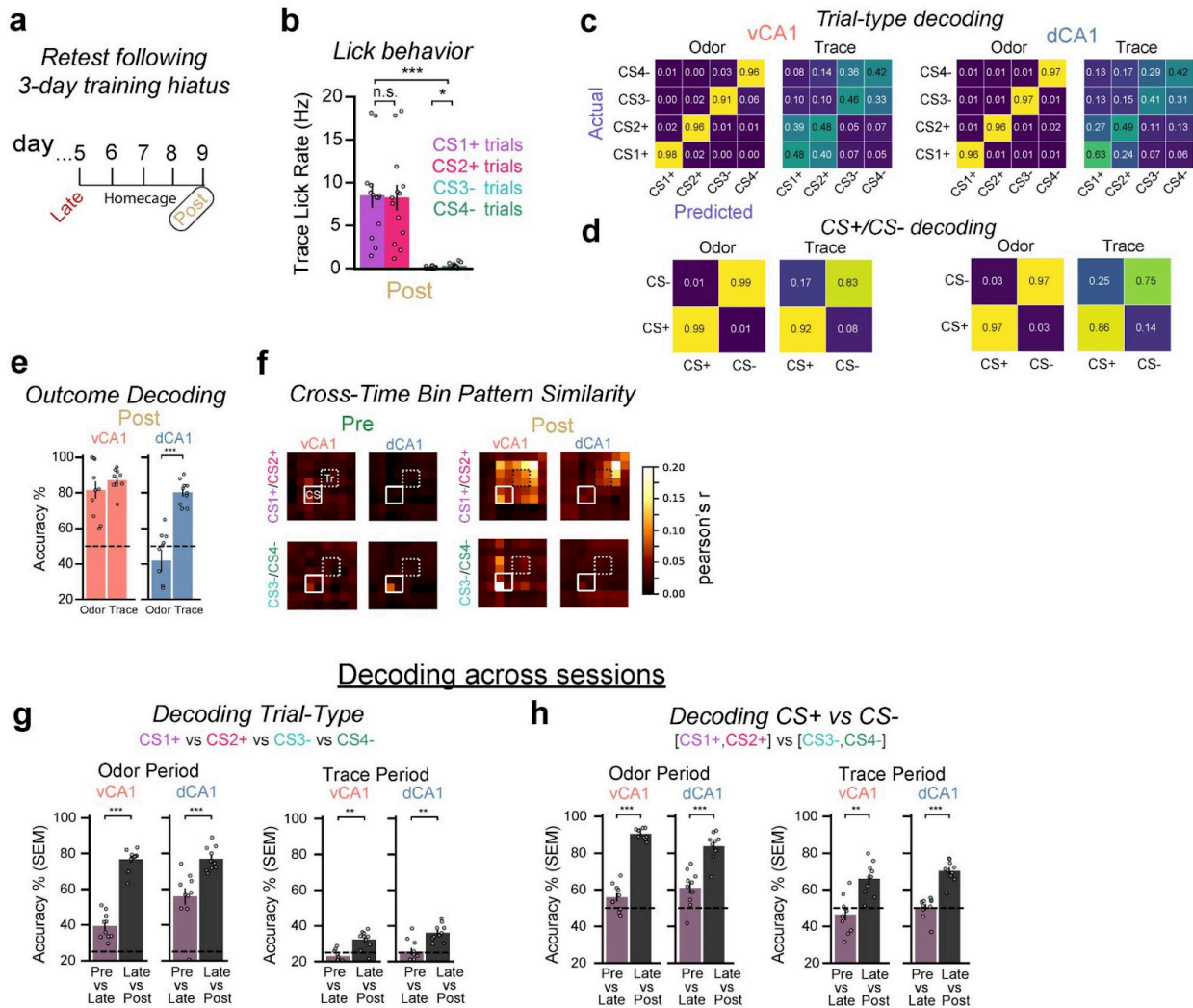
(Continued) Supplemental Figure 7 (related to Figure 2.5) a,c. Activity during CS+ trials for neurons registered across specific session pairs. For each time bin, activity z-scores for each neuron were averaged across all trials within a session, and neurons were sorted by peak firing rate latency during the indicated session. Note the changing subset of task-responsive cells from Early to Late, and the relative stability following learning (Late to Reacquisition). **b,d.** Quantification of cells with increased responsiveness to different task epochs. Individual cells show high remapping of responsiveness to CS+ task epochs across Early and Late sessions, but increased stability from Late to Reacquisition. **e-h.** Same as in a-d, but for CS- trials. **i, j.** Comparison of weights assigned to individual cells during decoding analysis; higher weight indicates greater importance for encoding (Stefanini et al., 2020). As activity is correlated with assigned weight, we plotted weights values after regressing out the components explained by the activity. We find an increased correlation of weight values after learning (Late and Reacquisition) compared to initial training (Early/Late), supporting a stabilization of task representations accompanies learning. **k, l.** Confusion matrices for across-session decoding.

Supplemental Figure 8. Confusion matrices and breath correlation



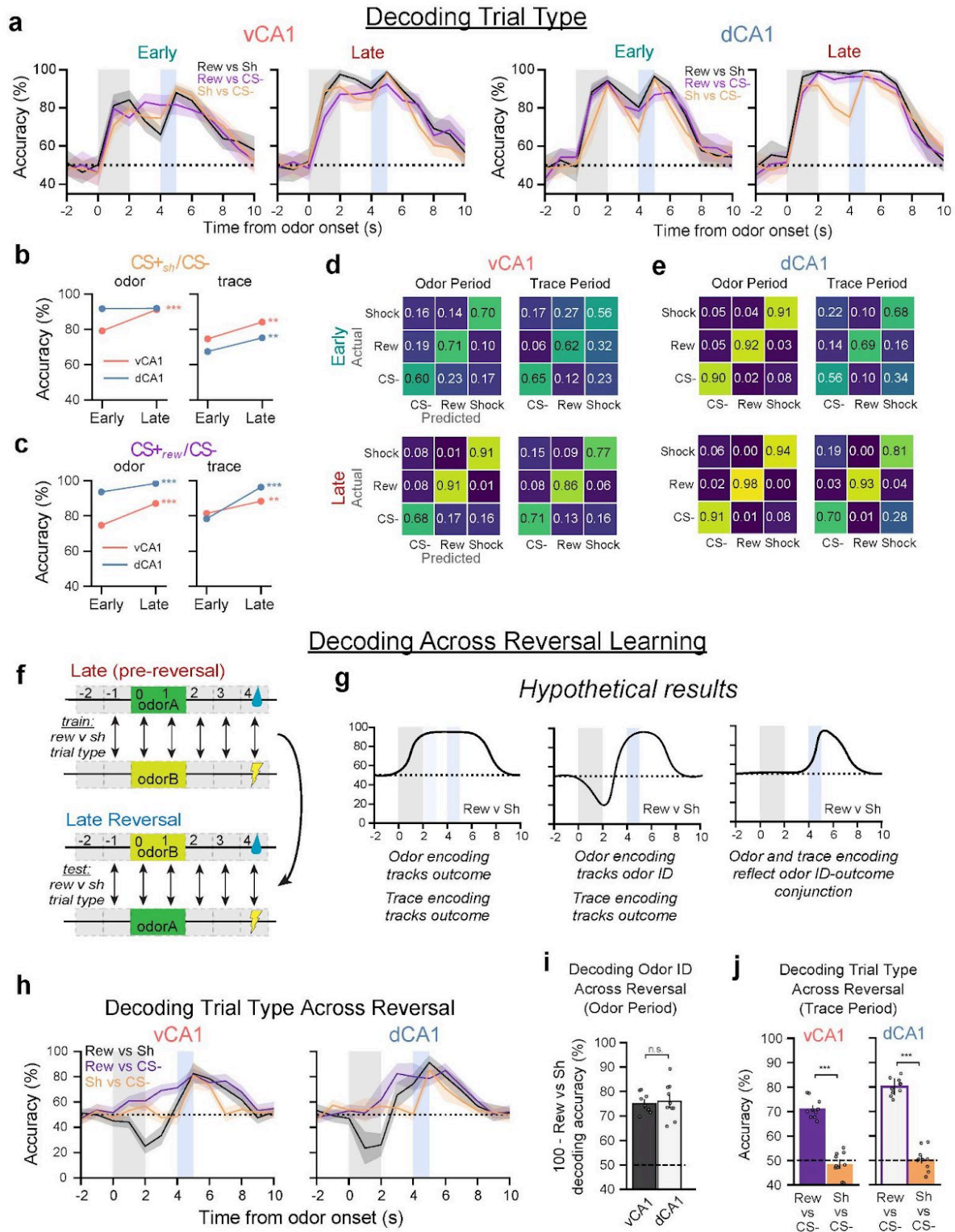
Supplemental Figure 8 (related to Figure 2.7) a-b. Confusion matrices for CS+ vs CS- trial type classification. **c.** Breathing rate was not correlated with calcium event activity in either hippocampal region. Data points represent individual animals (n= 11 vCA1, 5 dCA1). Data taken from Late session.

Supplemental Figure 9 Task representations show increased stability with learning following a break in training.



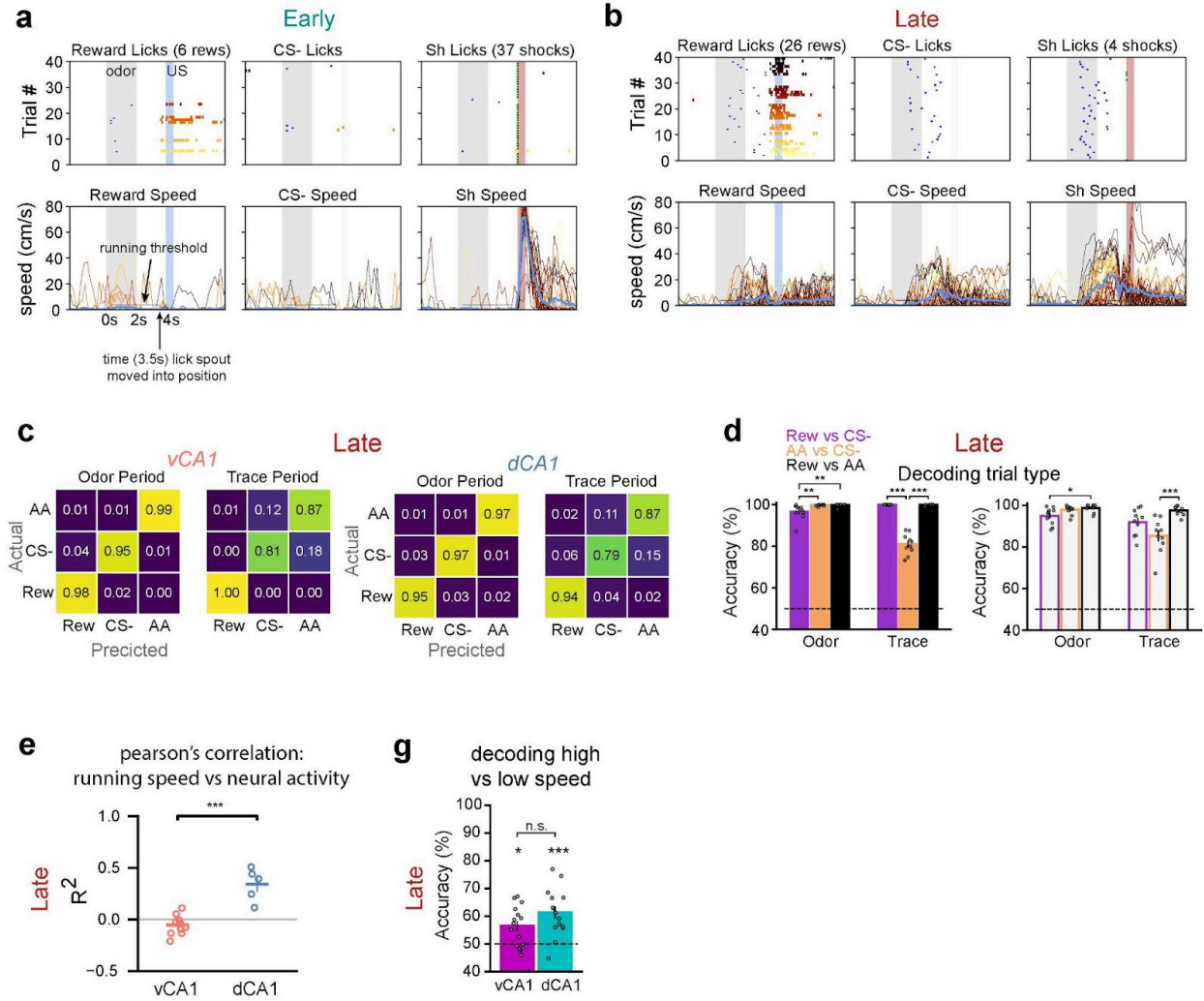
Supplemental Figure 9 (related to figure 2.7) a. In the 2-odor task, Late and Reacquisition sessions were separated by multiple extinction sessions. To assess how task representations may change across a similar time period, but with no additional task experience, following learning of the 4-odor task, mice were kept in their homecage and rerun on the learned task 4 days later (Post). **b.** Mean lick rate during the trace period for all animals (\pm SEM, Mann-Whitney U test). Data points represent individual animals ($n = 8$ vCA1, 5 dCA1). **c-d.** Trial-type and CS+ vs CS- decoding accuracies were similar for the Post session (shown here) compared to Late (Fig. 5c and Extended Data Figure 7 a, b; Analyses used 150 cells for each region). **e, f.** Also similar to the Late session, odor and outcome information were multiplexed in vCA1 during the odor delivery period, while outcome information was present in both vCA1 and dCA1 during trace (\pm SEM, Mann-Whitney U test). **g.** Task representations showed greater stability once learned. Analyses used cells registered across all 3 sessions (Analyses used 100 cells for each region). Each data point represents an individual decoding run. **h.** Same as in g, but decoding CS+ vs CS- across sessions.

Supplemental Figure 10 Odor ID and reward expectation representations remain stable across reversal learning, while shock anticipation signals fade.



(Continued) Supplemental Figure 10 (related to Figure 2.8) **a.** Trial-type decoding accuracy (\pm SD). Analyses used 444 cells for each region in a - e. Rew = reward trial. Sh = shock trial. **b.** Change in odor-period (left) or trace-period (right) decoding accuracies for CS+shock vs CS- trials from Early to Late sessions (\pm SEM). Statistics compare Early and Late sessions for a specific hippocampal region (Mann-Whitney U test). **c.** Same as in b but decoding CS+reward from CS- trials. **d-e.** Confusion matrices for trial-type decoding accuracy during Early (upper) or Late (lower) sessions. **f.** Schematic illustrating trial-type decoding across reversal learning. **g.** Hypothetical results for decoding CS+reward from CS+shock trials across reversal learning (for this set of results, stable encoding of US identity across reversal is assumed). Because data classes were labeled with respect to the outcome of a trial, and not the odor identity, stable neural representations of odor identity will manifest as cross-session decoding accuracies that are below chance (middle graph). **h.** Actual results for decoding trial type across reversal learning (\pm SD). The below chance decoding accuracy for CS+reward vs CS+shock during the odor period indicates representations of odor identity dominate the population activity during this time. Analyses used 281 cells for each region. **i.** Across-reversal odor ID decoding accuracy during the odor period (\pm SEM, Mann-Whitney U test). **j.** Across-reversal trial type decoding accuracy during the trace period (\pm SEM, Mann-Whitney U test).

Supplemental Figure 11 Headfixed active avoidance task results.



Supplemental Figure 11 (related to Figure 2.9) a. Lick (top) and running (bottom) behavior from an example mouse during the first day of training. Trial number is color-coded, yellow to black. During the first day of training, the mouse had very few trials with suprathreshold running, leading to few rewards and numerous shock deliveries. Shock delivery resulted in rapid, transient running. Vertical grey bar = odor delivery period; vertical blue/red bar = time of sucrose/shock delivery onset (on applicable trials). Blue ticks = time point when running exceeded threshold. Green ticks denote trials where shock was delivered. Light blue trace = average running speed. Sh = shock odor trial. **b.** Same as in a, but Late session for the same mouse. **c.** Confusion matrices for Late session. Only suprathreshold trials were included for analysis. Overall, classification accuracy was high for all trial types. However, there was a tendency for active avoidance (AA) and CS- trials to be confused with one another. Interestingly, animals also exhibited suprathreshold running during CS- trials (**Figure 2.8c**), despite it being inconsequential for the task, suggesting animals may have interpreted CS- trials as a potential predictor of shock. Analyses used 340 cells for both regions. **d.** Pairwise decoding trial type. While active avoidance trials are well discriminated from rewarded trials, decoding accuracy was lower for AA vs CS- trials during the trace period (\pm SEM, Mann-Whitney U test).

e. Running was not correlated with vCA1 neural activity, but was moderately correlated with dCA1 activity (\pm SEM, Mann-Whitney U test). Data is from Late session. **f.** To further assess how running may have contributed to our results, we trained a linear classifier to decode high vs low speed running trials during time bins outside of the task (5-10 seconds post odor delivery). While running speed could be decoded above chance in both regions, decoding was relatively weak. Significance stars above individual bars report significance level versus 50% chance decoding accuracy (\pm SEM, Wilcoxon signed-rank test).

Supplementary Table 1 (related to all Figures). Summary of statistics in all figure panels in manuscript.

Figure	Variable	Unit of Comparison	n	Test	Results
Fig. 2.1g	odor1/odor2 decoding accuracy, vCA1 vs dCA1	10 decoding iterations for each region	n-matched pseudopopulation of 454 cells from 11 vCA1 and 5 dCA1 mice	Mann-Whitney U	colored-coded bar above graph shows time bins where $p < 0.01$
Fig. 2.1i	decoding accuracy vs chance	10 decoding iterations for each region	pseudopopulation (see methods) of 454 cells (n-matched in vCA1 and dCA1) from 11 vCA1 and 5 dCA1 mice	Wilcoxon	color-coded bars above graph show time bins where $p < 0.01$
Fig. 2.2D	mean lick rate (Hz)	Trial type (Early session)	16 mice (11 vCA1 and 5 dCA1 mice)	Mann-Whitney U	$U = 75.5$, $p = 0.13$, effectsize (r) = 0.28
Fig. 2.2D	mean lick rate (Hz)	Trial type (Late session)	16 mice (11 vCA1 and 5 dCA1 mice)	Mann-Whitney U	$U = 0$, $p < 0.0001$, effectsize (r) = 0.85
Fig. 2.2h	vCA1 vs dCA1 CS+/CS- decoding accuracies during odor period (Pre session)	10 decoding iterations for each region	n-matched pseudopopulation of 454 cells from 11 vCA1 and 4 dCA1 mice	Mann-Whitney U	$U = 0$, $p = 0.00018$, effect-size (r) = 0.85
Fig. 2.2h	vCA1 vs dCA1 CS+/CS- decoding accuracies during odor period (Late session)	10 decoding iterations for each region	n-matched pseudopopulation of 454 cells from 11 vCA1 and 5 dCA1 mice	Mann-Whitney U	$U = 44$, $p = 0.68$, effectsize (r) = 0.10
Fig. 2.2h	vCA1 vs dCA1 CS+/CS- decoding accuracies during trace period (Pre session)	10 decoding iterations for each region	n-matched pseudopopulation of 454 cells from 11 vCA1 and 4 dCA1 mice	Mann-Whitney U	$U = 25$, $p = 0.064$, effect-size (r) = 0.42
Fig. 2.2h	vCA1 vs dCA1 CS+/CS- decoding accuracies during trace period (Late session)	10 decoding iterations for each region	n-matched pseudopopulation of 454 cells from 11 vCA1 and 5 dCA1 mice	Mann-Whitney U	$U = 32$, $p = 0.18$, effectsize (r) = 0.30
Fig. 2.2i	CS+/baseline vs CS-/baseline decoding accuracies, vCA1 or dCA1	10 decoding iterations for each trial type	n-matched pseudopopulation of 454 cells from 11 vCA1 or 5 dCA1 mice	Mann-Whitney U	color-coded bars above graph show time bins where $p < 0.01$
Fig. 2.2j	vCA1 vs dCA1 CS+/baseline decoding accuracies during odor period (Pre session)	10 decoding iterations for each region	n-matched pseudopopulation of 454 cells from 11 vCA1 and 4 dCA1 mice	Mann-Whitney U	$U = 0$, $p = 0.00017$, effect-size (r) = 0.85
Fig. 2.2j	vCA1 vs dCA1 CS+/baseline decoding accuracies during odor period (Late session)	10 decoding iterations for each region	n-matched pseudopopulation of 454 cells from 11 vCA1 and 5 dCA1 mice	Mann-Whitney U	$U = 69.5$, $p = 0.15$, effect-size (r) = 0.33
Fig. 2.2j	vCA1 vs dCA1 CS+/baseline decoding accuracies during trace period (Pre session)	10 decoding iterations for each region	n-matched pseudopopulation of 454 cells from 11 vCA1 and 4 dCA1 mice	Mann-Whitney U	$U = 25.5$, $p = 0.069$, effect-size (r) = 0.41
Fig. 2.2j	vCA1 vs dCA1 CS+/baseline decoding accuracies during trace period (Late session)	10 decoding iterations for each region	n-matched pseudopopulation of 454 cells from 11 vCA1 and 5 dCA1 mice	Mann-Whitney U	$U = 56$, $p = 0.68$, effectsize (r) = 0.10
Fig. 2.2k	odor period vs trace period decoding accuracy vs chance	10 decoding iterations	pseudopopulation of 454 cells from 11 vCA1 mice	Wilcoxon	$W = 0$, $p = 0.005$, effectsize (r) = 0.85
Fig. 2.2k	odor period vs trace period decoding accuracy vs chance	10 decoding iterations	pseudopopulation of 454 cells from 5 dCA1 mice	Wilcoxon	$W = 0$, $p = 0.005$, effectsize (r) = 0.85
Fig. 2.3C	mean lick rate (Hz)	Trial type (Early session)	6 mice (4 vCA1, 2 dCA1)	Mann-Whitney U	$U = 82$, $p = 0.21$, effectsize (r) = 0.22
Fig. 2.3C	mean lick rate (Hz)	Trial type (Late session)	6 mice (4 vCA1, 2 dCA1)	Mann-Whitney U	$U = 0$, $p < 0.0001$, effectsize (r) = 0.85
Fig. 2.3D	decoding accuracy vs chance, vCA1 vs dCA1	10 decoding iterations for each region	n-matched pseudopopulation of 537 cells from 4 vCA1 and 2 dCA1 mice	Wilcoxon	color-coded bars above graph show time bins where $p < 0.01$

Figure	Variable	Unit of Comparison	n	Test	Results
Fig. 2.3E	vCA1 vs dCA1 CS+/baseline decoding accuracies during tone period (Early session)	10 decoding iterations for each region	n-matched pseudopopulation of 537 cells from 4 vCA1 and 2 dCA1 mice	Mann-Whitney U	U = 15, p = 0.009, effect-size (r) = 0.59
Fig. 2.3E	vCA1 vs dCA1 CS+/baseline decoding accuracies during tone period (Late session)	10 decoding iterations for each region	n-matched pseudopopulation of 537 cells from 4 vCA1 and 2 dCA1 mice	Mann-Whitney U	U = 38, p = 0.38, effectsize (r) = 0.2
Fig. 2.3E	vCA1 vs dCA1 CS+/baseline decoding accuracies during trace period (Early session)	10 decoding iterations for each region	n-matched pseudopopulation of 537 cells from 4 vCA1 and 2 dCA1 mice	Mann-Whitney U	U = 89, p = 0.004, effect-size (r) = 0.66
Fig. 2.3E	vCA1 vs dCA1 CS+/baseline decoding accuracies during trace period (Late session)	10 decoding iterations for each region	n-matched pseudopopulation of 537 cells from 4 vCA1 and 2 dCA1 mice	Mann-Whitney U	U = 40.5, p = 0.5, effectsize (r) = 0.16
Fig. 2.3F	CS+/CS- decoding accuracy, vCA1 vs dCA1	10 decoding iterations for each region	n-matched pseudopopulation of 537 cells from 4 vCA1 and 2 dCA1 mice	Mann-Whitney U	colored-coded bar above graph shows time bins where p < 0.01
Fig. 2.3G	vCA1 vs dCA1 CS+/CS- decoding accuracies during tone period (Early session)	10 decoding iterations for each region	n-matched pseudopopulation of 537 cells from 4 vCA1 and 2 dCA1 mice	Mann-Whitney U	U = 52, p = 0.91, effectsize (r) = 0.03
Fig. 2.3G	vCA1 vs dCA1 CS+/CS- decoding accuracies during tone period (Late session)	10 decoding iterations for each region	n-matched pseudopopulation of 537 cells from 4 vCA1 and 2 dCA1 mice	Mann-Whitney U	U = 99, p < 0.001, effect-size (r) = 0.82
Fig. 2.3G	vCA1 vs dCA1 CS+/CS- decoding accuracies during trace period (Early session)	10 decoding iterations for each region	n-matched pseudopopulation of 537 cells from 4 vCA1 and 2 dCA1 mice	Mann-Whitney U	U = 77, p = 0.045, effect-size (r) = 0.46
Fig. 2.3G	vCA1 vs dCA1 CS+/CS- decoding accuracies during trace period (Late session)	10 decoding iterations for each region	n-matched pseudopopulation of 537 cells from 4 vCA1 and 2 dCA1 mice	Mann-Whitney U	U = 51, p = 0.97, effectsize (r) = 0.02
Fig. 2.4e	Ext vs Reacq CS+/CS- decoding accuracies during odor period (dCA1)	10 decoding iterations for each	n-matched pseudopopulation of 454 cells from 4 dCA1 mice	Mann-Whitney U, Bonferroni correction for n=3	U = 42, p = 1, effect-size (r) = 0.13
Fig. 2.4e	Early vs Late CS+/CS- decoding accuracies during odor period (vCA1)	10 decoding iterations for each	n-matched pseudopopulation of 454 cells from 11 vCA1 mice	Mann-Whitney U, Bonferroni correction for n=3	U = 0, p < 0.001, effectsize (r) = 0.85
Fig. 2.4e	Early vs Ext CS+/CS- decoding accuracies during odor period (vCA1)	10 decoding iterations for each	n-matched pseudopopulation of 454 cells from 11 vCA1 mice	Mann-Whitney U, Bonferroni correction for n=3	U = 58.5, p = 1, effectsize (r) = 0.14
Fig. 2.4e	Early vs Reacq CS+/CS- decoding accuracies during odor period (vCA1)	10 decoding iterations for each	n-matched pseudopopulation of 454 cells from 11 vCA1 mice	Mann-Whitney U, Bonferroni correction for n=3	U = 0, p < 0.001, effectsize (r) = 0.85
Fig. 2.4e	Late vs Ext CS+/CS- decoding accuracies during odor period (vCA1)	10 decoding iterations for each	n-matched pseudopopulation of 454 cells from 11 vCA1 mice	Mann-Whitney U, Bonferroni correction for n=3	U = 0, p < 0.001, effectsize (r) = 0.85
Fig. 2.4e	Late vs Reacq CS+/CS- decoding accuracies during odor period (vCA1)	10 decoding iterations for each	n-matched pseudopopulation of 454 cells from 11 vCA1 mice	Mann-Whitney U, Bonferroni correction for n=3	U = 46.5, p = 1., effectsize (r) = 0.14
Fig. 2.4e	Ext vs Reacq CS+/CS- decoding accuracies during odor period (vCA1)	10 decoding iterations for each	n-matched pseudopopulation of 454 cells from 11 vCA1 mice	Mann-Whitney U, Bonferroni correction for n=3	U = 0, p < 0.001, effectsize (r) = 0.85
Fig. 2.4e	Early vs Late CS+/CS- decoding accuracies during odor period (dCA1)	10 decoding iterations for each	n-matched pseudopopulation of 454 cells from 4 dCA1 mice	Mann-Whitney U, Bonferroni correction for n=3	U = 0, p < 0.001, effectsize (r) = 0.85
Fig. 2.4e	Early vs Ext CS+/CS- decoding accuracies during odor period (dCA1)	10 decoding iterations for each	n-matched pseudopopulation of 454 cells from 4 dCA1 mice	Mann-Whitney U, Bonferroni correction for n=3	U = 26, p = 0.23, effectsize (r) = 0.41
Fig. 2.4e	Early vs Reacq CS+/CS- decoding accuracies during odor period (dCA1)	10 decoding iterations for each	n-matched pseudopopulation of 454 cells from 4 dCA1 mice	Mann-Whitney U, Bonferroni correction for n=3	U = 0, p < 0.001, effectsize (r) = 0.85
Fig. 2.4e	Late vs Ext CS+/CS- decoding accuracies during odor period (dCA1)	10 decoding iterations for each	n-matched pseudopopulation of 454 cells from 4 dCA1 mice	Mann-Whitney U, Bonferroni correction for n=3	U = 0, p < 0.001, effectsize (r) = 0.85
Figure	Variable	Unit of Comparison	n	Test	Results

Figure	Variable	Unit of Comparison	n	Test	Results
Fig. 2.4e	Late vs Reacq CS+/CS- decoding accuracies during odor period (dCA1)	10 decoding iterations for each	n-matched pseudopopulation of 454 cells from 4 dCA1 mice	Mann-Whitney U, Bonferroni correction for n=3	U = 80.5, p = 0.07, effect-size (r) = 0.52
Fig. 2.4e	Ext vs Reacq CS+/CS- decoding accuracies during odor period (dCA1)	10 decoding iterations for each	n-matched pseudopopulation of 454 cells from 4 dCA1 mice	Mann-Whitney U, Bonferroni correction for n=3	U = 0, p < 0.001, effect-size (r) = 0.85
Fig. 2.5c	Across-session Early/Late vs Late/Reacq CS+/CS- decoding accuracies during odor period (vCA1)	10 decoding iterations for each	n-matched pseudopopulation of 241 cells from 10 vCA1 mice	Mann-Whitney U	U = 10, p = 0.003, effect-size (r) = 0.68
Fig. 2.5c	Across-session Early/Late vs Late/Reacq CS+/CS- decoding accuracies during odor period (dCA1)	10 decoding iterations for each	n-matched pseudopopulation of 241 cells from 4 dCA1 mice	Mann-Whitney U	U = 0, p < 0.001, effect-size (r) = 0.85
Fig. 2.5c	Across-session Early/Late vs Late/Reacq CS+/CS- decoding accuracies during trace period (vCA1)	10 decoding iterations for each	n-matched pseudopopulation of 241 cells from 10 vCA1 mice	Mann-Whitney U	U = 0, p < 0.001, effect-size (r) = 0.85
Fig. 2.5c	Across-session Early/Late vs Late/Reacq CS+/CS- decoding accuracies during trace period (dCA1)	10 decoding iterations for each	n-matched pseudopopulation of 241 cells from 4 dCA1 mice	Mann-Whitney U	U = 0, p < 0.001, effect-size (r) = 0.85
Fig. 2.5d	Early/Late vs Late/Reacq, odor period, CS- trials (vCA1)	Euclidean distance between MDS values	10 MDS runs	Mann-Whitney U, bonferroni correction for n=2	U = 78, p = 0.038, effect-size (r) = 0.47
Fig. 2.5d	Early/Late vs Late/Reacq, odor period, CS+ trials (vCA1)	Euclidean distance between MDS values	10 MDS runs	Mann-Whitney U, bonferroni correction for n=2	U = 100, p = 0.0002, effect-size (r) = 0.85
Fig. 2.5d	Early/Late vs Late/Reacq, odor period, CS- trials (dCA1)	Euclidean distance between MDS values	10 MDS runs	Mann-Whitney U, bonferroni correction for n=2	U = 37, p = 0.35, effect-size (r) = 0.22
Fig. 2.5d	Early/Late vs Late/Reacq, odor period, CS+ trials (dCA1)	Euclidean distance between MDS values	10 MDS runs	Mann-Whitney U, bonferroni correction for n=2	U = 46, p = 0.79, effect-size (r) = 0.07
Fig. 2.5e	Early/Late vs Late/Reacq, trace period, CS- trials (vCA1)	Euclidean distance between MDS values	10 MDS runs	Mann-Whitney U, bonferroni correction for n=2	U = 58, p = 0.57, effect-size (r) = 0.14
Fig. 2.5e	Early/Late vs Late/Reacq, trace period, CS+ trials (vCA1)	Euclidean distance between MDS values	10 MDS runs	Mann-Whitney U, bonferroni correction for n=2	U = 81, p = 0.021, effect-size (r) = 0.52
Fig. 2.5e	Early/Late vs Late/Reacq, traceperiod, CS- trials (dCA1)	Euclidean distance between MDS values	10 MDS runs	Mann-Whitney U, bonferroni correction for n=2	U = 56, p = 0.68, effect-size (r) = 0.1
Fig. 2.5e	Early/Late vs Late/Reacq, trace period, CS+ trials (dCA1)	Euclidean distance between MDS values	10 MDS runs	Mann-Whitney U, bonferroni correction for n=2	U = 97, p = < 0.001, effect-size (r) = 0.79
Fig. 2.6B	CS+/CS- decoding accuracy, vCA1 vs dCA1	10 decoding iterations for each	n-matched pseudopopulation of 339 cells from 7 vCA1 and 2 dCA1 mice	Mann-Whitney U	see figure for colorcoded p-values
Fig. 2.6C	CS+/CS- Early decoding accuracy, vCA1 vs dCA1	n = 19 (mean of each time bin x vs time bin y decoding result (each blue square in fig))	n-matched pseudopopulation of 339 cells from 7 vCA1 and 2 dCA1 mice	Mann-Whitney U	U = 254, p = 0.033, effect-size (r) = 0.35
Fig. 2.6C	CS+/CS- Late decoding accuracy, vCA1 vs dCA1	n = 19 (mean of each time bin x vs time bin y decoding result (each blue square in fig))	n-matched pseudopopulation of 339 cells from 7 vCA1 and 2 dCA1 mice	Mann-Whitney U	U = 313, p < 0.001., effect-size (r) = 0.63
Fig. 2.6C	CS+/CS- Extinction decoding accuracy, vCA1 vs dCA1	n = 19 (mean of each time bin x vs time bin y decoding result (each blue square in fig))	n-matched pseudopopulation of 339 cells from 7 vCA1 and 2 dCA1 mice	Mann-Whitney U	U = 236.5, p = 0.11, effect-size (r) = 0.27

Figure	Variable	Unit of Comparison	n	Test	Results
Fig. 2.6C	CS+/CS- Reacquisition decoding accuracy, vCA1 vs dCA1	n = 19 (mean of each time bin x vs time bin y decoding result (each blue square in fig))	n-matched pseudopopulation of 339 cells from 7 vCA1 and 2 dCA1 mice	Mann-Whitney U	U = 321, p < 0.001, effect-size (r) = 0.67
				region	F = 35.2, p < 0.001, effect size (ETA^2) = .31
				odor	F = 1.21, p = 0.31, effect size (ETA^2) = .03
				region*odor	F = 1.4, p = 0.25, effect size (ETA^2) = .04
Fig. 2.7d	Trial type decoding accuracy, Pre vs Late, odor period (vCA1)	10 decoding iterations for each session	n-matched pseudopopulation of 150 cells from 8 vCA1 mice	Mann-Whitney U	U = 19.5, p = 0.023, effect-size (r) = 0.52
Fig. 2.7d	Trial type decoding accuracy, Pre vs Late, odor period (dCA1)	10 decoding iterations for each session	n-matched pseudopopulation of 150 cells from 5 dCA1 mice	Mann-Whitney U	U = 37.5, p = 0.36, effect-size (r) = 0.21
Fig. 2.7e	trial type decoding accuracy, Late session	10 decoding iterations each	n-matched pseudopopulation of 150 cells from 8 vCA1 mice	One-way ANOVA	
				region	F = 36.5, p < 0.001, effect size (ETA^2) = .34
				odor	F = 1.17, p = 0.33, effect size (ETA^2) = .03
				region*odor	F = 1.15, p = 0.22, effect size (ETA^2) = .04
Fig. 2.7f	CS+ vs CS- decoding accuracy, Pre vs Late, odor period (vCA1)	10 decoding iterations for each session	n-matched pseudopopulation of 150 cells from 8 vCA1 mice	Mann-Whitney U	U = 1.0, p < 0.001, effect-size (r) = 0.83
Fig. 2.7f	CS+ vs CS- decoding accuracy, Pre vs Late, odor period (dCA1)	10 decoding iterations for each session	n-matched pseudopopulation of 150 cells from 5 dCA1 mice	Mann-Whitney U	U = , p < 0.001, effectsize (r) = 0.85
Fig. 2.7h	outcome decoding, Pre vs Late, odor period (vCA1)	10 decoding iterations for each	n-matched pseudopopulation of 150 cells from 8 vCA1 mice	Mann-Whitney U	U = 11.5, p = 0.004, effect-size (r) = 0.65
Fig. 2.7h	outcome decoding, Pre vs Late, odor period (dCA1)	10 decoding iterations for each	n-matched pseudopopulation of 150 cells from 5 dCA1 mice	Mann-Whitney U	U = 48, p = 0.91, effectsize (r) = 0.03
Fig. 2.7h	outcome decoding, Pre vs Late, trace period (vCA1)	10 decoding iterations for each	n-matched pseudopopulation of 150 cells from 8 vCA1 mice	Mann-Whitney U	U = 0, p < 0.001, effectsize (r) = 0.85
Fig. 2.7h	outcome decoding, Pre vs Late, trace period (dCA1)	10 decoding iterations for each	n-matched pseudopopulation of 150 cells from 5 dCA1 mice	Mann-Whitney U	U = 9.5, p = 0.002, effect-size (r) = 0.68
Fig. 2.7j	CS+/CS- vs CS1+/CS2+, odor period, Pre session (vCA1)	Euclidean distance between MDS values	10 MDS runs	Mann-Whitney U, bonferroni correction for n=2	U = 91, p = 0.004, effect-size (r) = 0.69
Fig. 2.7j	CS+/CS- vs CS3-/CS4-, odor period, Pre session (vCA1)	Euclidean distance between MDS values	10 MDS runs	Mann-Whitney U, bonferroni correction for n=2	U = 27, p = 0.18, effectsize (r) = 0.39
Fig. 2.7j	CS1+/CS2+ vs CS3-/CS4-, odor period, Pre session (vCA1)	Euclidean distance between MDS values	10 MDS runs	Mann-Whitney U, bonferroni correction for n=2	U = 11, p = 0.007, effect-size (r) = 0.66
Fig. 2.7j	CS+/CS- vs CS1+/CS2+, odor period, Late session (vCA1)	Euclidean distance between MDS values	10 MDS runs	Mann-Whitney U, bonferroni correction for n=2	U = 93, p = 0.002, effect-size (r) = 0.72
Fig. 2.7j	CS+/CS- vs CS3-/CS4-, odor period, Late session (vCA1)	Euclidean distance between MDS values	10 MDS runs	Mann-Whitney U, bonferroni correction for n=2	U = 100, p < 0.001, effect-size (r) = 0.85

Figure	Variable	Unit of Comparison	n	Test	Results
Fig. 2.7j	CS1+/CS2+ vs CS3-/CS4-, odor period, Late session (vCA1)	Euclidean distance between MDS values	10 MDS runs	Mann-Whitney U, bonferroni correction for n=2	U = 100, p < 0.001, effect-size (r) = 0.85
Fig. 2.7j	CS+/CS- vs CS1+/CS2+, odor period, Pre session (dCA1)	Euclidean distance between MDS values	10 MDS runs	Mann-Whitney U, bonferroni correction for n=2	U = 98, p < 0.001, effect-size (r) = 0.81
Fig. 2.7j	CS+/CS- vs CS3-/CS4-, odor period, Pre session (dCA1)	Euclidean distance between MDS values	10 MDS runs	Mann-Whitney U, bonferroni correction for n=2	U = 100, p < 0.001, effect-size (r) = 0.85
Fig. 2.7j	CS1+/CS2+ vs CS3-/CS4-, odor period, Pre session (dCA1)	Euclidean distance between MDS values	10 MDS runs	Mann-Whitney U, bonferroni correction for n=2	U = 74, p = 0.15, effectsize (r) = 0.41
Fig. 2.7j	CS+/CS- vs CS1+/CS2+, odor period, Late session (dCA1)	Euclidean distance between MDS values	10 MDS runs	Mann-Whitney U, bonferroni correction for n=2	U = 50, p = 1.0, effectsize (r) = 0.0
Fig. 2.7j	CS+/CS- vs CS3-/CS4-, odor period, Late session (dCA1)	Euclidean distance between MDS values	10 MDS runs	Mann-Whitney U, bonferroni correction for n=2	U = 25, p = 0.13, effectsize (r) = 0.42
Fig. 2.7j	CS1+/CS2+ vs CS3-/CS4-, odor period, Late session (dCA1)	Euclidean distance between MDS values	10 MDS runs	Mann-Whitney U, bonferroni correction for n=2	U = 26, p = 0.15, effectsize (r) = 0.41
Fig. 2.7j	CS+/CS- vs CS1+/CS2+, trace period, Pre session (vCA1)	Euclidean distance between MDS values	10 MDS runs	Mann-Whitney U, bonferroni correction for n=2	U = 58, p = 1.0, effectsize (r) = 0.13
Fig. 2.7j	CS+/CS- vs CS3-/CS4-, trace period, Pre session (vCA1)	Euclidean distance between MDS values	10 MDS runs	Mann-Whitney U, bonferroni correction for n=2	U = 43, p = 1.0, effectsize (r) = 0.12
Fig. 2.7j	CS1+/CS2+ vs CS3-/CS4-, trace period, Pre session (vCA1)	Euclidean distance between MDS values	10 MDS runs	Mann-Whitney U, bonferroni correction for n=2	U = 41, p = 0.94, effectsize (r) = 0.15
Fig. 2.7j	CS+/CS- vs CS1+/CS2+, trace period, Late session (vCA1)	Euclidean distance between MDS values	10 MDS runs	Mann-Whitney U, bonferroni correction for n=2	U = 100, p < 0.001., effect-size (r) = 0.85
Fig. 2.7j	CS+/CS- vs CS3-/CS4-, trace period, Late session (vCA1)	Euclidean distance between MDS values	10 MDS runs	Mann-Whitney U, bonferroni correction for n=2	U = 100, p < 0.001., effect-size (r) = 0.85
Fig. 2.7j	CS1+/CS2+ vs CS3-/CS4-, trace period, Late session (vCA1)	Euclidean distance between MDS values	10 MDS runs	Mann-Whitney U, bonferroni correction for n=2	U = 34, p = 0.48, effectsize (r) = 0.27
Fig. 2.7j	CS+/CS- vs CS1+/CS2+, trace period, Pre session (dCA1)	Euclidean distance between MDS values	10 MDS runs	Mann-Whitney U, bonferroni correction for n=2	U = 41, p = 1.0, effectsize (r) = 0.15
Fig. 2.7j	CS+/CS- vs CS3-/CS4-, trace period, Pre session (dCA1)	Euclidean distance between MDS values	10 MDS runs	Mann-Whitney U, bonferroni correction for n=2	U = 22, p = 0.08, effectsize (r) = 0.47
Fig. 2.7j	CS1+/CS2+ vs CS3-/CS4-, trace period, Pre session (dCA1)	Euclidean distance between MDS values	10 MDS runs	Mann-Whitney U, bonferroni correction for n=2	U = 27, p = 0.18, effectsize (r) = 0.39
Fig. 2.7j	CS+/CS- vs CS1+/CS2+, trace period, Late session (dCA1)	Euclidean distance between MDS values	10 MDS runs	Mann-Whitney U, bonferroni correction for n=2	U = 100, p < 0.001, effect-size (r) = 0.85
Fig. 2.7j	CS+/CS- vs CS3-/CS4-, trace period, Late session (dCA1)	Euclidean distance between MDS values	10 MDS runs	Mann-Whitney U, bonferroni correction for n=2	U = 100, p < 0.001, effect-size (r) = 0.85
Fig. 2.7j	CS1+/CS2+ vs CS3-/CS4-, trace period, Late session (dCA1)	Euclidean distance between MDS values	10 MDS runs	Mann-Whitney U, bonferroni correction for n=2	U = 21, p = 0.06, effectsize (r) = 0.49
Fig. 2.8b	mean lick rate (Hz)	Trial type (Rew vs Shock; Early session)	13 mice (10 vCA1 and 3 dCA1 mice)	Mann-Whitney U, Bonferroni correction for n=2	U = 133, p = 0.028, effect-size (r) = 0.49

Figure	Variable	Unit of Comparison	n	Test	Results
Fig. 2.8b	mean lick rate (Hz)	Trial type (Rew vs CS-; Early session)	13 mice (10 vCA1 and 3 dCA1 mice)	Mann-Whitney U, Bonferroni correction for n=2	U = 13, p < 0.001, effect-size (r) = 0.71
Fig. 2.8b	mean lick rate (Hz)	Trial type (Shock vs CS-; Early session)	13 mice (10 vCA1 and 3 dCA1 mice)	Mann-Whitney U, Bonferroni correction for n=2	U = 12.5, p < 0.001, effect-size (r) = 0.72
Fig. 2.8b	mean lick rate (Hz)	Trial type (Rew vs Shock; Late session)	13 mice (10 vCA1 and 3 dCA1 mice)	Mann-Whitney U, Bonferroni correction for n=2	U = 256, p = < 0.001, effect-size (r) = 1.7
Fig. 2.8b	mean lick rate (Hz)	Trial type (Rew vs CS-; Late session)	13 mice (10 vCA1 and 3 dCA1 mice)	Mann-Whitney U, Bonferroni correction for n=2	U = 0, p < 0.001, effectsize (r) = 0.85
Fig. 2.8b	mean lick rate (Hz)	Trial type (Shock vs CS-; Late session)	13 mice (10 vCA1 and 3 dCA1 mice)	Mann-Whitney U, Bonferroni correction for n=2	U = 0, p = 1, effect-size (r) = 0.56
Fig. 2.8c	CS+Rew Decoding Accuracy, Early vs Late, odor period (vCA1)	10 decoding iterations for each	n-matched pseudopopulation of 444 cells from 10 vCA1 mice	Fisher's Exact	p < 0.001, effect-size (odds ratio) = 0.23
Fig. 2.8c	CS+Shock Decoding Accuracy, Early vs Late, odor period (vCA1)	10 decoding iterations for each	n-matched pseudopopulation of 444 cells from 10 vCA1 mice	Fisher's Exact	p < 0.001, effect-size (odds ratio) = 0.24
Fig. 2.8c	CS- Decoding Accuracy, Early vs Late, odor period (vCA1)	10 decoding iterations for each	n-matched pseudopopulation of 444 cells from 10 vCA1 mice	Fisher's Exact	p = 0.14, effect-size (odds ratio) = 0.72
Fig. 2.8c	CS+Rew Decoding Accuracy, Early vs Late, trace period (vCA1)	10 decoding iterations for each	n-matched pseudopopulation of 444 cells from 10 vCA1 mice	Fisher's Exact	p < 0.001, effect-size (odds ratio) = 0.26
Fig. 2.8c	CS+Shock Decoding Accuracy, Early vs Late, trace period (vCA1)	10 decoding iterations for each	n-matched pseudopopulation of 444 cells from 10 vCA1 mice	Fisher's Exact	p < 0.001, effect-size (odds ratio) = 0.40
Fig. 2.8c	CS- Decoding Accuracy, Early vs Late, trace period (vCA1)	10 decoding iterations for each	n-matched pseudopopulation of 444 cells from 10 vCA1 mice	Fisher's Exact	p = 0.24, effect-size (odds ratio) = 0.76
Fig. 2.8c	CS+Rew Decoding Accuracy, Early vs Late, odor period (dCA1)	10 decoding iterations for each	n-matched pseudopopulation of 444 cells from 3 dCA1 mice	Fisher's Exact	p = 0.003, effect-size (odds ratio) = 0.18
Fig. 2.8c	CS+Shock Decoding Accuracy, Early vs Late, odor period (dCA1)	10 decoding iterations for each	n-matched pseudopopulation of 444 cells from 3 dCA1 mice	Fisher's Exact	p = 0.32, effect-size (odds ratio) = 0.63
Fig. 2.8c	CS- Decoding Accuracy, Early vs Late, odor period (dCA1)	10 decoding iterations for each	n-matched pseudopopulation of 444 cells from 3 dCA1 mice	Fisher's Exact	p = 0.73, effect-size (odds ratio) = 0.88
Fig. 2.8c	CS+Rew Decoding Accuracy, Early vs Late, trace period (dCA1)	10 decoding iterations for each	n-matched pseudopopulation of 444 cells from 3 dCA1 mice	Fisher's Exact	p < 0.001, effect-size (odds ratio) = 0.17
Fig. 2.8c	CS+Shock Decoding Accuracy, Early vs Late, trace period (dCA1)	10 decoding iterations for each	n-matched pseudopopulation of 444 cells from 3 dCA1 mice	Fisher's Exact	p = 0.003, effect-size (odds ratio) = 0.48
Fig. 2.8c	CS- Decoding Accuracy, Early vs Late, trace period (dCA1)	10 decoding iterations for each	n-matched pseudopopulation of 444 cells from 3 dCA1 mice	Fisher's Exact	p = 0.003, effect-size (odds ratio) = 0.52
Fig. 2.8e	mean lick rate (Hz)	Trial type (Rew vs Shock; Early Reversal session)	13 mice (10 vCA1 and 3 dCA1 mice)	Mann-Whitney U, Bonferroni correction for n=2	U = 82, p = 1, effect-size (r) = 0.02
Fig. 2.8e	mean lick rate (Hz)	Trial type (Rew vs CS-; Early Reversal session)	13 mice (10 vCA1 and 3 dCA1 mice)	Mann-Whitney U, Bonferroni correction for n=2	U = 21.5, p = 0.003, effect-size (r) = 0.62
Fig. 2.8e	mean lick rate (Hz)	Trial type (Shock vs CS-; Early Reversal session)	13 mice (10 vCA1 and 3 dCA1 mice)	Mann-Whitney U, Bonferroni correction for n=2	U = 10, p < 0.001, effectsize (r) = 0.74

Figure	Variable	Unit of Comparison	n	Test	Results
Fig. 2.8e	mean lick rate (Hz)	Trial type (Rew vs Shock; Late Reversal session)	13 mice (10 vCA1 and 3 dCA1 mice)	Mann-Whitney U, Bonferroni correction for n=2	U = 255, p = < 0.001, effect-size (r) = 1.7
Fig. 2.8e	mean lick rate (Hz)	Trial type (Rew vs CS-; Late Reversal session)	13 mice (10 vCA1 and 3 dCA1 mice)	Mann-Whitney U, Bonferroni correction for n=2	U = 3, p < 0.001, effectsize (r) = 0.81
Fig. 2.8e	mean lick rate (Hz)	Trial type (Shock vs CS-; Late Reversal session)	13 mice (10 vCA1 and 3 dCA1 mice)	Mann-Whitney U, Bonferroni correction for n=2	U = 110, p = 1, effectsize (r) = 0.26
Fig. 2.8f	CS+Rew/baseline vs CS+Shock/baseline decoding accuracies, Late Reversal, odor period (vCA1)	10 decoding iterations for each	n-matched pseudopopulation of 444 cells from 10 vCA1 mice	Mann-Whitney U, Bonferroni correction for n=2	U = 100, p < 0.001, effect-size (r) = 0.85
Fig. 2.8f	CS+Rew/baseline vs CS-/baseline decoding accuracies, Late Reversal, odor period (vCA1)	10 decoding iterations for each	n-matched pseudopopulation of 444 cells from 10 vCA1 mice	Mann-Whitney U, Bonferroni correction for n=2	U = 100, p < 0.001, effect-size (r) = 0.85
Fig. 2.8f	CS+Shock/baseline vs CS-/baseline decoding accuracies, Late Reversal, odor period (vCA1)	10 decoding iterations for each	n-matched pseudopopulation of 444 cells from 10 vCA1 mice	Mann-Whitney U, Bonferroni correction for n=2	U = 97, p < 0.001, effect-size (r) = 0.79
Fig. 2.8f	CS+Rew/baseline vs CS+Shock/baseline decoding accuracies, Late Reversal, odor period (dCA1)	10 decoding iterations for each	n-matched pseudopopulation of 444 cells from 3 dCA1 mice	Mann-Whitney U, Bonferroni correction for n=2	U = 17.5, p = 0.03, effect-size (r) = 0.55
Fig. 2.8f	CS+Rew/baseline vs CS-/baseline decoding accuracies, Late Reversal, odor period (dCA1)	10 decoding iterations for each	n-matched pseudopopulation of 444 cells from 3 dCA1 mice	Mann-Whitney U, Bonferroni correction for n=2	U = 27.5, p = 0.19, effect-size (r) = 0.38
Fig. 2.8f	CS+Shock/baseline vs CS-/baseline decoding accuracies, Late Reversal, odor period (dCA1)	10 decoding iterations for each	n-matched pseudopopulation of 444 cells from 3 dCA1 mice	Mann-Whitney U, Bonferroni correction for n=2	U = 55.5, p = 1, effectsize (r) = 0.09
Fig. 2.8f	CS+Rew/baseline vs CS+Shock/baseline decoding accuracies, Late Reversal, trace period (vCA1)	10 decoding iterations for each	n-matched pseudopopulation of 444 cells from 10 vCA1 mice	Mann-Whitney U, Bonferroni correction for n=2	U = 100, p < 0.001, effect-size (r) = 0.85
Fig. 2.8f	CS+Rew/baseline vs CS-/baseline decoding accuracies, Late Reversal, trace period (vCA1)	10 decoding iterations for each	n-matched pseudopopulation of 444 cells from 10 vCA1 mice	Mann-Whitney U, Bonferroni correction for n=2	U = 100, p < 0.001, effect-size (r) = 0.85
Fig. 2.8f	CS+Shock/baseline vs CS-/baseline decoding accuracies, Late Reversal, trace period (vCA1)	10 decoding iterations for each	n-matched pseudopopulation of 444 cells from 10 vCA1 mice	Mann-Whitney U, Bonferroni correction for n=2	U = 22.5, p = 0.08, effect-size (r) = 0.46
Fig. 2.8f	CS+Rew/baseline vs CS+Shock/baseline decoding accuracies, Late Reversal, trace period (dCA1)	10 decoding iterations for each	n-matched pseudopopulation of 444 cells from 3 dCA1 mice	Mann-Whitney U, Bonferroni correction for n=2	U = 100, p < 0.001, effect-size (r) = 0.85
Fig. 2.8f	CS+Rew/baseline vs CS-/baseline decoding accuracies, Late Reversal, trace period (dCA1)	10 decoding iterations for each	n-matched pseudopopulation of 444 cells from 3 dCA1 mice	Mann-Whitney U, Bonferroni correction for n=2	U = 100, p < 0.001, effect-size (r) = 0.85
Fig. 2.8f	CS+Shock/baseline vs CS-/baseline decoding accuracies, Late Reversal, trace period (dCA1)	10 decoding iterations for each	n-matched pseudopopulation of 444 cells from 3 dCA1 mice	Mann-Whitney U, Bonferroni correction for n=2	U = 23.5, p = 0.095, effect-size (r) = 0.45
Fig. 2.8g	Odor A/baseline vs odor B/baseline decoding accuracies across reversal training, odor period (vCA1)	10 decoding iterations for each	n-matched pseudopopulation of 281 cells from 10 vCA1 mice	Mann-Whitney U, Bonferroni correction for n=2	U = 42.5, p = 1, effectsize (r) = 0.13
Fig. 2.8g	Odor A/baseline vs odor C/baseline decoding accuracies across reversal training, odor period (vCA1)	10 decoding iterations for each	n-matched pseudopopulation of 281 cells from 10 vCA1 mice	Mann-Whitney U, Bonferroni correction for n=2	U = 0, p < 0.001, effectsize (r) = 0.85
Fig. 2.8g	Odor B/baseline vs odor C/baseline decoding accuracies across reversal training, odor period (vCA1)	10 decoding iterations for each	n-matched pseudopopulation of 281 cells from 10 vCA1 mice	Mann-Whitney U, Bonferroni correction for n=2	U = 0, p < 0.001, effectsize (r) = 0.85
Fig. 2.8g	Odor A/baseline vs odor B/baseline decoding accuracies across reversal training, odor period (dCA1)	10 decoding iterations for each	n-matched pseudopopulation of 281 cells from 3 dCA1 mice	Mann-Whitney U, Bonferroni correction for n=2	U = 36, p = 0.61, effectsize (r) = 0.24

Figure	Variable	Unit of Comparison	n	Test	Results
Fig. 2.8g	Odor A/baseline vs odor C/baseline decoding accuracies across reversal training, odor period (dCA1)	10 decoding iterations for each	n-matched pseudopopulation of 281 cells from 3 dCA1 mice	Mann-Whitney U, Bonferroni correction for n=2	U = 39.5, p = .9, effectsize (r) = 0.18
Fig. 2.8g	Odor B/baseline vs odor C/baseline decoding accuracies across reversal training, odor period (dCA1)	10 decoding iterations for each	n-matched pseudopopulation of 281 cells from 3 dCA1 mice	Mann-Whitney U, Bonferroni correction for n=2	U = 28, p = .21, effectsize (r) = 0.37
Fig. 2.8h	CS+Rew/baseline vs CS+Shock/baseline decoding accuracies across reversal training, trace period (vCA1)	10 decoding iterations for each	n-matched pseudopopulation of 281 cells from 10 vCA1 mice	Mann-Whitney U, Bonferroni correction for n=2	U = 100, p < 0.001, effect-size (r) = 0.85
Fig. 2.8h	CS+Rew/baseline vs CS-/baseline decoding accuracies across reversal training, trace period (vCA1)	10 decoding iterations for each	n-matched pseudopopulation of 281 cells from 10 vCA1 mice	Mann-Whitney U, Bonferroni correction for n=2	U = 0, p < 0.001, effectsize (r) = 0.85
Fig. 2.8h	CS+Shock/baseline vs CS-/baseline decoding accuracies across reversal training, trace period (vCA1)	10 decoding iterations for each	n-matched pseudopopulation of 281 cells from 10 vCA1 mice	Mann-Whitney U, Bonferroni correction for n=2	U = 55, p = 1, effect-size (r) = 0.08
Fig. 2.8h	CS+Rew/baseline vs CS+Shock/baseline decoding accuracies across reversal training, trace period (dCA1)	10 decoding iterations for each	n-matched pseudopopulation of 281 cells from 3 dCA1 mice	Mann-Whitney U, Bonferroni correction for n=2	U = 100, p < 0.001, effect-size (r) = 0.85
Fig. 2.8h	CS+Rew/baseline vs CS-/baseline decoding accuracies across reversal training, trace period (dCA1)	10 decoding iterations for each	n-matched pseudopopulation of 281 cells from 3 dCA1 mice	Mann-Whitney U, Bonferroni correction for n=2	U = 0, p < 0.001, effectsize (r) = 0.85
Fig. 2.8h	CS+Shock/baseline vs CS-/baseline decoding accuracies across reversal training, trace period (dCA1)	10 decoding iterations for each	n-matched pseudopopulation of 281 cells from 3 dCA1 mice	Mann-Whitney U, Bonferroni correction for n=2	U = 49, p = 1, effect-size (r) = 0.17
Fig. 2.9c	propotion of reward trials with suprathreshold running	Early vs. Late sessions	12 mice (8 vCA1, 4 dCA1)	Mann-Whitney U	U = 36, p = 0.004, effect-size (r) = 0.2
Fig. 2.9c	propotion of CS- trials with suprathreshold running	Early vs. Late sessions	12 mice (8 vCA1, 4 dCA1)	Mann-Whitney U	U = 43.5, p = 0.01, effect-size (r) = 0.18
Fig. 2.9c	propotion of shock trials with suprathreshold running	Early vs. Late sessions	12 mice (8 vCA1, 4 dCA1)	Mann-Whitney U	U = 0, p < 0.001, effectsize (r) = 0.32
Fig. 2.9d	mean lick rate (Hz)	Trial type (Rew vs Shock)	12 mice (8 vCA1, 4 dCA1)	Mann-Whitney U	U = 139.5, p < 0.001, effect-size (r) = 0.8
Fig. 2.9d	mean lick rate (Hz)	Trial type (Rew vs CS-)	12 mice (8 vCA1, 4 dCA1)	Mann-Whitney U	U = 138, p < 0.001, effect-size (r) = 0.78
Fig. 2.9d	mean lick rate (Hz)	Trial type (CS- vs Shock)	12 mice (8 vCA1, 4 dCA1)	Mann-Whitney U	U = 71.5, p = 1.0, effectsize (r) = 0.006
Fig. 2.9e	CS+Rew/baseline vs CS+Shock/baseline decoding accuracies, Late, odor period (vCA1)	10 decoding iterations for each	n-matched pseudopopulation of 340 cells from 8 vCA1 mice	Mann-Whitney U, Bonferroni correction for n=2	U = 44.5, p = 1.0, effectsize (r) = 0.09
Fig. 2.9e	CS+Rew/baseline vs CS-/baseline decoding accuracies, Late, odor period (vCA1)	10 decoding iterations for each	n-matched pseudopopulation of 340 cells from 8 vCA1 mice	Mann-Whitney U, Bonferroni correction for n=2	U = 98, p < 0.001, effect-size (r) = 0.81
Fig. 2.9e	CS+Shock/baseline vs CS-/baseline decoding accuracies, Late, odor period (vCA1)	10 decoding iterations for each	n-matched pseudopopulation of 340 cells from 8 vCA1 mice	Mann-Whitney U, Bonferroni correction for n=2	U = 100, p < 0.001, effect-size (r) = 0.85
Fig. 2.9e	CS+Rew/baseline vs CS+Shock/baseline decoding accuracies, Late, odor period (dCA1)	10 decoding iterations for each	n-matched pseudopopulation of 340 cells from 4 dCA1 mice	Mann-Whitney U, Bonferroni correction for n=2	U = 20.5, p = 0.049, effect-size (r) = 0.5
Fig. 2.9e	CS+Rew/baseline vs CS-/baseline decoding accuracies, Late, odor period (dCA1)	10 decoding iterations for each	n-matched pseudopopulation of 340 cells from 4 dCA1 mice	Mann-Whitney U, Bonferroni correction for n=2	U = 36.5, p = 0.64, effect-size (r) = 0.23
Fig. 2.9e	CS+Shock/baseline vs CS-/baseline decoding accuracies, Late, odor period (dCA1)	10 decoding iterations for each	n-matched pseudopopulation of 340 cells from 4 dCA1 mice	Mann-Whitney U, Bonferroni correction for n=2	U = 65.5, p = 0.47, effect-size (r) = 0.26

Figure	Variable	Unit of Comparison	n	Test	Results
Fig. 2.9e	CS+Rew/baseline vs CS+Shock/baseline decoding accuracies, Late, trace period (vCA1)	10 decoding iterations for each	n-matched pseudopopulation of 340 cells from 8 vCA1 mice	Mann-Whitney U, Bonferroni correction for n=2	U = 100, p < 0.001, effect-size (r) = 0.85
Fig. 2.9e	CS+Rew/baseline vs CS-/baseline decoding accuracies, Late, trace period (vCA1)	10 decoding iterations for each	n-matched pseudopopulation of 340 cells from 8 vCA1 mice	Mann-Whitney U, Bonferroni correction for n=2	U = 100, p < 0.001, effect-size (r) = 0.85
Fig. 2.9e	CS+Shock/baseline vs CS-/baseline decoding accuracies, Late, trace period (vCA1)	10 decoding iterations for each	n-matched pseudopopulation of 340 cells from 8 vCA1 mice	Mann-Whitney U, Bonferroni correction for n=2	U = 60, p = 0.94, effectsize (r) = 0.17
Fig. 2.9e	CS+Rew/baseline vs CS+Shock/baseline decoding accuracies, Late, trace period (dCA1)	10 decoding iterations for each	n-matched pseudopopulation of 340 cells from 4 dCA1 mice	Mann-Whitney U, Bonferroni correction for n=2	U = 40, p = 0.92, effectsize (r) = 0.17
Fig. 2.9e	CS+Rew/baseline vs CS-/baseline decoding accuracies, Late, trace period (dCA1)	10 decoding iterations for each	n-matched pseudopopulation of 340 cells from 4 dCA1 mice	Mann-Whitney U, Bonferroni correction for n=2	U = 76, p = 0.1, effectsize (r) = 0.44
Fig. 2.9e	CS+Shock/baseline vs CS-/baseline decoding accuracies, Late, trace period (dCA1)	10 decoding iterations for each	n-matched pseudopopulation of 340 cells from 4 dCA1 mice	Mann-Whitney U, Bonferroni correction for n=2	U = 81.5, p = 0.035, effect-size (r) = 0.53
S2c	odor1/odor2 decoding accuracy, vCA1 vs dCA1 (0.5 sec time bins)	10 decoding iterations for each region	n-matched pseudopopulation of 454 cells from 11 vCA1 and 5 dCA1 mice	Mann-Whitney U	colored-coded bar above graph shows time bins where p < 0.01
S2d	odor1/odor2 decoding accuracy, vCA1 vs dCA1 (2 sec time bins)	10 decoding iterations for each region	n-matched pseudopopulation of 454 cells from 11 vCA1 and 5 dCA1 mice	Mann-Whitney U	colored-coded bar above graph shows time bins where p < 0.01
S2e	decoding accuracy vs baseline	10 decoding iterations each	n-matched pseudopopulation of 454 cells from 11 vCA1 and 5 dCA1 mice	One-way ANOVA	
				region	F = 107, p < 0.001, effect size (ETA^2) = .70
				odor	F = .47, p = 0.5, effect size (ETA^2) = .003
				region*odor	F = 9.92, p = 0.003, effect size (ETA^2) = .065
S2e	vCA1 vs dCA1 odor1/baseline decoding accuracies	10 decoding iterations for each region	n-matched pseudopopulation of 454 cells from 11 vCA1 and 5 dCA1 mice	Mann-Whitney U	U = 0, p = 0.00017, effect-size (r) = 0.85
S2e	vCA1 vs dCA1 odor2/baseline decoding accuracies	10 decoding iterations for each region	n-matched pseudopopulation of 454 cells from 11 vCA1 and 5 dCA1 mice	Mann-Whitney U	U = 12.0, p = 0.0046, effect-size (r) = 0.64
S3c	Early vs Late linear regression of calcium activity and lick rate	Early vs Late sessions	10 vCA1 mice	T-test	t = 1.86, p = 0.079, effect-size (Cohen's d) = 0.88
S3c	Early vs Late linear regression of calcium activity and lick rate	Early vs Late sessions	5 dCA1 mice	T-test	t = 1.51 p = 0.17, effectsize (Cohen's d) = 1.07
S3d	CS+ responsive cells during odor period, Early vs Late (vCA1)	total combined cells from 11 vCA1 mice	see figure for exact cell numbers	Fisher's Exact	p = 0.003, effect-size (odds ratio) = 2.02
S3d	CS- responsive cells during odor period, Early vs Late (vCA1)	total combined cells from 11 vCA1 mice	see figure for exact cell numbers	Fisher's Exact	p = 0.13, effect-size (odds ratio) = 0.6
S3d	CS+ responsive cells during trace period, Early vs Late (vCA1)	total combined cells from 11 vCA1 mice	see figure for exact cell numbers	Fisher's Exact	p < 0.001, effect-size (odds ratio) = 4.56
S3d	CS- responsive cells during trace period, Early vs Late (vCA1)	total combined cells from 11 vCA1 mice	see figure for exact cell numbers	Fisher's Exact	p = 0.055, effect-size (odds ratio) = 6.96

Figure	Variable	Unit of Comparison	n	Test	Results
S3d	CS+ responsive cells during odor period, Early vs Late (dCA1)	total combined cells from 4 dCA1 mice	see figure for exact cell numbers	Fisher's Exact	p < 0.001, effect-size (odds ratio) = 2.7
S3d	CS- responsive cells during odor period, Early vs Late (dCA1)	total combined cells from 4 dCA1 mice	see figure for exact cell numbers	Fisher's Exact	p = 0.38, effect-size (odds ratio) = 0.79
S3d	CS+ responsive cells during trace period, Early vs Late (dCA1)	total combined cells from 4 dCA1 mice	see figure for exact cell numbers	Fisher's Exact	p < 0.001, effect-size (odds ratio) = 8.24
S3d	CS- responsive cells during trace period, Early vs Late (dCA1)	total combined cells from 4 dCA1 mice	see figure for exact cell numbers	Fisher's Exact	p = 0.004, effect-size (odds ratio) = 11.3
S4c	CS+/baseline (upper) or CS-/baseline (lower) decoding accuracies, Pre vs Late sessions	10 decoding iterations for each	n-matched pseudopopulation of 454 cells from 11 vCA1 or 5 dCA1 mice	Mann-Whitney U	color-coded bars above graph show time bins where p < 0.01
S4d	Early vs Late, odor period (vCA1)	Euclidean distance between CS+ and CS-MDS values	10 MDS runs	Mann-Whitney U	U = 2, p < 0.001, effectsize (r) = 0.81
S4d	Early vs Late, trace period (vCA1)	Euclidean distance between CS+ and CS-MDS values	10 MDS runs	Mann-Whitney U	U = 3, p < 0.001, effectsize (r) = 0.79
S4d	Early vs Late, odor period (dCA1)	Euclidean distance between CS+ and CS-MDS values	10 MDS runs	Mann-Whitney U	U = 25, p = 0.064, effect-size (r) = 0.42
S4d	Early vs Late, trace period (dCA1)	Euclidean distance between CS+ and CS-MDS values	10 MDS runs	Mann-Whitney U	U = 0, p < 0.001, effectsize (r) = 0.85
S4f	CS+/CS- decoding accuracy, odor period	pre vs post 'aha' point	11 vCA1 mice	Mann-Whitney U	U = 21, p = .031, effectsize (r) = 0.49
S4f	CS+/CS- decoding accuracy, trace period	pre vs post 'aha' point	11 vCA1 mice	Mann-Whitney U	U = 0, p < .001, effectsize (r) = 0.84
S4f	CS+/CS- decoding accuracy, odor period	pre vs post 'aha' point	4 dCA1 mice	Mann-Whitney U	U = 27, p = 0.089., effect-size (r) = 0.39
S4f	CS+/CS- decoding accuracy, trace period	pre vs post 'aha' point	4 dCA1 mice	Mann-Whitney U	U = 19, p = .021., effect-size (r) = 0.52.
S5C	CS+/baseline decoding accuracies during tone period, Early vs Late session (vCA1)	10 decoding iterations for each session	n-matched pseudopopulation of 537 cells from 4 vCA1 mice	Mann-Whitney U	U = 24, p = 0.054, effect-size (r) = 0.44
S5C	CS+/baseline decoding accuracies during tone period, Early vs Late session (dCA1)	10 decoding iterations for each session	n-matched pseudopopulation of 537 cells from 2 dCA1 mice	Mann-Whitney U	U = 40, p = 0.47, effectsize (r) = 0.17
S5D	CS-/baseline decoding accuracies during tone period, Early vs Late session (vCA1)	10 decoding iterations for each session	n-matched pseudopopulation of 537 cells from 4 vCA1 mice	Mann-Whitney U	U = 47, p = 0.85, effectsize (r) = 0.05
S5D	CS-/baseline decoding accuracies during tone period, Early vs Late session (dCA1)	10 decoding iterations for each session	n-matched pseudopopulation of 537 cells from 2 dCA1 mice	Mann-Whitney U	U = 29.5, p = 0.13, effect-size (r) = 0.35
S5E	mean lick rate (Hz)	Trial type (Early session)	3 vCA1 mice (non-learners only)	Mann-Whitney U	U = 4, p = 1, effect-size (r) = 0.0
S5E	mean lick rate (Hz)	Trial type (Late session)	3 vCA1 mice (non-learners only)	Mann-Whitney U	U = 2, p = 0.38, effectsize (r) = 0.37
S5F	CS+/CS- decoding accuracy. Early vs Late	10 decoding iterations for each session	n-matched pseudopopulation of 71 cells from 4 vCA1 (learner), 3 vCA1 (nonlearner), or 2 dCA1 (learner) mice	Mann-Whitney U	color-coded bars above graph show time bins where p < 0.01

Figure	Variable	Unit of Comparison	n	Test	Results
S5G	CS+/CS- decoding accuracy, tone period, vCA1 nonlearners vs vCA1 learners (Early)	10 decoding iterations for each	n-matched pseudopopulation of 71 cells from 4 vCA1 (learner), 3 vCA1 (nonlearner), or 2 dCA1 (learner) mice	Mann-Whitney U, Bonferroni correction for n=2	U = 30, p = 0.28, effectsize (r) = 0.34
S5G	CS+/CS- decoding accuracy, tone period, vCA1 nonlearners vs dCA1 learners (Early)	10 decoding iterations for each	n-matched pseudopopulation of 71 cells from 4 vCA1 (learner), 3 vCA1 (nonlearner), or 2 dCA1 (learner) mice	Mann-Whitney U, Bonferroni correction for n=2	U = 70, p = 0.27, effectsize (r) = 0.34
S5G	CS+/CS- decoding accuracy, tone period, vCA1 learners vs dCA1 learners (Early)	10 decoding iterations for each	n-matched pseudopopulation of 71 cells from 4 vCA1 (learner), 3 vCA1 (nonlearner), or 2 dCA1 (learner) mice	Mann-Whitney U, Bonferroni correction for n=2	U = 83, p = 0.028, effect-size (r) = 0.56
S5G	CS+/CS- decoding accuracy, tone period, vCA1 nonlearners vs vCA1 learners (Late)	10 decoding iterations for each	n-matched pseudopopulation of 71 cells from 4 vCA1 (learner), 3 vCA1 (nonlearner), or 2 dCA1 (learner) mice	Mann-Whitney U, Bonferroni correction for n=2	U = 3, p < 0.001, effectsize (r) = 0.79
S5G	CS+/CS- decoding accuracy, tone period, vCA1 nonlearners vs dCA1 learners (Late)	10 decoding iterations for each	n-matched pseudopopulation of 71 cells from 4 vCA1 (learner), 3 vCA1 (nonlearner), or 2 dCA1 (learner) mice	Mann-Whitney U, Bonferroni correction for n=2	U = 29.5, p = 0.26, effect-size (r) = 0.35
S5G	CS+/CS- decoding accuracy, tone period, vCA1 learners vs dCA1 learners (Late)	10 decoding iterations for each	n-matched pseudopopulation of 71 cells from 4 vCA1 (learner), 3 vCA1 (nonlearner), or 2 dCA1 (learner) mice	Mann-Whitney U, Bonferroni correction for n=2	U = 92, p = 0.003, effect-size (r) = 0.71
S5G	CS+/CS- decoding accuracy, trace period, vCA1 nonlearners vs vCA1 learners (Early)	10 decoding iterations for each	n-matched pseudopopulation of 71 cells from 4 vCA1 (learner), 3 vCA1 (nonlearner), or 2 dCA1 (learner) mice	Mann-Whitney U, Bonferroni correction for n=2	U = 58.5, p = 0.1, effectsize (r) = 0.14
S5G	CS+/CS- decoding accuracy, trace period, vCA1 nonlearners vs dCA1 learners (Early)	10 decoding iterations for each	n-matched pseudopopulation of 71 cells from 4 vCA1 (learner), 3 vCA1 (nonlearner), or 2 dCA1 (learner) mice	Mann-Whitney U, Bonferroni correction for n=2	U = 36.5, p = 0.65, effect-size (r) = 0.23
Fig. S3G	CS+/CS- decoding accuracy, trace period, vCA1 learners vs dCA1 learners (Early)	10 decoding iterations for each	n-matched pseudopopulation of 71 cells from 4 vCA1 (learner), 3 vCA1 (nonlearner), or 2 dCA1 (learner) mice	Mann-Whitney U, Bonferroni correction for n=2	U = 30.5, p = 0.3, effectsize (r) = 0.33
S5G	CS+/CS- decoding accuracy, trace period, vCA1 nonlearners vs vCA1 learners (Late)	10 decoding iterations for each	n-matched pseudopopulation of 71 cells from 4 vCA1 (learner), 3 vCA1 (nonlearner), or 2 dCA1 (learner) mice	Mann-Whitney U, Bonferroni correction for n=2	U = 1, p < 0.001, effectsize (r) = 0.83
S5G	CS+/CS- decoding accuracy, trace period, vCA1 nonlearners vs dCA1 learners (Late)	10 decoding iterations for each	n-matched pseudopopulation of 71 cells from 4 vCA1 (learner), 3 vCA1 (nonlearner), or 2 dCA1 (learner) mice	Mann-Whitney U, Bonferroni correction for n=2	U = 11, p = 0.007, effect-size (r) = 0.66
S5G	CS+/CS- decoding accuracy, trace period, vCA1 learners vs dCA1 learners (Late)	10 decoding iterations for each	n-matched pseudopopulation of 71 cells from 4 vCA1 (learner), 3 vCA1 (nonlearner), or 2 dCA1 (learner) mice	Mann-Whitney U, Bonferroni correction for n=2	U = 83, p = 0.028, effect-size (r) = 0.56
S9g	Across-session Early/Late vs Late/Reacq trial type decoding accuracies during trace period (dCA1)	10 decoding iterations for each	n-matched pseudopopulation of 100 cells from 5 dCA1 mice	Mann-Whitney U	U = 10, p = 0.003, effect-size (r) = 0.68
S9h	Across-session Early/Late vs Late/Reacq CS+/CS- decoding accuracies during odor period (vCA1)	10 decoding iterations for each	n-matched pseudopopulation of 100 cells from 8 vCA1 mice	Mann-Whitney U	U = 0, p < 0.001, effectsize (r) = 0.85
S9h	Across-session Early/Late vs Late/Reacq CS+/CS- decoding accuracies during odor period (dCA1)	10 decoding iterations for each	n-matched pseudopopulation of 100 cells from 5 dCA1 mice	Mann-Whitney U	U = 3, p < 0.001, effectsize (r) = 0.79
S9h	Across-session Early/Late vs Late/Reacq CS+/CS- decoding accuracies during trace period (vCA1)	10 decoding iterations for each	n-matched pseudopopulation of 100 cells from 8 vCA1 mice	Mann-Whitney U	U = 6, p = 0.001, effectsize (r) = 0.74

Figure	Variable	Unit of Comparison	n	Test	Results
S9h	Across-session Early/Late vs Late/Reacq CS+/CS- decoding accuracies during trace period (dCA1)	10 decoding iterations for each	n-matched pseudopopulation of 100 cells from 5 dCA1 mice	Mann-Whitney U	U = 0, p < 0.001, effectsize (r) = 0.85
S10b	CS+Shock/CS- decoding accuracy, odor period, Early vs Late (vCA1)	10 decoding iterations for each session	n-matched pseudopopulation of 444 cells from 10 vCA1 mice	Mann-Whitney U	U = 0, p < 0.001, effectsize (r) = 0.85
S10b	CS+Shock/CS- decoding accuracy, odor period, Early vs Late (dCA1)	10 decoding iterations for each session	n-matched pseudopopulation of 444 cells from 3 dCA1 mice	Mann-Whitney U	U = 49.5, p = 1, effectsize (r) = 0.008
S10b	CS+Shock/CS- decoding accuracy, trace period, Early vs Late (vCA1)	10 decoding iterations for each session	n-matched pseudopopulation of 444 cells from 10 vCA1 mice	Mann-Whitney U	U = 9, p = 0.002, effectsize (r) = 0.69
S10b	CS+Shock/CS- decoding accuracy, trace period, Early vs Late (dCA1)	10 decoding iterations for each session	n-matched pseudopopulation of 444 cells from 3 dCA1 mice	Mann-Whitney U	U = 12, p = 0.005, effect-size (r) = 0.64
S10c	CS+Rew/CS- decoding accuracy, odor period, Early vs Late (vCA1)	10 decoding iterations for each session	n-matched pseudopopulation of 444 cells from 10 vCA1 mice	Mann-Whitney U	U = 0, p < 0.001, effectsize (r) = 0.85
S10c	CS+Rew/CS- decoding accuracy, odor period, Early vs Late (dCA1)	10 decoding iterations for each session	n-matched pseudopopulation of 444 cells from 3 dCA1 mice	Mann-Whitney U	U = 0, p < 0.001, effectsize (r) = 0.77
S10c	CS+Rew/CS- decoding accuracy, trace period, Early vs Late (vCA1)	10 decoding iterations for each session	n-matched pseudopopulation of 444 cells from 10 vCA1 mice	Mann-Whitney U	U = 11, p = 0.004, effect-size (r) = 0.66
S10c	CS+Rew/CS- decoding accuracy, trace period, Early vs Late (dCA1)	10 decoding iterations for each session	n-matched pseudopopulation of 444 cells from 3 dCA1 mice	Mann-Whitney U	U = 0, p < 0.001, effectsize (r) = 0.85
S10d,e	trial type decoding accuracy, odor period, Late session	10 decoding iterations each	n-matched pseudopopulation of 444 cells from 10 vCA1 and 3 dCA1 mice	One-way ANOVA	
				region	F = 47.7, p < 0.001, effect size (ETA^2) = .24
				odor	F = 33.8, p < 0.001, effect size (ETA^2) = .34
				region*odor	F = 14.6, p < 0.001, effect size (ETA^2) = .15
S10d,e	trial type decoding accuracy, trace period, Late session	10 decoding iterations each	n-matched pseudopopulation of 444 cells from 10 vCA1 and 3 dCA1 mice	One-way ANOVA	
				region	F = 2.5, p = 0.12, effect size (ETA^2) = .02
				odor	F = 28.4, p < 0.001, effect size (ETA^2) = .52
				region*odor	F = .94, p = 0.4, effect size (ETA^2) = .03
S10i	Odor identity decoding accuracy across reversal learning (Late/Late Reversal), vCA1 vs dCA1	10 decoding iterations for each region	n-matched pseudopopulation of 281 cells from 10 vCA1 and 3 dCA1 mice	Mann-Whitney U	U = 41, p = 0.52, effectsize (r) = 0.15
S10j	Trial type decoding accuracy across reversal learning, trace period, Rew/CS- accuracy vs Sh/CS- accuracy (vCA1)	10 decoding iterations each	n-matched pseudopopulation of 281 cells from 10 vCA1 mice	Mann-Whitney U	U = 100, p < 0.001, effect-size (r) = 0.85
S10j	Trial type decoding accuracy across reversal learning, trace period, Rew/CS- accuracy vs Sh/CS- accuracy (dCA1)	10 decoding iterations each	n-matched pseudopopulation of 281 cells from 3 dCA1 mice	Mann-Whitney U	U = 100, p < 0.001, effect-size (r) = 0.85

Figure	Variable	Unit of Comparison	n	Test	Results
S11c	trial type decoding accuracy, odor period	10 decoding iterations each	n-matched pseudopopulation of 340 cells from 8 vCA1 and 4 dCA1 mice	One-way ANOVA	
				region	F = 1.6, p = 0.21, effect size (ETA^2) = .03
				odor	F = 0.95, p = 0.39, effect size (ETA^2) = .03
				region*odor	F = 1.44, p = 0.25, effect size (ETA^2) = .05
S11c	trial type decoding accuracy, trace period	10 decoding iterations each	n-matched pseudopopulation of 340 cells from 8 vCA1 and 4 dCA1 mice	One-way ANOVA	
				region	F = 5.16, p = 0.027, effect size (ETA^2) = .048
				odor	F = 15.3, p < 0.001, effect size (ETA^2) = .29
				region*odor	F = 9.4, p < 0.001, effect size (ETA^2) = .17
S11d	comparison of Rew vs CS- and Sh vs CS- decoding accuracies during odor period (vCA1; suprathreshold running trials only)	10 decoding iterations each	n-matched pseudopopulation of 340 cells from 8 vCA1 mice	Mann-Whitney U, Bonferroni correction for n=2	U = 10, p = 0.005, effect-size (r) = 0.68
S11d	comparison of Rew vs Sh and Sh vs CS- decoding accuracies during odor period (vCA1; suprathreshold running trials only)	10 decoding iterations each	n-matched pseudopopulation of 340 cells from 8 vCA1 mice	Mann-Whitney U, Bonferroni correction for n=2	U = 33.5, p = 0.34, effect-size (r) = 0.28
S11d	comparison of Rew vs CS- and Rew vs Sh decoding accuracies during odor period (vCA1; suprathreshold running trials only)	10 decoding iterations each	n-matched pseudopopulation of 340 cells from 8 vCA1 mice	Mann-Whitney U, Bonferroni correction for n=2	U = 90, p = 0.003, effect-size (r) = 0.68
S11d	comparison of Rew vs CS- and Sh vs CS- decoding accuracies during trace period (vCA1; suprathreshold running trials only)	10 decoding iterations each	n-matched pseudopopulation of 340 cells from 8 vCA1 mice	Mann-Whitney U, Bonferroni correction for n=2	U = 100, p < 0.001, effect-size (r) = 0.85
S11d	comparison of Rew vs Sh and Sh vs CS- decoding accuracies during trace period (vCA1; suprathreshold running trials only)	10 decoding iterations each	n-matched pseudopopulation of 340 cells from 8 vCA1 mice	Mann-Whitney U, Bonferroni correction for n=2	U = 0, p < 0.001, effect-size (r) = 0.85
S11d	comparison of Rew vs CS- and Rew vs Sh decoding accuracies during trace period (vCA1; suprathreshold running trials only)	10 decoding iterations each	n-matched pseudopopulation of 340 cells from 8 vCA1 mice	Mann-Whitney U, Bonferroni correction for n=2	U = 39.5, p = 0.56, effect-size (r) = 0.18
S11d	comparison of Rew vs CS- and Sh vs CS- decoding accuracies during odor period (dCA1; suprathreshold running trials only)	10 decoding iterations each	n-matched pseudopopulation of 340 cells from 4 dCA1 mice	Mann-Whitney U, Bonferroni correction for n=2	U = 27.5, p = 0.19, effect-size (r) = 0.38
S11d	comparison of Rew vs Sh and Sh vs CS- decoding accuracies during odor period (dCA1; suprathreshold running trials only)	10 decoding iterations each	n-matched pseudopopulation of 340 cells from 4 dCA1 mice	Mann-Whitney U, Bonferroni correction for n=2	U = 29, p = 0.23, effectsize (r) = 0.35
S11d	comparison of Rew vs CS- and Rew vs Sh decoding accuracies during odor period (dCA1; suprathreshold running trials only)	10 decoding iterations each	n-matched pseudopopulation of 340 cells from 4 dCA1 mice	Mann-Whitney U, Bonferroni correction for n=2	U = 83.5, p = 0.024, effect-size (r) = 0.57

Figure	Variable	Unit of Comparison	n	Test	Results
S11d	comparison of Rew vs CS- and Sh vs CS- decoding accuracies during trace period (dCA1; suprathreshold running trials only)	10 decoding iterations each	n-matched pseudopopulation of 340 cells from 4 dCA1 mice	Mann-Whitney U, Bonferroni correction for n=2	U = 74.5, p = 0.14, effect-size (r) = 0.41
S11d	comparison of Rew vs Sh and Sh vs CS- decoding accuracies during trace period (dCA1; suprathreshold running trials only)	10 decoding iterations each	n-matched pseudopopulation of 340 cells from 4 dCA1 mice	Mann-Whitney U, Bonferroni correction for n=2	U = 2, p < 0.001, effectsize (r) = 0.81
S11d	comparison of Rew vs CS- and Rew vs Sh decoding accuracies during trace period (dCA1; suprathreshold running trials only)	10 decoding iterations each	n-matched pseudopopulation of 340 cells from 4 dCA1 mice	Mann-Whitney U, Bonferroni correction for n=2	U = 78.5, p = 0.068, effect-size (r) = 0.48
S11e	Late session linear regression of calcium activity and running velocity (47.5 sec post odor onset)	imaging sessions	11 vCA1, 5 dCA1	T-test	t = 6.68, p < 0.001, effect-size (Cohen's d) = 3.38
S11f	Late session speed decoding accuracy, vCA1 vs dCA1	for each trial type, decoding accuracy for each 1 sec time bin spanning a 5 sec ITI period	15 each region (3 trial types x 5 time bins)	Mann-Whitney U	U = 75.5, p = 0.13, effect-size (r) = 0.43
S11f	Late session speed decoding accuracy vs chance (50%), vCA1	for each trial type, decoding accuracy for each 1 sec time bin spanning a 5 sec ITI period	15	Wilcoxon signedrank test	W = 16, p = 0.012, effect-size (r) = 0.57
S11f	Late session speed decoding accuracy vs chance (50%), dCA1	for each trial type, decoding accuracy for each 1 sec time bin spanning a 5 sec ITI period	15	Wilcoxon signedrank test	W = 2, p < 0.001, effectsize (r) = 0.81
N/A	total cells registered across sessions	dCA1 2odor Early-Late	337		
N/A	total cells registered across sessions	dCA1 2odor Late-Reacquisition	377		
N/A	total cells registered across sessions	vCA1 2odor Early-Late	241		
N/A	total cells registered across sessions	vCA1 2odor Late-Reacquisition	253		
N/A	total cells registered across sessions	dCA1 4odor Pre-Late	503		
N/A	total cells registered across sessions	dCA1 4odor Late-Post	503		
N/A	total cells registered across sessions	vCA1 4odor Pre-Late	104		
N/A	total cells registered across sessions	vCA1 4odor Late-Post	104		
N/A	total cells registered across sessions	dCA1 3odor Late-Reversal Late	281		
N/A	total cells registered across sessions	vCA1 3odor Late-Reversal Late	392		

Chapter 3: Conclusions

Using head-fixed 2-photon imaging in adult, behaving mice the results have demonstrated odor- and tone-evoked encoding in dCA1 and vCA1 in a range of associative learning tasks. This is similar to previous findings showing that before training stimuli and cues, particularly odors, are represented in dCA1 (Eichenbaum et al., 1987; Y. Li et al., 2017; Taxidis et al., 2020) is required for olfactory associative learning (Eichenbaum et al., 1987; Y. Li et al., 2017; Taxidis et al., 2020). In vCA1, responses to and population decoding of initial odor exposure was considerably inferior compared to dCA1, suggesting a continuous odor representation in dCA1 over this period. This extends the study of odor encoding in vCA1, which has primarily previously been studied in aversive behavior experiments, particularly avoidance behavior (Esclassan et al., 2009; McEchron et al., 1999; Mikulovic et al., 2018; Phillips & LeDoux, 1992; Wang et al., 2013; Zhang et al., 2014). When the 2 odors were associated with a sucrose reward or nothing, dCA1 continued to easily distinguish between the odors and the odor and baseline period, while vCA1 decoding only achieved significance above chance once the task was learned. Single cell, decoding by increasing cell count, and MDS analyses generally follow these results, but offer two further nuances: 1) Though the percentage of responsive cells was roughly the same for both areas during the early and late sessions sessions, the higher rate in enhanced CS+/CS- discriminability over the first 100 cells added to the decoder suggests either a subset of and/or on average, cells in dCA1 during early learning contains more information decoder-relevant information than in vCA1. 2) While high levels of odor decoding appear similar for dCA1 across early and late sessions, a significant increase in percentage of responding cells

and an increase, though not significant, in euclidean distance across early and late sessions suggest improvements in dCA1 odor encoding with learning that are not clearly present in the decoding results, likely due to a ceiling effect. These findings in dCA1 suggest a lack of encoding salience due to CS- encoding, while also changes in learning extend current literature which has shown remapping of dCA1 activity and selectivity with changing stimuli, particularly reward (Bast et al., 2009; Gauthier & Tank, 2018; Jarzebowski et al., 2022; Jin & Lee, 2021; Zaremba et al., 2017). Cumulatively, dCA1 and vCA1 can encode odor representations, though their ability to do so appears to be differentially dependent on learned association.

In contrast to the many differences in odor decoding, both areas decoding during the trace period similarly increased with learning. However, the Aha analysis suggests that 1) odor decoding in both areas increases before mice fully learn the task, and 2) vCA1 trace decoding increases sharply around the most rapid behavioral learning, which often occurred at the end of the early session or in the second session. This suggests a closer connection between trial-to-trial learning of the association and vCA1 encoding. Perhaps, this could be do a representation in dCA1 of increased licking behavior to reward in the 10 trials immediately before the aha point, though lick behavior does not closely correlate with activity in vCA1 or dCA1, suggesting that dCA1 rapidly learned trace decoding might represent something beyond licking behavior, possibly a prolonged odor representation. These findings extend previous work suggesting that vCA1 might have a larger role in working memory and trial-to-trial in specifically olfactory associative learning behavior than dCA1 (Hauser et al., 2020; Kesner et al., 2011; J. Li et al., 2022; Salimi et al., 2022). Surprisingly, the results show

mostly weak correlations between neural activity and licking, breathing or running behaviors in dCA1 and vCA1, particularly in vCA1, despite recent papers suggesting brain-wide signals for these types of behaviors, though other papers have also suggested a decorrelation between licking behavior and dCA1 activity (Ahmed et al., 2020; Musall et al., 2019; Stringer et al., 2019). Due to the correlation found by multiple labs between specific behavior actions in anxiety-based tasks and ventral hippocampal activity, the literature increasingly reflects the theory that ventral hippocampus drives approach behavior (Bryant & Barker, 2020; Jimenez et al., 2018; Padilla-Coreano et al., 2016; Parfitt et al., 2017; Pi et al., 2020; Sánchez-Bellot et al., 2022) Further studies should determine if other task evoked behaviors or measures of physiological correlates of salience, such as orofacial movements beyond licking, changes in pupil diameter, or heart rate, may contribute to correlate with hippocampal representations of associatively learned stimuli on a trial-by-trial basis.

The tone version of the experiment demonstrated that these learning-based differences in dCA1 and vCA1 are generally consistent across modality, with vCA1 tone encoding beginning significantly lower than in dCA1 and rising to parity with learning. Tone trace period decoding also was the same across experimental modalities in terms of relative change with learning. Notably, mice who failed to learn the tone task were unable to decode in odor or trace periods, suggesting decoding ability is related to behavioral learning specifically rather than accumulated task experience. This comparison between learners and non-learners emerged due to the considerably higher difficulty in tone association compared to the odor task, with mice taking up to 6 times longer to learn and some mice failing to learn the task even over 20 days. This difficulty

also likely explains the reduced decoding accuracies during the odor and trace periods, though it is interesting to note dCA1 does not discriminate between CS+/- tones in this task, while vCA1 can discriminate between the tones with learning. Perhaps this suggests a further difference between areas, that during more difficult discriminations, dCA1 will readily represent both stimuli before and after association learning, but vCA1 creates more specialized representations through different valence associations. The tone results offer some contrast to previous studies that have found tone encoding in dCA1 to be dependent on spatial features, whereas the results in a non-spatial task suggest dCA1 and vCA1 can encode tones, though more weakly than odorants, and vCA1 encoding is likely dependent on association to a rewarding or punishing stimulus (Itskov et al., 2012; Shan et al., 2016).

As the mice progressed through extinction and reinstatement sessions in the 2odor experiment, dCA1 encoding of odor remained stable, while vCA1 odor encoding varied with the presence of reward, further suggesting that vCA1 stimulus encoding is dependent on learned association with a value-based or behaviorally-relevant outcome. Additionally, both areas demonstrated stability in decoding across learned sessions with or without intervening extinction sessions, particularly during the trace period. This provides an interesting contrast to findings demonstrating vCA1 place cells remap readily, while vCA1 anxiety or avoidance behavior representations appear to be more stable (Chockanathan & Padmanabhan, 2021; Ciochi et al., 2015; Forro et al., 2022; Jimenez et al., 2018; Keinath et al., 2014; Poppenk et al., 2013). Results from the shock outcome experiments, both unavoidable and instrumentally controlled shock outcomes, provide further evidence for the importance of behavioral relevance for vCA1 cue and

outcome encoding. This suggests a range of vCA1 stable encoding tied to direct behavioral relevance of the outcome.

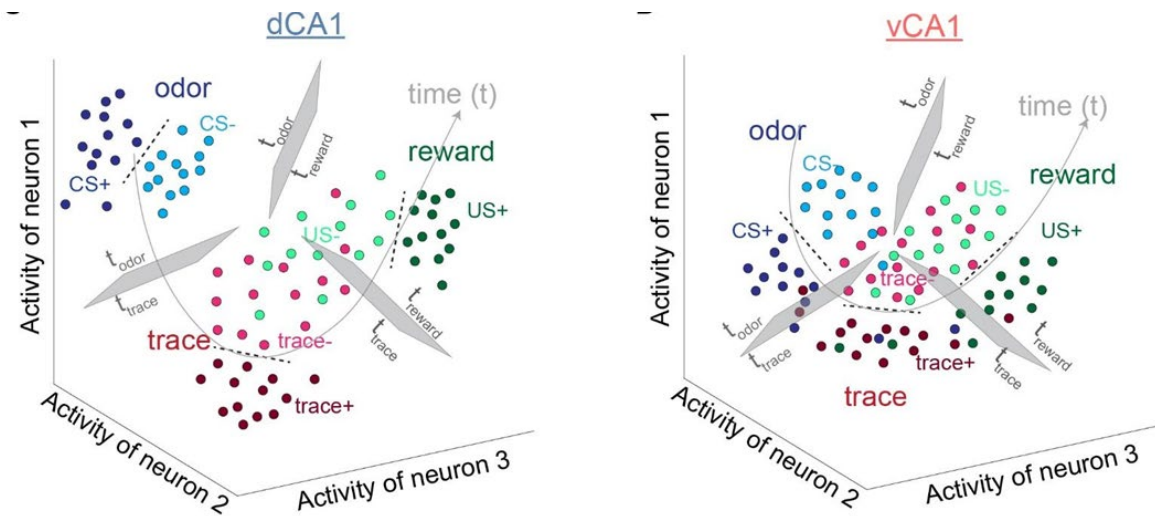
Previous studies have found odor encoding in vCA1, but the relationship between this single and other potentially encoded variables, such as associated outcome remain unclear, particularly at population level analyses (Eichenbaum et al., 1987; Kesner et al., 2011; Radvansky et al., 2021). The 4 odor paradigm allowed testing of this specific question, demonstrating through decoding the outcome that neuronal populations in vCA1 but not dCA1 also encode the outcome associated with an odor in addition to odor identity, allowing downstream regions to have a stable representation of odor identity and associated outcome. This increased informational density was also evident in the comparison between areas; vCA1, but not dCA1, represented outcome beyond the odor and trace periods, throughout the entire trial duration, even into the inter-trial interval. These stretched representations across odor, trace, and US periods may link discontinuous cue-reward events, providing a measure of value throughout a rewarded trial type (**Figure 3.1**). These two results, the mixing of outcome and cue information and trial-length outcome representation, extend results from many experiments, particularly in human literature that have found value-based representation in anterior hippocampus and generalizing encoding properties in ventral hippocampus (Bakkour et al., 2019; Knudsen & Wallis, 2021; Komorowski et al., 2013; Nguyen et al., 2018). There are many hypothesized uses for such a cohesive representation of task variables through the environment, including a (Çavdaroğlu et al., 2021).

While this study helps elucidate the potential roles for vCA1 and dCA1 population dynamics in associative learning, the underlying encoding mechanisms remain unclear.

Previous studies have found populations of dCA1 neurons coding for time in similar tasks via sequential ensemble firing (Taxidis et al., 2020). vCA1 could employ similar rotating ensembles of sequentially patterned activity to encode for outcome over trial-long epochs, but the observed stability of broadened vCA1 firing suggests rather that a dedicated subpopulation of cells might perform this role, though the low correlation between cue selectivity and decoder weight may complicate this interpretation of vCA1 network encoding properties (Jarzebowski et al., 2022). As has been identified studying spatial encoding in dCA1, it has also been found that neural oscillations likely organize vCA1 and dCA1 activity during olfactory associative learning and social behavior encoding, as well as playing a role in hippocampal development (Ahlbeck et al., 2018; Martin et al., 2007; Rao et al., 2019; Salimi et al., 2022; Schoepfer, 2020). Further study of the ensemble dynamics and neural oscillations underlying the observed differences across areas in associative learning encoding will enable targeted manipulation of these mechanisms and advance understanding of downstream processing.

Enhanced targeted manipulation of associative learning is particularly of interest in the context of hippocampal-associated post traumatic stress disorder (PTSD) (Kheirbek & Hen, 2011; Turner et al., 2022). Many studies have demonstrated correlational differences in human patients with PTSD with general hippocampal, as well as specifically anterior and posterior hippocampal, connectivity and activity (Chen & Etkin, 2013; Malivoire et al., 2018; Morey et al., 2016). Future work should examine the change in population encoding of associative learning in animal models of PTSD to determine how manipulating specifically dCA1 or vCA1 encoding can recover associative learning ability.

Figure 3.1 Summary Schematic



a-b. Summary schematic illustrating learned task representations in dCA1 (C) and vCA1 (D). Each dot represents a single-trial population activity vector during odor (blue), trace (red) or US (green) task epochs. In both dCA1 and vCA1, neural representations of CS+ and CS- trials are highly separable during each epoch. Task epochs are also generally separable from one another in both regions, particularly for CS+ trials and comparisons farther apart in time. In dCA1 there is less overlap of representations across epochs than there is in vCA1, owing in part to neural activity with greater temporal specialization in dCA1.

References for Chapter 3

- Ahlbeck, J., Song, L., Chini, M., Bitzenhofer, S. H., & Hanganu-Opatz, I. L. (2018). Glutamatergic drive along the septo-temporal axis of hippocampus boosts prelimbic oscillations in the neonatal mouse. *eLife*, 7. <https://doi.org/10.7554/eLife.33158>
- Ahmed, M. S., Priestley, J. B., Castro, A., Stefanini, F., Solis Canales, A. S., Balough, E. M., Lavoie, E., Mazzucato, L., Fusi, S., & Losonczy, A. (2020). Hippocampal Network Reorganization Underlies the Formation of a Temporal Association Memory. *Neuron*, 107(2), 283–291.e6.
- Bakkour, A., Palombo, D. J., Zylberberg, A., Kang, Y. H., Reid, A., Verfaellie, M., Shadlen, M. N., & Shohamy, D. (2019). The hippocampus supports deliberation during value-based decisions. *eLife*, 8. <https://doi.org/10.7554/eLife.46080>
- Bast, T., Wilson, I. A., Witter, M. P., & Morris, R. G. M. (2009). From rapid place learning to behavioral performance: a key role for the intermediate hippocampus. *PLoS Biology*, 7(4), e1000089.
- Bryant, K. G., & Barker, J. M. (2020). Arbitration of Approach-Avoidance Conflict by Ventral Hippocampus. *Frontiers in Neuroscience*, 14, 615337.
- Çavdaroğlu, B., Riaz, S., Shi, Y., Balci, F., & Ito, R. (2021). The ventral hippocampus CA3 is critical in regulating timing uncertainty in temporal decision-making. In *Cell Reports* (Vol. 34, Issue 5, p. 108694). <https://doi.org/10.1016/j.celrep.2021.108694>
- Chen, A. C., & Etkin, A. (2013). Hippocampal network connectivity and activation differentiates post-traumatic stress disorder from generalized anxiety disorder. *Neuropsychopharmacology: Official Publication of the American College of Neuropsychopharmacology*, 38(10), 1889–1898.

- Chockanathan, U., & Padmanabhan, K. (2021). Divergence in Population Coding for Space between Dorsal and Ventral CA1. *eNeuro*, 8(5).
<https://doi.org/10.1523/ENEURO.0211-21.2021>
- Ciocchi, S., Passecker, J., Malagon-Vina, H., Mikus, N., & Klausberger, T. (2015). Brain computation. Selective information routing by ventral hippocampal CA1 projection neurons. *Science*, 348(6234), 560–563.
- Eichenbaum, H., Kuperstein, M., Fagan, A., & Nagode, J. (1987). Cue-sampling and goal-approach correlates of hippocampal unit activity in rats performing an odor-discrimination task. *The Journal of Neuroscience: The Official Journal of the Society for Neuroscience*, 7(3), 716–732.
- Esclassan, F., Coutureau, E., Di Scala, G., & Marchand, A. R. (2009). Differential contribution of dorsal and ventral hippocampus to trace and delay fear conditioning. In *Hippocampus* (Vol. 19, Issue 1, pp. 33–44). <https://doi.org/10.1002/hipo.20473>
- Forro, T., Volitaki, E., Malagon-Vina, H., Klausberger, T., Nevian, T., & Ciocchi, S. (2022). Anxiety-related activity of ventral hippocampal interneurons. *Progress in Neurobiology*, 219, 102368.
- Gauthier, J. L., & Tank, D. W. (2018). A Dedicated Population for Reward Coding in the Hippocampus. *Neuron*, 99(1), 179–193.e7.
- Hauser, J., Llano López, L. H., Feldon, J., Gargiulo, P. A., & Yee, B. K. (2020). Small lesions of the dorsal or ventral hippocampus subregions are associated with distinct impairments in working memory and reference memory retrieval, and combining them attenuates the acquisition rate of spatial reference memory. In *Hippocampus* (Vol. 30, Issue 9, pp. 938–957). <https://doi.org/10.1002/hipo.23207>

- Itskov, P. M., Vinnik, E., Honey, C., Schnupp, J., & Diamond, M. E. (2012). Sound sensitivity of neurons in rat hippocampus during performance of a sound-guided task. *Journal of Neurophysiology*, *107*(7), 1822–1834.
- Jarzebowski, P., Hay, Y. A., Grewe, B. F., & Paulsen, O. (2022). Different encoding of reward location in dorsal and intermediate hippocampus. *Current Biology: CB*, *32*(4), 834–841.e5.
- Jimenez, J. C., Su, K., Goldberg, A. R., Luna, V. M., Biane, J. S., Ordek, G., Zhou, P., Ong, S. K., Wright, M. A., Zweifel, L., Paninski, L., Hen, R., & Kheirbek, M. A. (2018). Anxiety Cells in a Hippocampal-Hypothalamic Circuit. *Neuron*, *97*(3), 670–683.e6.
- Jin, S.-W., & Lee, I. (2021). Differential encoding of place value between the dorsal and intermediate hippocampus. *Current Biology: CB*, *31*(14), 3053–3072.e5.
- Keinath, A. T., Wang, M. E., Wann, E. G., Yuan, R. K., Dudman, J. T., & Muzzio, I. A. (2014). Precise spatial coding is preserved along the longitudinal hippocampal axis. *Hippocampus*, *24*(12), 1533–1548.
- Kesner, R. P., Hunsaker, M. R., & Ziegler, W. (2011). The role of the dorsal and ventral hippocampus in olfactory working memory. *Neurobiology of Learning and Memory*, *96*(2), 361–366.
- Kheirbek, M. A., & Hen, R. (2011). Dorsal vs ventral hippocampal neurogenesis: implications for cognition and mood. *Neuropsychopharmacology: Official Publication of the American College of Neuropsychopharmacology*, *36*(1), 373–374.
- Knudsen, E. B., & Wallis, J. D. (2021). Hippocampal neurons construct a map of an abstract value space. *Cell*, *184*(18), 4640–4650.e10.

- Komorowski, R. W., Garcia, C. G., Wilson, A., Hattori, S., Howard, M. W., & Eichenbaum, H. (2013). Ventral hippocampal neurons are shaped by experience to represent behaviorally relevant contexts. *The Journal of Neuroscience: The Official Journal of the Society for Neuroscience*, *33*(18), 8079–8087.
- Li, J., Cao, D., Dimakopoulos, V., Shi, W., Yu, S., Fan, L., Stieglitz, L., Imbach, L., Sarnthein, J., & Jiang, T. (2022). Anterior–Posterior Hippocampal Dynamics Support Working Memory Processing. In *The Journal of Neuroscience* (Vol. 42, Issue 3, pp. 443–453). <https://doi.org/10.1523/jneurosci.1287-21.2021>
- Li, Y., Xu, J., Liu, Y., Zhu, J., Liu, N., Zeng, W., Huang, N., Rasch, M. J., Jiang, H., Gu, X., Li, X., Luo, M., Li, C., Teng, J., Chen, J., Zeng, S., Lin, L., & Zhang, X. (2017). A distinct entorhinal cortex to hippocampal CA1 direct circuit for olfactory associative learning. *Nature Neuroscience*, *20*(4), 559–570.
- Malivoire, B. L., Girard, T. A., Patel, R., & Monson, C. M. (2018). Functional connectivity of hippocampal subregions in PTSD: relations with symptoms. *BMC Psychiatry*, *18*(1), 129.
- Martin, C., Beshel, J., & Kay, L. M. (2007). An olfacto-hippocampal network is dynamically involved in odor-discrimination learning. *Journal of Neurophysiology*, *98*(4), 2196–2205.
- McEchron, M. D., Bouwmeester, H., Tseng, W., Weiss, C., & Disterhoft, J. F. (1999). Hippocampectomy disrupts auditory trace fear conditioning and contextual fear conditioning in the rat. In *Hippocampus* (Vol. 8, Issue 6, pp. 638–646). [https://doi.org/10.1002/\(sici\)1098-1063\(1998\)8:6<638::aid-hipo6>3.0.co;2-q](https://doi.org/10.1002/(sici)1098-1063(1998)8:6<638::aid-hipo6>3.0.co;2-q)

- Mikulovic, S., Restrepo, C. E., Siwani, S., Bauer, P., Pupe, S., Tort, A. B. L., Kullander, K., & Leão, R. N. (2018). Ventral hippocampal OLM cells control type 2 theta oscillations and response to predator odor. *Nature Communications*, *9*(1), 3638.
- Morey, R. A., Haswell, C. C., Hooper, S. R., & De Bellis, M. D. (2016). Amygdala, Hippocampus, and Ventral Medial Prefrontal Cortex Volumes Differ in Maltreated Youth with and without Chronic Posttraumatic Stress Disorder. *Neuropsychopharmacology: Official Publication of the American College of Neuropsychopharmacology*, *41*(3), 791–801.
- Musall, S., Kaufman, M. T., Juavinett, A. L., Gluf, S., & Churchland, A. K. (2019). Single-trial neural dynamics are dominated by richly varied movements. *Nature Neuroscience*, *22*(10), 1677–1686.
- Nguyen, H.-B., Parent, C., Tse, Y. C., Wong, T. P., & Meaney, M. J. (2018). Generalization of Conditioned Auditory Fear is Regulated by Maternal Effects on Ventral Hippocampal Synaptic Plasticity. *Neuropsychopharmacology: Official Publication of the American College of Neuropsychopharmacology*, *43*(6), 1297–1307.
- Padilla-Coreano, N., Bolkan, S. S., Pierce, G. M., Blackman, D. R., Hardin, W. D., Garcia-Garcia, A. L., Spellman, T. J., & Gordon, J. A. (2016). Direct Ventral Hippocampal-Prefrontal Input Is Required for Anxiety-Related Neural Activity and Behavior. *Neuron*, *89*(4), 857–866.
- Parfitt, G. M., Nguyen, R., Bang, J. Y., Aqrabawi, A. J., Tran, M. M., Kanghoon Seo, D., Richards, B. A., & Kim, J. C. (2017). Bidirectional Control of Anxiety-Related Behaviors in Mice: Role of Inputs Arising from the Ventral Hippocampus to the

Lateral Septum and Medial Prefrontal Cortex. In *Neuropsychopharmacology* (Vol. 42, Issue 8, pp. 1715–1728). <https://doi.org/10.1038/npp.2017.56>

Phillips, R. G., & LeDoux, J. E. (1992). Differential contribution of amygdala and hippocampus to cued and contextual fear conditioning. In *Behavioral Neuroscience* (Vol. 106, Issue 2, pp. 274–285). <https://doi.org/10.1037/0735-7044.106.2.274>

Pi, G., Gao, D., Wu, D., Wang, Y., Lei, H., Zeng, W., Gao, Y., Yu, H., Xiong, R., Jiang, T., Li, S., Wang, X., Guo, J., Zhang, S., Yin, T., He, T., Ke, D., Li, R., Li, H., ... Wang, J.-Z. (2020). Posterior basolateral amygdala to ventral hippocampal CA1 drives approach behaviour to exert an anxiolytic effect. *Nature Communications*, *11*(1), 183.

Poppenk, J., Evensmoen, H. R., Moscovitch, M., & Nadel, L. (2013). Long-axis specialization of the human hippocampus. *Trends in Cognitive Sciences*, *17*(5), 230–240.

Radvansky, B. A., Oh, J. Y., Climer, J. R., & Dombeck, D. A. (2021). Behavior determines the hippocampal spatial mapping of a multisensory environment. *Cell Reports*, *36*(5), 109444.

Rao, R. P., von Heimendahl, M., Bahr, V., & Brecht, M. (2019). Neuronal Responses to Conspecifics in the Ventral CA1. *Cell Reports*, *27*(12), 3460–3472.e3.

Salimi, M., Tabasi, F., Nazari, M., Ghazvineh, S., & Raoufy, M. R. (2022). The olfactory bulb coordinates the ventral hippocampus-medial prefrontal cortex circuit during spatial working memory performance. *The Journal of Physiological Sciences: JPS*, *72*(1), 9.

- Sánchez-Bellot, C., AlSubaie, R., Mishchanchuk, K., Wee, R. W. S., & MacAskill, A. F. (2022). Two opposing hippocampus to prefrontal cortex pathways for the control of approach and avoidance behaviour. *Nature Communications*, *13*(1), 339.
- Schoepfer, K. J. (2020). *Hippocampal-Prefrontal Oscillatory Signaling in the Rat Brain: Sexual Dimorphisms and Effects of Female Estrous Stage*.
- Shan, K. Q., Lubenov, E. V., Papadopoulou, M., & Siapas, A. G. (2016). Spatial tuning and brain state account for dorsal hippocampal CA1 activity in a non-spatial learning task. In *eLife* (Vol. 5). <https://doi.org/10.7554/elife.14321>
- Stringer, C., Pachitariu, M., Steinmetz, N., Reddy, C. B., Carandini, M., & Harris, K. D. (2019). Spontaneous behaviors drive multidimensional, brainwide activity. *Science*, *364*(6437), 255.
- Taxidis, J., Pnevmatikakis, E. A., Dorian, C. C., Mylavarapu, A. L., Arora, J. S., Samadian, K. D., Hoffberg, E. A., & Golshani, P. (2020). Differential Emergence and Stability of Sensory and Temporal Representations in Context-Specific Hippocampal Sequences. *Neuron*, *108*(5), 984–998.e9.
- Turner, V. S., O'Sullivan, R. O., & Kheirbek, M. A. (2022). Linking external stimuli with internal drives: A role for the ventral hippocampus. *Current Opinion in Neurobiology*, *76*, 102590.
- Wang, M. E., Fraize, N. P., Yin, L., Yuan, R. K., Petsagourakis, D., Wann, E. G., & Muzzio, I. A. (2013). Differential roles of the dorsal and ventral hippocampus in predator odor contextual fear conditioning. *Hippocampus*, *23*(6), 451–466.
- Zaremba, J. D., Diamantopoulou, A., Danielson, N. B., Grosmark, A. D., Kaifosh, P. W., Bowler, J. C., Liao, Z., Sparks, F. T., Gogos, J. A., & Losonczy, A. (2017). Impaired

hippocampal place cell dynamics in a mouse model of the 22q11.2 deletion. In *Nature Neuroscience* (Vol. 20, Issue 11, pp. 1612–1623).

<https://doi.org/10.1038/nn.4634>

Zhang, W.-N., Bast, T., Xu, Y., & Feldon, J. (2014). Temporary inhibition of dorsal or ventral hippocampus by muscimol: Distinct effects on measures of innate anxiety on the elevated plus maze, but similar disruption of contextual fear conditioning. In *Behavioural Brain Research* (Vol. 262, pp. 47–56).

<https://doi.org/10.1016/j.bbr.2013.10.044>

Publishing Agreement

It is the policy of the University to encourage open access and broad distribution of all theses, dissertations, and manuscripts. The Graduate Division will facilitate the distribution of UCSF theses, dissertations, and manuscripts to the UCSF Library for open access and distribution. UCSF will make such theses, dissertations, and manuscripts accessible to the public and will take reasonable steps to preserve these works in perpetuity.

I hereby grant the non-exclusive, perpetual right to The Regents of the University of California to reproduce, publicly display, distribute, preserve, and publish copies of my thesis, dissertation, or manuscript in any form or media, now existing or later derived, including access online for teaching, research, and public service purposes.

DocuSigned by:

Max Ladow

F2EDDB6F533140F...

Author Signature

12/2/2022

Date